

Exploiting Newton-factorized, 2PN-accurate, waveform multipoles in effective-one-body models for spin-aligned noncircularized binaries

Andrea Placidi^{1,2}, Simone Albanesi^{3,4}, Alessandro Nagar^{4,5},
Marta Orselli^{1,2}, Sebastiano Bernuzzi⁶, and Gianluca Grignani¹

¹*Dipartimento di Fisica e Geologia, Università di Perugia,*

INFN Sezione di Perugia, Via A. Pascoli, 06123 Perugia, Italia

²*Niels Bohr Institute, Copenhagen University, Blegdamsvej 17, DK-2100 Copenhagen O, Denmark*

³*Dipartimento di Fisica, Università di Torino, via P. Giuria 1, 10125 Torino, Italy*

⁴*INFN Sezione di Torino, Via P. Giuria 1, 10125 Torino, Italy*

⁵*Institut des Hautes Etudes Scientifiques, 91440 Bures-sur-Yvette, France and*

⁶*Theoretisch-Physikalisches Institut, Friedrich-Schiller-Universität Jena, 07743, Jena, Germany*

(Dated: March 9, 2022)

We present a new approach to factorize and resum the post-Newtonian (PN) waveform for generic equatorial motion to be used within effective-one-body (EOB) based waveform models. The new multipolar waveform factorization improves previous prescriptions in that: (i) the generic Newtonian contribution is factored out from each multipole; (ii) the circular part is factored out and resummed using standard EOB methods and (iii) the residual, 2PN-accurate, noncircular part, and in particular the tail contribution, is additionally resummed using Padé approximants. The resulting waveform is validated in the extreme-mass-ratio limit by comparisons with nine (mostly nonspinning) numerical waveforms either from eccentric inspirals, with eccentricities up to $e = 0.9$, or dynamical captures. The resummation of the noncircular tail contribution is found essential to obtain excellent ($\lesssim 0.05$ rad at periastron for $e = 0.9$) analytical/numerical agreement and to considerably improve the prescription with just the Newtonian prefactor. In the comparable mass case, the new 2PN waveform shows only a marginal improvement over the previous Newtonian factorization, though yielding maximal unfaithfulness $\simeq 10^{-3}$ with the 28 publicly available numerical relativity simulations with eccentricity up to ~ 0.3 (except for a single outlier that grazes 10^{-2}). We finally use test-particle data to validate the waveform factorization proposed by Khalil et al. [Phys. Rev. 104 (2021) 2, 024046] and conclude that its amplitude can be considered reliable (though less accurate, $\sim 6\%$ fractional difference versus 1.5% of our method) only up to eccentricities ~ 0.3 .

I. INTRODUCTION

One of the greatest achievements of recent years is the detection of gravitational waves (GW) from coalescing binary systems by the LIGO-Virgo-Kagra (LVK) collaboration [1]. This opened up a new exciting way of investigating the properties of spacetime in regime of strong gravitational field. Moreover, the scientific community is already working hard to plan the construction of ground based detectors of third generation [2–7], such as Einstein Telescope [8] and Cosmic Explorer [9], with extremely high sensitivity. In addition, the space based detector LISA [10] will open a window in the low frequency band allowing the potential detection of new kinds of sources, such as Intermediate and Extreme-Mass-Ratio Inspirals [11–13]. This gives rise to the compelling need of improving the analytical waveform models used to interpret the detected GW signals [14]. In particular, the question of how to incorporate eccentric effects in the waveform models for coalescing binaries, both on the analytical and the numerical side, is under intense study [15–27]. More specifically, Ref. [17] introduced an efficient and accurate, yet simple, approach to generalize the effective-one-body (EOB) quasi-circular waveform and radiation-reaction of the `TEOBResumS` model to the eccentric case, basically consisting in replacing the standard quasi-circular Newtonian prefactors in these func-

tions with the general expression that follows from taking the time-derivatives of the Newtonian mass and current multipoles. The same idea has been used to describe dynamical captures of black holes [28], leading to an EOB model able to describe binaries with generic orbits [24]. This breakthrough in the description of noncircular systems even allowed a new analysis of GW190521 [29], showing that the dynamical capture scenario is favorite against the quasi-circular highly-precessing scenario proposed by the LVK Collaboration [30]. Moreover, a recent work [25] showed that the inclusion of higher-order post Newtonian (PN) terms in the EOB potentials allows to construct a model that is both faithful in the quasi-circular case, similarly to the native quasi-circular model, as well as for eccentric inspirals.

Nonetheless, high-PN, noncircular, analytical information computed in several works [27, 31] has not been incorporated yet within `TEOBResumS`, although it is currently present in other models [20, 27, 32]. In particular, the 2PN-accurate waveform of Ref. [27] has been included in a new EOB model for eccentric coalescence, `SEOBNRv4HME` [32] that builds upon the quasi-circular model `SEOBNRv4HM` [33, 34], that is rather different from `TEOBResumS` either in structure and performance [35, 36]. The purpose of this work is to exploit currently known analytical results up to 2PN so to include them in `TEOBResumS`-based eccentric models [24, 25]. In particular, we exploit here the analytical 2PN waveform infor-

mation present in its original form in both Refs. [27, 31]¹. In practice, each multipole is factorized using the general Newtonian prefactor, as proposed in Ref. [17], that is then multiplied by a resummed quasicircular correction and by the residual noncircular correction at 2PN. This latter contribution is then additionally resummed. This procedure is extensively tested against different types of numerical waveform data both in the test-mass limit and for comparable-mass binaries.

The paper is organized as follows. In Sec. II we review available analytical results up to 2PN accuracy and calculate the genuine noncircular contribution at 2PN accuracy obtained by factoring out, multipole by multipole, both the generic Newtonian prefactor and the circular part. This analytic approach is validated in Sec. III by comparison with numerical waveforms emitted by a test-particle orbiting a Kerr black hole along eccentric orbits. This gives rise to the need of implementing additional resummation strategies, notably on the noncircular tail contribution, so to obtain analytical waveforms that are reliable *also* for large eccentricities, $e \sim 0.9$. In Sec. IV we perform similar analyses for a few illustrative hyperbolic encounters and dynamical capture scenario in the test-mass limit. Section V focuses on comparable-mass binaries and provides direct phasing comparisons between Numerical Relativity (NR) waveforms and the EOB eccentric model of Ref. [25] updated with the new 2PN-accurate factorized and resummed waveform. Finally, in Sec. VI, for the test-mass limit case, we provide analogous waveform comparisons with the factorization scheme proposed in Ref. [27] (and used in Ref. [32]), whose distinctive feature is that *only* the circular Newtonian prefactor, instead of the generic one, is factorized for each multipole. Concluding remarks are collected in Sec. VII. The paper is finally completed by a few technical Appendixes. If not otherwise specified, we use geometrical units with $G = c = 1$.

II. NEWTON-FACTORIZED EOB WAVEFORM

The 2PN waveform in EOB coordinates was recently obtained by Khalil et al. [27]. For the instantaneous contribution, they obtained the expressions for the modes in EOB coordinates at 2PN accuracy by translating to EOB coordinates the results of Refs. [31, 37] which are originally expressed in harmonic coordinates. The tail contri-

butions are derived starting from the results of Ref. [16] which are subsequently extended in Ref. [27] to include higher order corrections in the eccentricity and also to higher modes. The final result in Ref. [27] is then written using the standard factorization of the circular part, adding the noncircular contribution as a correction. Here we exploit the PN-expanded results of Ref. [27] (neglecting the spin part) but then we employ a rather different factorization scheme. Before doing so, it is pedagogically useful to recall here all the steps, in order to fix the notation and to keep the discussion as self-contained as possible. In this section we mostly focus on the dominant mode with $\ell = m = 2$. The results for the subdominant modes are presented in Appendix A. Note also that in Sec. II C we discuss some issues related to the modes with $m = 0$.

A. The 2PN waveform in EOB coordinates

To start with, let us recall that we work with the following multipolar decomposition of the strain waveform

$$h_+ - ih_\times = D_L^{-1} \sum_{\ell=2}^{\ell_{\max}} \sum_{m=-\ell}^{\ell} h_{\ell m} {}_{-2}Y_{\ell m}, \quad (1)$$

where D_L is the source distance in radiative coordinates and ${}_{-2}Y_{\ell m}$ are the spin-weight -2 spherical harmonics. Each waveform mode is additionally factorized as [31]

$$h_{\ell m} = 4\nu \sqrt{\frac{\pi}{5}} e^{-im\varphi} \hat{H}_{\ell m}, \quad (2)$$

where each $\hat{H}_{\ell m}$ mode is decomposed in the sum of instantaneous and hereditary (or tail) terms

$$\hat{H}_{\ell m} = \hat{H}_{\ell m}^{\text{inst}} + \hat{H}_{\ell m}^{\text{tail}}, \quad (3)$$

that enter at different PN orders.

1. Instantaneous contributions

The instantaneous contributions to the modes for non-spinning binaries were derived in Ref. [38, 39] up to 2PN order and in Ref. [31] up to 3PN order, where they are expressed in harmonic coordinates. The 2PN-accurate $\ell = m = 2$ mode in harmonic coordinates explicitly reads

$$(\hat{H}_{22}^{\text{inst}})_h = \frac{1}{r_h} + r_h^2 \dot{\varphi}_h^2 + 2ir_h \dot{r}_h \dot{\varphi}_h - \dot{r}_h^2$$

¹ Note that, although Ref. [27] also computed new spin-dependent eccentric waveform corrections up to 2PN, we will not use them

here, but postpone their inclusion in a suitable factorized waveform to future work.

$$\begin{aligned}
& + \frac{1}{c^2} \left\{ \frac{1}{r_h^2} \left(\frac{\nu}{2} - 5 \right) + r_h \left[\dot{\varphi}_h^2 \left(\frac{78\nu}{21} + \frac{11}{42} \right) - i\dot{r}_h\dot{\varphi}_h(r_h^2 + r_h^2\dot{\varphi}_h^2) \left(\frac{27\nu}{7} - \frac{9}{7} \right) \right] \right. \\
& - \left. \frac{\dot{r}_h^2}{r_h} \left(\frac{16\nu}{7} + \frac{15}{14} \right) + i\dot{r}_h\dot{\varphi}_h \left(\frac{45\nu}{7} + \frac{25}{21} \right) + (r_h^4 - r_h^4\dot{\varphi}_h^4) \left(\frac{27\nu}{14} - \frac{9}{14} \right) \right\} \\
& + \frac{1}{c^4} \left\{ \frac{1}{r_h^3} \left(\frac{79\nu^2}{126} + \frac{181\nu}{36} + \frac{757}{63} \right) + \dot{\varphi}_h^2 \left(\frac{13133\nu^2}{1512} - \frac{5225\nu}{216} - \frac{11891}{1512} \right) \right. \\
& + \frac{\dot{r}_h^4}{r_h} \left(\frac{214\nu^2}{21} + \frac{83\nu}{21} - \frac{557}{168} \right) + \frac{i\dot{r}_h\dot{\varphi}_h}{r_h} \left(\frac{2852\nu^2}{189} - \frac{3767\nu}{189} - \frac{773}{189} \right) \\
& - \frac{\dot{r}_h^2}{r_h^2} \left(\frac{467\nu^2}{126} + \frac{2789\nu}{252} - \frac{619}{252} \right) + (r_h^2 r_h^4 \dot{\varphi}_h^4 - r_h^6 + r_h^6 \dot{\varphi}_h^6 - r_h^2 r_h^4 \dot{\varphi}_h^2) \left(\frac{1111\nu^2}{168} - \frac{589\nu}{168} + \frac{83}{168} \right) \\
& - i\dot{r}_h^2 \dot{r}_h \dot{\varphi}_h^3 \left(\frac{1703\nu^2}{84} - \frac{103\nu}{12} - \frac{433}{84} \right) - i\dot{r}_h^3 \dot{\varphi}_h \left(\frac{211\nu^2}{9} + \frac{731\nu}{63} - \frac{863}{126} \right) \\
& + r_h^3 \dot{\varphi}_h^4 \left(-\frac{2995\nu^2}{252} + \frac{19\nu}{252} + \frac{835}{252} \right) + i r_h^3 \dot{r}_h^3 \dot{\varphi}_h^3 \left(\frac{1111\nu^2}{42} - \frac{589\nu}{42} + \frac{83}{42} \right) \\
& \left. - r_h \dot{r}_h^2 \dot{\varphi}_h^2 \left(\frac{58\nu^2}{21} + \frac{169\nu}{14} - \frac{11}{28} \right) + i(r_h \dot{r}_h^5 \dot{\varphi}_h + \dot{r}_h r_h^5 \dot{\varphi}_h^5) \left(\frac{1111\nu^2}{84} - \frac{589\nu}{84} + \frac{83}{84} \right) \right\} + \mathcal{O}\left(\frac{1}{c^6}\right), \quad (4)
\end{aligned}$$

where φ_h is the harmonic orbital phase, r_h is the mass-reduced radial harmonic coordinate defined as $r_h \equiv R_h/M$, with $M = m_1 + m_2$ where m_1 and m_2 are the individual masses of the binary system. For completeness we explicitly report here the transformation from harmonic to EOB coordinates, following the same steps of Ref. [27] using the relations that can be derived from Ref. [40]. The EOB dynamics is expressed using mass-reduced phase-space variables $(r, \varphi, p_r, p_\varphi)$, which are related to the physical ones by $r \equiv R/M$ (relative separation),

$p_r = P_R/\mu$ (radial momentum), φ (orbital phase), $p_\varphi = P_\varphi/(\mu M)$ (angular momentum) and $t = T/M$ (time) where $\mu \equiv m_1 m_2 / M$. As for the relative separation, we will henceforth use its inverse $u \equiv 1/r$. Moreover, to better keep track of the PN counting, we will make explicit the dependence on $1/c$, recalling that $u \sim p_r^2 \sim p_\varphi^2 u^2 \sim 1/c^2$. Using the transformation laws given in Ref. [40], we obtain the following relations between the quantities $(r_h, \dot{r}_h, \varphi_h, \dot{\varphi}_h)$ and the EOB canonical variables $(u, \varphi, p_r, p_\varphi)$

$$\begin{aligned}
r_h &= \frac{1}{u} + \frac{1}{c^2} \left[\frac{1}{2} \nu \left(\frac{3p_r^2}{u} + p_\varphi^2 u - 1 \right) - 1 \right] \\
& - \frac{\nu}{8c^4 u} \left[(5 - 3\nu)p_r^4 + 2p_r^2 u \left(28 - 3(\nu - 1)p_\varphi^2 u \right) + u^2 \left(2(\nu - 19) + (\nu + 1)p_\varphi^4 u^2 + p_\varphi^2 u(1 - 3\nu) \right) \right] \\
& + \mathcal{O}\left(\frac{1}{c^6}\right), \quad (5)
\end{aligned}$$

$$\begin{aligned}
\dot{r}_h &= p_r + \frac{1}{2c^2} p_r \left[(2\nu - 1)p_r^2 + u \left((4\nu - 1)p_\varphi^2 u - 6 - 4\nu \right) \right] \\
& + \frac{1}{8c^4} \left[(3 - 8\nu)p_r^5 - 2p_r^3 u \left(2(8\nu - 5) + (2\nu^2 + 12\nu - 3) p_\varphi^2 u \right) \right. \\
& \left. + p_r u^2 \left(-10\nu^2 + 78\nu + 12 + (8\nu^2 - 16\nu + 3) p_\varphi^4 u^2 + 2(\nu^2 - 55\nu + 6) p_\varphi^2 u \right) \right] + \mathcal{O}\left(\frac{1}{c^6}\right), \quad (6)
\end{aligned}$$

$$\varphi_h = \varphi + \frac{1}{c^2} \nu p_r p_\varphi u - \frac{1}{4c^4} \nu p_r p_\varphi u \left((4\nu + 2)p_r^2 + u \left(-3\nu + 15 + 2p_\varphi^2 u \right) \right) + \mathcal{O}\left(\frac{1}{c^6}\right), \quad (7)$$

$$\dot{\varphi}_h = p_\varphi u^2 + \frac{1}{2c^2} p_\varphi u^2 \left[u \left((\nu - 1)p_\varphi^2 u - 2 \right) - (3\nu + 1)p_r^2 \right]$$

$$\begin{aligned}
& -\frac{1}{8c^4}p_\varphi u^2 \left[-\left(15\nu^2 + 11\nu + 3\right)p_r^4 + 2p_r^2 u \left(2\left(\nu^2 - 24\nu - 3\right) + 3\left(3\nu^2 - \nu - 1\right)p_\varphi^2 u\right) \right. \\
& \left. + u^2 \left(2\left(\nu^2 - 9\nu + 2\right) + \left(\nu^2 + 5\nu - 3\right)p_\varphi^4 u^2 - 2\left(3\nu^2 - 17\nu + 2\right)p_\varphi^2 u\right) \right] + \mathcal{O}\left(\frac{1}{c^6}\right). \tag{8}
\end{aligned}$$

Replacing these equations into Eq. (4) above, yields

$$\begin{aligned}
\hat{H}_{22}^{\text{inst}} &= u - p_r^2 + 2ip_r p_\varphi u + p_\varphi^2 u^2 + \frac{1}{c^2} \left\{ i \left(\frac{\nu}{7} - \frac{5}{7} \right) p_r^3 p_\varphi u - ip_r p_\varphi u^2 \left[\left(\frac{4\nu}{7} + \frac{185}{21} \right) - \left(\frac{\nu}{7} - \frac{5}{7} \right) p_\varphi^2 u \right] \right. \\
&+ \left. \left(\frac{\nu}{14} - \frac{5}{14} \right) (p_\varphi^4 u^4 - p_r^4) + \left(\frac{3\nu}{14} + \frac{64}{14} \right) p_r^2 u + u^2 \left[(\nu - 4) + \left(\frac{31\nu}{14} - \frac{157}{42} \right) p_\varphi^2 u \right] \right\} \\
&+ \frac{1}{c^4} \left\{ \left(\frac{17\nu^2}{168} + \frac{13\nu}{168} - \frac{5}{24} \right) (p_r^6 + p_r^4 p_\varphi^2 u^2 - p_\varphi^6 u^6) - i \left(\frac{17\nu^2}{84} + \frac{13\nu}{84} - \frac{5}{12} \right) p_r p_\varphi u (p_r^4 + p_\varphi^4 u^4) \right\} \\
&- p_r^2 u^2 \left[\left(\frac{13\nu^2}{63} + \frac{151\nu}{18} + \frac{1055}{252} \right) + \left(\frac{17\nu^2}{504} + \frac{13\nu}{504} - \frac{5}{72} \right) p_\varphi^4 u^2 + \left(\frac{313\nu^2}{252} + \frac{85\nu}{252} - \frac{101}{252} \right) p_\varphi^2 u \right] \\
&- \left(\frac{85\nu^2}{168} + \frac{55\nu}{168} + \frac{425}{168} \right) p_r^4 u + ip_r^3 p_\varphi u^2 \left[\left(\frac{62\nu^2}{63} + \frac{11\nu}{126} + \frac{695}{126} \right) - \left(\frac{17\nu^2}{42} + \frac{13\nu}{42} - \frac{5}{6} \right) p_\varphi^2 u \right] \\
&- ip_r p_\varphi u^3 \left[\left(\frac{523\nu^2}{189} + \frac{2452\nu}{189} - \frac{193}{27} \right) + \left(\frac{8\nu^2}{21} - \frac{29\nu}{14} - \frac{67}{28} \right) p_\varphi^2 u \right] + u^3 \left[\left(\frac{205\nu^2}{126} - \frac{49\nu}{18} + \frac{190}{63} \right) \right. \\
&\left. - \left(\frac{671\nu^2}{504} + \frac{1375\nu}{504} - \frac{481}{72} \right) p_\varphi^4 u^2 + \left(\frac{127\nu^2}{27} - \frac{2710\nu}{189} - \frac{5519}{1512} \right) p_\varphi^2 u \right] \left. \right\} + \mathcal{O}\left(\frac{1}{c^6}\right). \tag{9}
\end{aligned}$$

This result coincides with Eq. (83) of Ref. [27] by replacing $p_\varphi^2 u^2 = p^2 - p_r^2$. The canonical transformations above have also been applied to the other multipoles up to $\ell = 6$ and have been obtained independently of Ref. [27], which appeared while the current paper was in preparation. Our results precisely coincide with those of Ref. [27]. However, as an additional, independent, validation of the transformations applied to the various multipoles we have shown that the 2PN angular momentum flux given by Eq. (3.70) of Ref. [40] can be obtained combining together the various multipoles once written in EOB coordinates, as explained in Appendix B.

2. Hereditary contributions

The hereditary components $\hat{H}_{\ell m}^{\text{tail}}$ are taken from Ref. [27]. These contributions were computed as an expansion in eccentricity and using the Keplerian parametrization (KP), according to the method out-

lined in [16]. The resulting tail contributions are initially expressed in terms of the frequency parameter $x \equiv (GM\Omega/c^3)^{2/3}$, the eccentricity e and the phase variable χ , which together with the semilatus rectum p parameterize the motion as

$$r = \frac{p}{1 + e \cos \chi}. \tag{10}$$

In particular the parameters p and e used in Refs. [16, 27] and in this paper are defined in analogy with Newtonian mechanics by the relations²

$$e = \frac{r_+ - r_-}{r_+ + r_-}, \quad p = \frac{2r_+ r_-}{r_+ + r_-}, \tag{11}$$

where r_\pm are the turning point of the radial motion, respectively apastron and periastron.

From Ref. [27], the $\ell = m = 2$ dominant tail component at 2PN accuracy, and up $\mathcal{O}(e^6)$, reads

the quasi-Keplerian parametrization.

² We warn the reader that the eccentricity e defined here is different from the time eccentricity e_t that appears in the context of

$$\begin{aligned}
(\hat{H}_{22}^{\text{tail}})_{KP} = & \frac{2\pi x^{5/2}}{c^3} \left[1 + e \left(\frac{11e^{-i\chi}}{8} + \frac{13e^{i\chi}}{8} \right) + e^2 \left(\frac{5}{8}e^{-2i\chi} + \frac{7}{8}e^{2i\chi} + 4 \right) + e^3 \left(\frac{121e^{-i\chi}}{32} + \frac{143e^{i\chi}}{32} + \frac{3e^{-3i\chi}}{32} + \frac{e^{3i\chi}}{12} \right) \right. \\
& + e^4 \left(\frac{25e^{-2i\chi}}{16} + \frac{203e^{2i\chi}}{96} - \frac{5e^{4i\chi}}{96} + \frac{65}{8} \right) + e^5 \left(\frac{55e^{-i\chi}}{8} + \frac{6233e^{i\chi}}{768} + \frac{15e^{-3i\chi}}{64} + \frac{281e^{3i\chi}}{1536} + \frac{53e^{5i\chi}}{7680} \right) \\
& \left. + e^6 \left(\frac{175e^{-2i\chi}}{64} + \frac{1869e^{2i\chi}}{512} - \frac{449e^{4i\chi}}{3840} + \frac{31e^{6i\chi}}{23040} + \frac{30247}{2304} \right) \right]. \tag{12}
\end{aligned}$$

Analogously to Ref. [27], we want to recast the expressions above in terms of EOB phase-space variables. In particular, we want to use (u, p_r, p_φ) only, avoiding the explicit appearance of the time-derivatives of the momenta. This will eventually simplify the numerical implementation and differs from the choice made in Ref. [27]. Since we are working at 2PN accuracy, to this aim we can use the following Newtonian relations³

$$x = \frac{1 - e^2}{p}, \tag{13}$$

$$u = \frac{1 + e \cos\chi}{p}, \tag{14}$$

$$p_\varphi = \sqrt{p}, \tag{15}$$

$$p_r = \frac{e \sin\chi}{\sqrt{p}}. \tag{16}$$

Moreover, since Eq. (12) is given as an expansion in the eccentricity e , it is important to identify the proper variables, in terms of the new set (u, p_r, p_φ) , which are of the same order in the eccentricity. One can show that Eq. (12) translates into an expansion in both p_r and \dot{p}_r , with the latter related to p_φ through the Newtonian equation of motion

$$\dot{p}_r = u^2(p_\varphi^2 u - 1). \tag{17}$$

Using Eqs. (13)-(16), one can show that $p_r \sim e$ and $(p_\varphi^2 u - 1) \sim e$. In this way, from Eq. (12) one obtains an expression in terms of (u, p_r, \dot{p}_r) which contains also half integer powers of u , and that reads⁴

$$\begin{aligned}
\hat{H}_{22}^{\text{tail}} = & \frac{2\pi u^{5/2}}{c^3} \left[1 + \left(\frac{\dot{p}_r}{2u^2} + \frac{ip_r}{4\sqrt{u}} \right) - \frac{\dot{p}_r^2}{8u^4} - \left(\frac{\dot{p}_r^3}{96u^6} + \frac{7ip_r\dot{p}_r^2}{32u^{9/2}} - \frac{7p_r^2\dot{p}_r}{32u^3} - \frac{7ip_r^3}{96u^{3/2}} \right) + \left(\frac{7\dot{p}_r^4}{384u^8} + \frac{ip_r\dot{p}_r^3}{12u^{13/2}} \right) \right. \\
& - \frac{p_r^2\dot{p}_r^2}{64u^5} - \frac{ip_r^3\dot{p}_r}{96u^{7/2}} + \frac{p_r^4}{48u^2} \left. - \left(\frac{13\dot{p}_r^5}{1920u^{10}} - \frac{ip_r\dot{p}_r^4}{768u^{17/2}} + \frac{73p_r^2\dot{p}_r^3}{768u^7} + \frac{49ip_r^3\dot{p}_r^2}{384u^{11/2}} - \frac{35p_r^4\dot{p}_r}{384u^4} - \frac{89ip_r^5}{3840u^{5/2}} \right) \right. \\
& \left. + \left(\frac{109\dot{p}_r^6}{46080u^{12}} - \frac{ip_r\dot{p}_r^5}{64u^{21/2}} + \frac{137p_r^2\dot{p}_r^4}{1536u^9} + \frac{137ip_r^3\dot{p}_r^3}{1152u^{15/2}} - \frac{65p_r^4\dot{p}_r^2}{768u^6} - \frac{23ip_r^5\dot{p}_r}{640u^{9/2}} + \frac{p_r^6}{96u^3} \right) \right]. \tag{18}
\end{aligned}$$

These can then be eliminated by using Eq. (17), which, after an expansion in \dot{p}_r (i.e., in eccentricity) gives

$$\begin{aligned}
p_\varphi = & \frac{1}{\sqrt{u}} + \frac{\dot{p}_r}{2u^{5/2}} - \frac{\dot{p}_r^2}{8u^{9/2}} + \frac{\dot{p}_r^3}{16u^{13/2}} - \frac{5\dot{p}_r^4}{128u^{17/2}} \\
& + \frac{7\dot{p}_r^5}{256u^{21/2}} - \frac{21\dot{p}_r^6}{1024u^{25/2}} + \mathcal{O}(\dot{p}_r^7), \tag{19}
\end{aligned}$$

which yields

$$\begin{aligned}
\frac{1}{\sqrt{u}} = & p_\varphi \left(1 - \frac{\dot{p}_r}{2u^2} + \frac{3\dot{p}_r^2}{8u^4} - \frac{5\dot{p}_r^3}{16u^6} \right. \\
& \left. + \frac{35\dot{p}_r^4}{128u^8} - \frac{63\dot{p}_r^5}{256u^{10}} + \frac{231\dot{p}_r^6}{1024u^{12}} \right) + \mathcal{O}(\dot{p}_r^7). \tag{20}
\end{aligned}$$

Once this is inserted into Eq. (18), one precisely obtains Eq. (102) of [27] which we rewrite here for completeness in our notation

³ Corrections to the leading Newtonian order would enter at 2.5PN order in the waveform.

⁴ Here the round brackets collect terms at the same order in eccentricity

$$\begin{aligned}
\hat{H}_{22}^{\text{tail}} = & \frac{2\pi}{c^3} \left[p_\varphi u^3 + \frac{1}{4} i p_r u^2 - \left(\frac{7\dot{p}_r^3 p_\varphi}{96u^3} + \frac{7ip_r \dot{p}_r^2}{32u^2} - \frac{7}{32} p_r^2 \dot{p}_r p_\varphi - \frac{7}{96} i p_r^3 u \right) \right. \\
& + \left(\frac{3\dot{p}_r^4 p_\varphi}{32u^5} + \frac{ip_r \dot{p}_r^3}{12u^4} - \frac{p_r^2 \dot{p}_r^2 p_\varphi}{8u^2} - \frac{ip_r^3 \dot{p}_r}{96u} + \frac{1}{48} p_r^4 p_\varphi u \right) - \left(\frac{173\dot{p}_r^5 p_\varphi}{1920u^7} - \frac{ip_r \dot{p}_r^4}{768u^6} + \frac{p_r^2 \dot{p}_r^3 p_\varphi}{192u^4} + \frac{49ip_r^3 \dot{p}_r^2}{384u^3} - \frac{31p_r^4 \dot{p}_r p_\varphi}{384u} - \frac{89ip_r^5}{3840} \right) \\
& \left. + \left(\frac{97\dot{p}_r^6 p_\varphi}{1152u^9} - \frac{ip_r \dot{p}_r^5}{64u^8} + \frac{p_r^2 \dot{p}_r^4 p_\varphi}{16u^6} + \frac{137ip_r^3 \dot{p}_r^3}{1152u^5} - \frac{47p_r^4 \dot{p}_r^2 p_\varphi}{384u^3} - \frac{23ip_r^5 \dot{p}_r}{640u^2} + \frac{p_r^6 p_\varphi}{96} \right) \right] \quad (21)
\end{aligned}$$

Note that this expression, once interpreted within the EOB framework, is ambiguous, since here \dot{p}_r actually only refers to the time derivative of the *Newtonian* radial momentum obtained from the Newtonian equations of motion. Although there are no strong arguments that

may prevent us to promote it to the derivative of the *relativistic* radial momentum as defined within the resummed EOB dynamics, we prefer to simplify the logic and have an expression that *avoids* \dot{p}_r , and only uses (u, p_r, p_φ) . We thus use again Eq. (17) to transform Eq. (21) as

$$\begin{aligned}
\hat{H}_{22}^{\text{tail}} = & \frac{2\pi}{c^3} \left[\left(\frac{1931}{1440} - \frac{595p_\varphi^2 u}{384} + \frac{377p_\varphi^4 u^2}{128} - \frac{1747p_\varphi^6 u^3}{576} + \frac{347p_\varphi^8 u^4}{192} - \frac{381p_\varphi^{10} u^5}{640} + \frac{97p_\varphi^{12} u^6}{1152} \right) \right. \\
& - ip_r u^2 \left(\frac{9}{256} - \frac{29p_\varphi^2 u}{48} + \frac{39p_\varphi^4 u^2}{128} + \frac{5p_\varphi^6 u^3}{64} - \frac{61p_\varphi^8 u^4}{768} + \frac{p_\varphi^{10} u^5}{64} \right) \\
& - p_r^2 p_\varphi u^2 \left(\frac{53}{192} - \frac{13p_\varphi^2 u}{64} - \frac{17p_\varphi^4 u^2}{64} + \frac{49p_\varphi^6 u^3}{192} - \frac{p_\varphi^8 u^4}{16} \right) - ip_r^3 u \left(\frac{47}{288} - \frac{77p_\varphi^2 u}{128} + \frac{31p_\varphi^4 u^2}{64} - \frac{137p_\varphi^6 u^3}{1152} \right) \\
& \left. - p_r^4 p_\varphi u \left(\frac{35}{192} - \frac{125p_\varphi^2 u}{384} + \frac{47p_\varphi^4 u^2}{384} \right) + ip_r^5 \left(\frac{227}{3840} - \frac{23p_\varphi^2 u}{640} \right) + \frac{p_r^6 p_\varphi}{96} \right]. \quad (22)
\end{aligned}$$

In this way, the tail contribution is written with the same variables that we use for the instantaneous part. Moreover, leaving p_r and \dot{p}_r in the expressions leads to two issues: (i) the waveform becomes progressively unreliable at merger since p_r may become singular (although this is easily solved by replacing p_r with p_{r^*} , the momentum conjugate to some, suitably defined, Regge-Wheeler tortoise coordinate [41]); (ii) an expression that includes \dot{p}_r is evidently less efficient from the computational point of view. Finally, note that the absence of logarithmic terms in Eq. (22) is due to a dedicated phase redefinition performed already at the level of Eq. (12) that reabsorbs these terms along with the gauge parameter (see Sec. III C of [16] for further details).

B. Newton-factorized modes and 2PN residual noncircular corrections ($m \neq 0$)

The PN expanded waveform needs to be factorized and resummed in order to improve its strong-field behavior and to incorporate its information within state-of-the-art EOB models. The factorization (and resummation) scheme for the circular waveform was introduced long ago [42] and it has been progressively improved with suc-

cessive layers of sophistication [43–46] to achieve the best possible strong-field robustness and accuracy. To start with, Ref. [42] proposed to factor out the PN-expanded multipolar waveform for spin-aligned binaries as

$$h_{\ell m} = h_{\ell m}^{(N, \epsilon)} \hat{h}_{\ell m}, \quad (23)$$

where $h_{\ell m}^{(N, \epsilon)}$ indicates the Newtonian contribution, obtained by taking the ℓ -th time derivative of the mass or current multipole moments [47], while $\hat{h}_{\ell m}$ indicates the post-Newtonian corrections. In Eq. (23), $\epsilon = 0, 1$ depending on whether $\ell + m$ is even or odd. Since Ref. [42] was dealing with circularized binaries, $h_{\ell m}^{(N, \epsilon)}$ was simplified in the circular approximation, while the $\hat{h}_{\ell m}$ was then additionally factorized and resummed in various ways, allowing to obtain a remarkable level of agreement with the numerical results concerning very different binaries on quasi-circular orbits (from large mass ratios to comparable mass black holes). Refs [17, 24, 28] pointed out that an easy, and surprisingly accurate, way of generalizing the EOB resummed quasi-circular waveform to eccentric inspirals is to replace the quasi-circular Newtonian prefactor (for each multipole) with its general counterpart valid along generic orbits, i.e. without neglecting the time derivatives of r and Ω . The validity of this

prescription has then been tested extensively (including higher modes) by Ref. [19] in the test-particle limit and in Refs. [17, 24, 25] for comparable mass binaries, via detailed comparisons with the available NR simulations. To incorporate the 2PN results computed in this paper in such a factorization scheme, Eq. (23) is generalized to explicitly separate circular and noncircular contributions, that is

$$h_{\ell m} = h_{\ell m}^{(N,\epsilon)c} \hat{h}_{\ell m}^{(N,\epsilon)\text{nc}} \hat{h}_{\ell m}^c \hat{h}_{\ell m}^{\text{nc}}, \quad (24)$$

where we have

- (i) $h_{\ell m}^{(N,\epsilon)c}$: the Newtonian circular factor.
- (ii) $\hat{h}_{\ell m}^{(N,\epsilon)\text{nc}}$: the Newtonian *noncircular* correction, which is simply obtained from the corresponding mass and current Newtonian multipole moments, and whose expression is given in detail in Ref. [19].
- (iii) $\hat{h}_{\ell m}^c$: the PN residual circular correction, which is then resummed using several analytical prescriptions which we will briefly recall below. We use here the $\hat{h}_{\ell m}$'s functions entering the last avatar of the `TEOBResumS` waveform model [46, 48].
- (iv) $\hat{h}_{\ell m}^{\text{nc}}$: the PN residual *noncircular* correction, which are computed here for the first time.

Refs [17, 19, 24, 28] adopted the waveform factorized scheme of Eq. (24) for the waveform, although imposing $\hat{h}_{\ell m}^{\text{nc}} = 1$ for simplicity⁵. Our aim here is to explicitly determine the $\hat{h}_{\ell m}^{\text{nc}}$ noncircular correction factors at 2PN accuracy by factorizing the PN-expanded multipoles obtained in the previous section. The procedure is rather straightforward, although it needs the 2PN-expanded EOB equations of motion in order to recast the Newton-normalized relativistic correction into a meaningful residual PN-expansion. The generic Newtonian prefactors are all listed in Ref. [19], so there is no need to repeat here their derivation. Our factorization procedure consists in three steps: (i) starting from $h_{\ell m}$, we factor out the generic Newtonian prefactor and (ii) we replace the derivatives with the 2PN expanded equations of motion and expand the residual at 2PN, then (iii) we factor out the circular part in order to single out the residual noncircular correction $\hat{h}_{\ell m}^{\text{nc}}$. Indeed, for this prescription to work properly one has to be sure that no spurious poles are introduced by the factorization. Even though this is not the case for the majority of the spherical modes, all the modes with $m = 0$ happen to show this kind of problematic behavior, since their Newtonian factor is entirely noncircular and thus goes to zero in the circular limit.

⁵ Notice that the waveform factorization of Ref. [27] is different from the one proposed here, since it only factorizes the circular parts $h_{\ell m}^{(N,\epsilon)c} \hat{h}_{\ell m}$ while the parts that belong to the Newtonian noncircular factor are kept in PN-expanded form.

We defer to the next section the discussion of a possible alternative prescription for these modes.

Focusing here on the (2, 2) mode to exemplify the general factorization procedure, we have

$$h_{22}^{(N,0)c} = -8\sqrt{\frac{\pi}{5}}(r\Omega)^2 e^{-2i\varphi}, \quad (25)$$

$$h_{22}^{(N,0)\text{nc}} = 1 - \frac{\ddot{r}}{2r\Omega^2} - \frac{\dot{r}^2}{2(r\Omega)^2} + i\left(\frac{2\dot{r}}{r\Omega} + \frac{\dot{\Omega}}{2\Omega^2}\right). \quad (26)$$

The factorization of the general Newtonian factor $h_{\ell m}^{(N,\epsilon)c} \hat{h}_{\ell m}^{(N,\epsilon)\text{nc}}$ yields

$$\hat{h}_{\ell m}^{(\epsilon)} \equiv T_{2\text{PN}} \left[\frac{h_{\ell m}}{\left(h_{\ell m}^{(N,\epsilon)c} \hat{h}_{\ell m}^{(N,\epsilon)\text{nc}}\right)_{\text{EOMs}}} \right], \quad (27)$$

where the operator $T_{2\text{PN}}$ indicates that the expression within the square brackets is expanded at 2PN order. The subscript ‘‘EOMs’’ indicates that in the Newtonian term we replace the time-derivatives with the corresponding EOB equations of motion⁶. At this point the expression (27) is a rational function of (u, p_r, p_φ) of the type ‘‘1 + PN terms’’⁷.

Now that the PN factor is singled out we can also factor out its circular component

$$\hat{h}_{\ell m}^{(\epsilon)c} \equiv \lim_{p_r \rightarrow 0} \hat{h}_{\ell m}^{(\epsilon)}, \quad (28)$$

in order to obtain the total noncircular PN factor we are interested in, that is

$$\hat{h}_{\ell m}^{\text{nc}} \equiv T_{2\text{PN}} \left[\frac{\hat{h}_{\ell m}^{(\epsilon)}}{\hat{h}_{\ell m}^{(\epsilon)c}} \right], \quad (29)$$

where again $T_{2\text{PN}}$ indicates that we are retaining all combinations of powers of (u, p_r, p_φ) up to 2PN accuracy.

In this way the noncircular PN factor $\hat{h}_{\ell m}^{\text{nc}}$ amounts to a collection of all the relativistic noncircular contributions not yet included into the model. Moreover, we can split $\hat{h}_{\ell m}^{\text{nc}}$ into a tail factor and an instantaneous factor⁸, namely

$$\hat{h}_{\ell m}^{\text{nc}} = \hat{h}_{\ell m}^{\text{nc,tail}} \hat{h}_{\ell m}^{\text{nc,inst}}, \quad (30)$$

⁶ The equations of motion for the first time-derivatives can be computed directly from the EOB Hamiltonian; see Appendix B of Ref. [40] for their explicit expression at 2PN order. From there the computation of the higher order derivatives follows from a straightforward iteration.

⁷ We remind the reader that, as explained above, this factorization cannot be used for the $m = 0$ modes since they do not have a circular part to factorize. We will discuss this particular case in Sec. II C.

⁸ This splitting can be performed with ease since tail and instantaneous contributions are consistently well separated by the PN ordering

and eventually trade the radial momentum p_r for $p_{r_*} \equiv (A/B)^{1/2} p_r$, with $(A/B)^{1/2}$ truncated at 2PN accuracy. In addition, to simplify the structure of the analytical

expressions we are using, we expand each of the new factors in p_{r_*} up to the fourth order⁹. Focusing now on the $\ell = m = 2$ dominant mode, the so obtained tail factor is

$$\hat{h}_{22}^{\text{nc tail}} = 1 + \frac{1}{c^3} \frac{\pi}{(p_\varphi^2 u + 1)^2} \left[-i \left(\frac{9p_{r_*} u}{64} \hat{t}_{p_{r_*}}^{22} + \frac{457}{456} \frac{p_{r_*}^3}{(p_\varphi^2 u + 1)^2} \hat{t}_{p_{r_*}^3}^{22} \right) + \frac{5729}{1440} \frac{p_{r_*}^2 p_\varphi u}{(p_\varphi^2 u + 1)} \hat{t}_{p_{r_*}^2}^{22} + \frac{133}{80} \frac{p_{r_*}^4 p_\varphi}{(p_\varphi^2 u + 1)^3} \hat{t}_{p_{r_*}^4}^{22} \right] \quad (31)$$

where $(\hat{t}_{p_{r_*}}^{22}, \hat{t}_{p_{r_*}^3}^{22}, \hat{t}_{p_{r_*}^2}^{22}, \hat{t}_{p_{r_*}^4}^{22})$ are the following polynomials in $y \equiv p_\varphi^2 u$ (with alternate signs)

$$\hat{t}_{p_{r_*}}^{22} = 1 + \frac{24341}{405} y - \frac{290}{3} y^2 + \frac{1606}{9} y^3 - \frac{13979}{81} y^4 + 101 y^5 - \frac{1504}{45} y^6 + \frac{388}{81} y^7, \quad (32)$$

$$\hat{t}_{p_{r_*}^3}^{22} = 1 + \frac{46372}{2285} y - \frac{134587}{2285} y^2 + \frac{45492}{457} y^3 - \frac{54397}{457} y^4 + \frac{43924}{457} y^5 - \frac{112697}{2285} y^6 + \frac{32212}{2285} y^7 - \frac{776}{457} y^8, \quad (33)$$

$$\hat{t}_{p_{r_*}^2}^{22} = 1 - \frac{27552}{5729} y + \frac{2910}{337} y^2 - \frac{70015}{5729} y^3$$

$$+ \frac{61785}{5729} y^4 - \frac{34674}{5729} y^5 + \frac{10952}{5729} y^6 - \frac{1455}{5729} y^7, \quad (34)$$

$$\hat{t}_{p_{r_*}^4}^{22} = 1 - \frac{35260}{1197} y + \frac{78500}{1197} y^2 - \frac{34825}{342} y^3 + \frac{265975}{2394} y^4 - \frac{96727}{1107} y^5 + \frac{6305}{171} y^6 - \frac{3245}{342} y^7 + \frac{2425}{2394} y^8. \quad (35)$$

The instantaneous factor is conveniently separated in amplitude and phase

$$h_{22}^{\text{nc inst}} = f_{22}^{\text{nc inst}} e^{i\delta_{22}^{\text{nc inst}}}, \quad (36)$$

which respectively are given by

$$f_{22}^{\text{nc inst}} = 1 - \frac{p_{r_*}^2}{c^2 (p_\varphi^2 u + 1)^3} \left[\left(\frac{1}{14} - \frac{31\nu}{14} \right) \hat{f}_{1^{\text{1PN}}}^{22} + \frac{p_{r_*}^2}{u (p_\varphi^2 u + 1)^2} \left(\frac{5}{7} - \frac{8\nu}{7} \right) \hat{f}_{p_{r_*}^{1\text{PN}}}^{22} \right] + \frac{p_{r_*}^2}{c^4 (p_\varphi^2 u + 1)^4} \left[u \left(\frac{65}{252} + \frac{211\nu}{126} + \frac{139\nu^2}{63} \right) \hat{f}_{u^{2\text{PN}}}^{22} + \frac{p_{r_*}^2}{(p_\varphi^2 u + 1)^2} \left(\frac{1613}{504} - \frac{1567\nu}{504} - \frac{71\nu^2}{72} \right) \hat{f}_{p_{r_*}^{1\text{PN}}}^{22} \right], \quad (37)$$

$$\delta_{22}^{\text{nc inst}} = \frac{1}{c^2} \frac{p_{r_*} p_\varphi}{(p_\varphi^2 u + 1)^2} \left[u \left(\frac{25}{21} - \frac{18\nu}{7} \right) \hat{\delta}_{u^{1\text{PN}}}^{22} + \frac{p_{r_*}^2}{(p_\varphi^2 u + 1)^2} \left(\frac{55}{21} - \frac{34\nu}{7} \right) \hat{\delta}_{p_{r_*}^{1\text{PN}}}^{22} \right] + \frac{1}{c^4} \frac{p_{r_*} p_\varphi u}{(p_\varphi^2 u + 1)^3} \left[u \left(\frac{7}{27} - \frac{416\nu}{189} - \frac{652\nu^2}{189} \right) \hat{\delta}_{u^{2\text{PN}}}^{22} + \frac{p_{r_*}^2}{(p_\varphi^2 u + 1)^2} \left(\frac{20945}{2646} - \frac{17321}{1323}\nu + \frac{134}{1323}\nu^2 \right) \hat{\delta}_{p_{r_*}^{2\text{PN}}}^{22} \right]. \quad (38)$$

Similarly to the tail factor, the functions $(\hat{f}_i, \hat{\delta}_i)$ are polynomials in y whose explicit expressions are

$$\hat{f}_{1^{\text{1PN}}}^{22} = 1 - \frac{7(1+3\nu)}{1-31\nu} y - \frac{(451-177\nu)}{3-93\nu} y^2 - \frac{3(3+5\nu)}{1-31\nu} y^3, \quad (39)$$

$$\hat{f}_{p_{r_*}^{1\text{PN}}}^{22} = 1 - \frac{65-216\nu}{3(5-8\nu)} y - \frac{5(115-72\nu)}{3(5-8\nu)} y^2 + \frac{305-264\nu}{3(5-8\nu)} y^3, \quad (40)$$

$$\hat{f}_{u^{2\text{PN}}}^{22} = 1 - \frac{44767+28618\nu-7276\nu^2}{42(65+422\nu+556\nu^2)} y + \frac{132507-87244\nu-29672\nu^2}{14(65+422\nu+556\nu^2)} y^2 - \frac{134789+27920\nu+9472\nu^2}{42(65+422\nu+556\nu^2)} y^3$$

⁹ We have verified that this choice gives an excellent approximation to the full expressions for all cases considered.

$$\begin{aligned}
& - \frac{3(637 - 1448\nu + 512\nu^2)}{2(65 + 422\nu + 556\nu^2)} y^4 \\
& - \frac{3(418 + 355\nu + 710\nu^2)}{7(65 + 422\nu + 556\nu^2)} y^5, \quad (41) \\
\hat{f}_{p_{r_*}^{22}}^{22} = 1 & - \frac{16399 - 169738\nu - 9902\nu^2}{7(1613 - 1567\nu - 497\nu^2)} y \\
& - \frac{256835 - 145513\nu + 7405\nu^2}{4839 - 4701\nu - 1491\nu^2} y^2 \\
& + \frac{4(292018 - 194489\nu - 76057\nu^2)}{21(1613 - 1567\nu - 497\nu^2)} y^3 \\
& - \frac{449937 + 29671\nu - 80119\nu^2}{7(1613 - 1567\nu - 497\nu^2)} y^4 \\
& - \frac{34361 - 33826\nu - 3518\nu^2}{7(1613 - 1567\nu - 497\nu^2)} y^5 \\
& + \frac{15(5 - 13\nu + \nu^2)}{1613 - 1567\nu - 497\nu^2} y^6, \\
\hat{\delta}_{u^{1\text{PN}}}^{22} = 1 & + \frac{125 - 102\nu}{25 - 54\nu} y, \quad (42) \\
\hat{\delta}_{p_{r_*}^{1\text{PN}}}^{22} = 1 & + \frac{42(5 - 2\nu)}{55 - 102\nu} y - \frac{35(7 - 6\nu)}{55 - 102\nu} y^2, \quad (43) \\
\hat{\delta}_{u^{2\text{PN}}}^{22} = 1 & + \frac{39761 - 20950\nu - 21236\nu^2}{14(49 - 416\nu - 652\nu^2)} y \\
& - \frac{3(3709 - 2556\nu - 408\nu^2)}{14(49 - 416\nu - 652\nu^2)} y^2 \\
& - \frac{3(767 - 2551\nu - 1070\nu^2)}{7(49 - 416\nu - 652\nu^2)} y^3, \quad (44) \\
\hat{\delta}_{p_{r_*}^{2\text{PN}}}^{22} = 1 & + \frac{66624 - 84120\nu + 300789\nu^2}{41890 - 69284\nu + 536\nu^2} y \\
& - \frac{292601 - 144464\nu^2 - 298528\nu}{41890 - 69284\nu + 536\nu^2} y^2 \\
& + \frac{7(28217 + 17672\nu - 1664\nu^2)}{41890 - 69284\nu + 536\nu^2} y^3
\end{aligned}$$

$$+ \frac{3(6473 - 23284\nu + 6856\nu^2)}{41890 - 69284\nu + 536\nu^2} y^4. \quad (45)$$

We anticipate here that in Sec. III A we will argue that the polynomials $\hat{t}_{p_{r_*}}^{\ell m}(y)$ of the tail factor need a proper resummation in order for the 2PN corrections to have a robust behavior in strong field.

C. 2PN noncircular corrections for the $m = 0$ modes

As mentioned in the previous section, the factorization scheme presented therein cannot be applied successfully to the spherical modes with $m = 0$, because of the vanishing of their Newtonian factor in the circular limit. Nevertheless, we can still build a model for them that is well behaved and incorporates the 2PN noncircular information of the starting PN-expanded waves. In particular the alternative to Eq. (24) we propose in this case is

$$h_{\ell 0} = \hat{S}_{\text{eff}} \left(h_{\ell 0}^{(N, \epsilon)} + \hat{h}_{\ell 0} \right), \quad (46)$$

where the PN correction, which indeed is fully noncircular, is given by

$$\hat{h}_{\ell 0} = T_{2\text{PN}} \left[\left(\frac{h_{\ell 0} - h_{\ell 0}^{(N, \epsilon)}}{\hat{S}_{\text{eff}}} \right)_{\text{EOMs}} \right]. \quad (47)$$

Similarly to the other prescription, this quantity comes out naturally split into an instantaneous and a tail part,

$$\hat{h}_{\ell 0} = \hat{h}_{\ell 0}^{\text{tail}} + \hat{h}_{\ell 0}^{\text{inst}}. \quad (48)$$

Here we prefer to express the PN corrections using $(r, p_{r_*}, \dot{p}_{r_*})$, without writing \dot{p}_{r_*} in terms of (r, p_{r_*}, p_φ) . The reason is that in this case writing the corrections in p_φ leads to terms that do not vanish in the circular limit since they are not proportional to powers of p_{r_*} ¹⁰. The corresponding PN corrections for the mode (2, 0) read

$$\begin{aligned}
\hat{h}_{20}^{\text{tail}} &= -\frac{\pi}{960u^{10}c^3} \sqrt{\frac{\dot{p}_{r_*} + u^2}{6u}} \left[960\dot{p}_{r_*} u^{10} + 960\dot{p}_{r_*}^2 u^8 + 240 \left(-3\dot{p}_{r_*}^3 u^6 + p_{r_*}^2 \dot{p}_{r_*} u^9 \right) + 80u^4 \left(7\dot{p}_{r_*}^4 + 2p_{r_*}^4 u^6 \right) \right. \\
&\quad \left. - 5 \left(95\dot{p}_{r_*}^5 u^2 + 26p_{r_*}^2 \dot{p}_{r_*}^3 u^5 + 11p_{r_*}^4 \dot{p}_{r_*} u^8 \right) + \left(417\dot{p}_{r_*}^6 + 110p_{r_*}^2 \dot{p}_{r_*}^4 u^3 - 45p_{r_*}^4 \dot{p}_{r_*}^2 u^6 + 2p_{r_*}^6 u^9 \right) \right] \quad (49) \\
\hat{h}_{20}^{\text{inst}} &= \frac{1}{14\sqrt{6}u^2c^2} \left[\dot{p}_{r_*} u^2 (-19 + \nu) + 3 \left(\dot{p}_{r_*}^2 - p_{r_*}^2 u^3 \right) (3 + 5\nu) + 6p_{r_*}^2 \dot{p}_{r_*} u (3 + 5\nu) + 3p_{r_*}^4 u^2 (3 + 5\nu) \right] \\
&\quad + \frac{1}{504\sqrt{6}u^3c^4} \left[\dot{p}_{r_*} u^4 (1052 - 2803\nu - 53\nu^2) + p_{r_*}^2 u^5 (-743 + 7009\nu - 571\nu^2) + 3\dot{p}_{r_*}^2 u^2 (545 - 430\nu + 28\nu^2) \right]
\end{aligned}$$

¹⁰ Specifically there are contributions that vanish in the circular limit only when p_φ is replaced with its corresponding quasi-

circular PN expansion in terms of u .

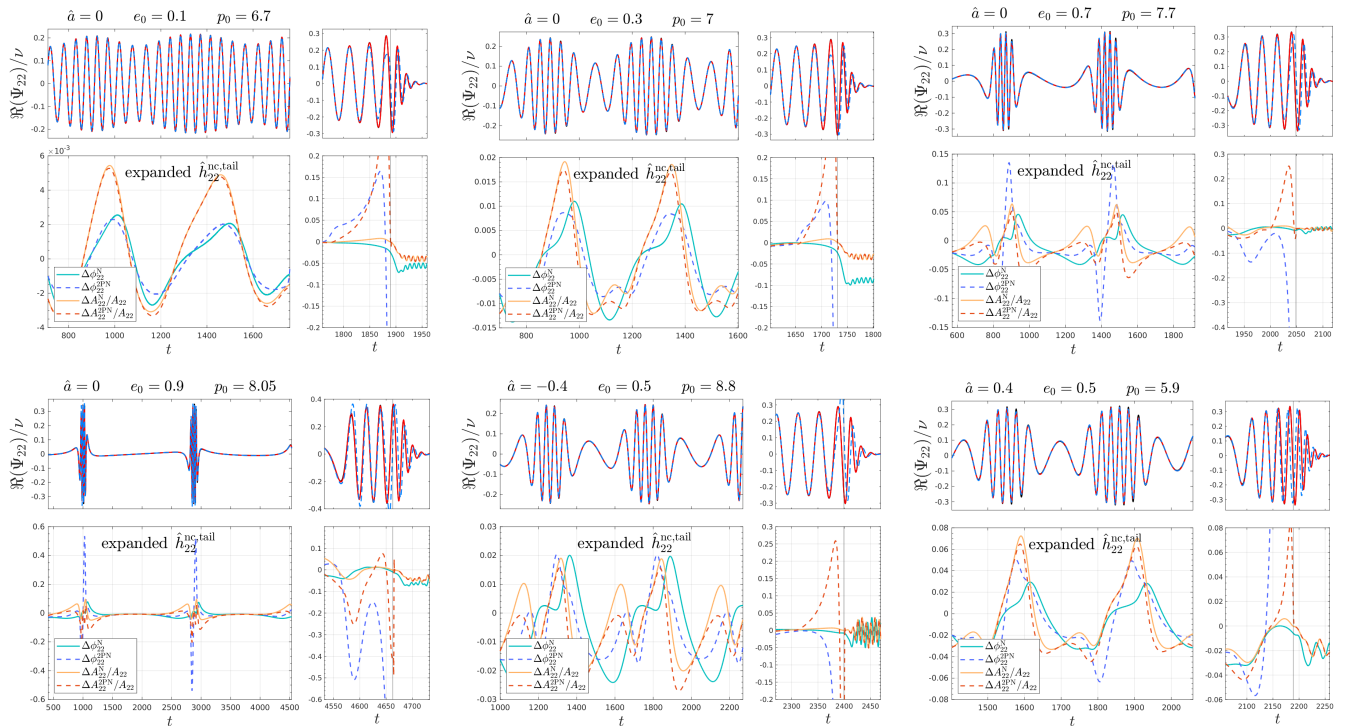


FIG. 1. Comparisons with *nonresummed* noncircular tail factor: comparing analytical and numerical $\ell = m = 2$ waveforms for the transition from inspiral to plunge of a test-particle on a Kerr black hole with spin parameter \hat{a} . We consider different configurations with $\nu = 10^{-3}$. Each panel displays the numerical waveform (black, indistinguishable) and two EOB waveforms: (i) the solid-red one with noncircular information only in the Newtonian prefactor, (ii) the dashed-blue one with noncircular 2PN corrections to the *nonresummed* tail $\hat{h}_{22}^{\text{nc,tail}}$ of Eq. (31). The bottom panel shows both the phase differences and the relative amplitude differences with respect to the numerical waveform. We use dashed lines for the differences corresponding to the wave with 2PN corrections. The vertical line marks the merger-time, corresponding to the peak of the numerical amplitude.

$$\begin{aligned}
 & -3\dot{p}_{r_*}^3 \left(79 + 25\nu + 5\nu^2 \right) + 18p_{r_*}^2 \dot{p}_{r_*} u^3 \left(81 + 404\nu + 65\nu^2 \right) - 9p_{r_*}^2 \dot{p}_{r_*}^2 u \left(115 + 121\nu + 65\nu^2 \right) \\
 & + 6p_{r_*}^4 u^4 \left(79 + 133\nu + 185\nu^2 \right) - 9p_{r_*}^4 \dot{p}_{r_*} u^2 \left(151 + 217\nu + 125\nu^2 \right) - 3p_{r_*}^6 u^3 \left(187 + 313\nu + 185\nu^2 \right) \Big]. \quad (50)
 \end{aligned}$$

Inspired by what we did here, we also rewrote the 2PN noncircular corrections for the modes $m \neq 0$ (both the instantaneous and the tail part) by replacing p_φ by its expression in terms of $(u, p_{r_*}, \dot{p}_{r_*})$ using the 2PN-accurate equations of motion. Since this approach lays outside the main logic of the paper, we will discuss it separately in Appendix C.

III. WAVEFORM VALIDATION: ECCENTRIC INSPIRALS IN THE LARGE MASS RATIO LIMIT

Let us now move to explore the performance of our new factorized waveform, starting from the case of elliptic inspirals in the large mass ratio limit. We recall that Ref. [19] validated the simple Newton-factorized waveform, without the 2PN noncircular correction, in the test-mass limit, i.e. considering the motion of a test-particle

around a Kerr black hole. The validation was relying on comparisons between the analytic EOB waveform and the numerical solution of the Teukolsky equation, obtained using the 2+1 time-domain code *Teukode* [49]. It was considered either: (i) the geodesic motion along elliptic orbits and (ii) the full transition from the eccentric inspiral to merger and ringdown. The outcome of that study was that, even without the 2PN correction, the analytic waveform delivers a rather accurate approximation of the exact waveform up to mild values of the initial eccentricity, both for amplitude and phase (see e.g. Fig. 13 of Ref. [19]). To start with, we use precisely the expressions for $(\hat{h}_{22}^{\text{nc,tail}}, \hat{h}_{22}^{\text{nc,inst}})$ given in Eqs. (31), (36) and redo the comparison of Ref. [19], where the interested reader can find more technical details regarding the dynamics. The eccentric numerical waveforms used in this work are listed in Table I. We also recall that the quasi-circular part of the waveform we use is precisely the same of Ref. [19]. In

TABLE I. Numerical eccentric simulations considered in this work. We use $\nu = 10^{-3}$ to drive the transition from inspiral to merger. For each eccentric simulation we report the spin parameter \hat{a} , the initial/final values of eccentricity and semilatus rectum, and the merger time t_{mrg} . The final values of eccentricity and semilatus rectum are evaluated at t_{sep} since they are not defined for later times, where t_{sep} is the time when the semilatus rectum equals the separatrix and the radial turning points cease to exist (definitions of e , p and separatrix written in terms of radial turning points can be found in Sec.II A of Ref. [19]).

\hat{a}	e_0	p_0	e_{sep}	p_{sep}	t_{sep}	t_{mrg}
0.0	0.1	6.700	0.107	6.213	1459	1890
0.0	0.3	7.000	0.305	6.611	1382	1731
0.0	0.7	7.700	0.694	7.388	1916	2049
0.0	0.9	8.050	0.891	7.783	4570	4663
-0.4	0.5	8.800	0.501	8.426	2182	2387
0.4	0.5	5.900	0.490	5.415	2092	2192

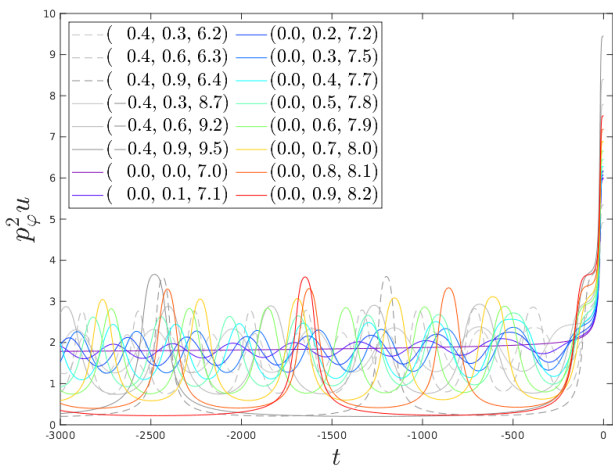


FIG. 2. Last part of the time evolution of $p_\varphi^2 u$ for different combinations of (\hat{a}, e_0, p_0) . Note that during the plunge $p_\varphi^2 u$ can grow up to ~ 10 . This growth is mostly responsible of the unacceptably large analytical/numerical phase disagreement during the plunge, at 2PN-accuracy, seen in Fig. 1.

Fig. 1 we report different configurations aiming at comprehensively cover the parameter space. The first four panels from left to right refer to nonspinning binaries with increasing eccentricity $e_0 = (0.1, 0.3, 0.7, 0.9)$, while the last two panels refer to two spinning binaries with $\hat{a} = \pm 0.4$ and initial eccentricity $e_0 = 0.5$. For low eccentricity, up to $e \simeq 0.3$, the 2PN corrections improve the phase agreement during the inspiral, but for higher eccentricity the phase of the wave with only Newtonian corrections is more accurate. Moreover, in all the cases the analytical/numerical agreement visibly deteriorates as one gets closer to plunge and merger, both at the level of the phase and of the amplitude. Indeed, careful analysis of the geodesic case highlights that the reliable be-

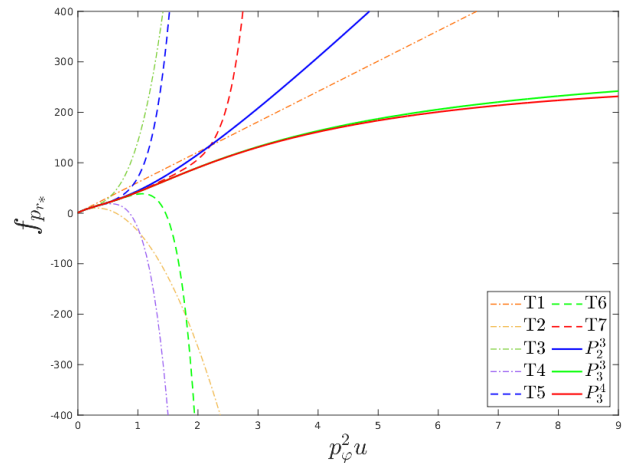


FIG. 3. Behavior of various truncations of the $\hat{i}_{pr_*}^{22}$ polynomial of Eq. (32). The various truncations of $\hat{i}_{pr_*}^{22}$ oscillate and become very large for values of $p_\varphi^2 u$ of the order of those reached during the plunge, see Fig. 2. A straightforward diagonal Padé approximant tapers the behavior of the polynomials in strong field and eventually improves the behavior of the waveform there.

havior of the waveform during the eccentric inspiral is related to *cancellations* between the tail and instantaneous factors. By contrast, the inaccurate behavior of the analytical waveform during the plunge is related to the fact that the quantity $p_\varphi^2 u$, which appears everywhere in Eq. (31), becomes rather large during late plunge up to merger, as shown in Fig. 2. The growth of $p_\varphi^2 u$ makes the eccentric corrections too large with respect to the instantaneous terms and the cancellations mentioned above are no longer possible, leading to the observed loss in accuracy. This issue is also responsible for the large phase disagreement near the periastra of configurations with high eccentricity. To cure this behavior we need to implement specific resummation strategies, as we will discuss in the next section.

A. Resummation of the hereditary residual noncircular factor

Let us start this section by going back to the structure of the tail factor. In its native form, it is a 1.5PN accurate term that is expanded in eccentricity up to e^6 . We have seen in the sections above that this expansion in eccentricity, after the factorization of the Newtonian contribution, can be recasted in a rational function of (u, p_r, p_φ) , Eq. (31). In particular, the expansion in the eccentricity e can be rewritten as an expansion in the radial momentum p_r and \dot{p}_r , which can be subsequently recasted in a form where one is left with several polynomials in $y = p_\varphi^2 u$ that are all, formally, at *Newtonian order*. Figure 2 shows the behavior of y versus time for differ-

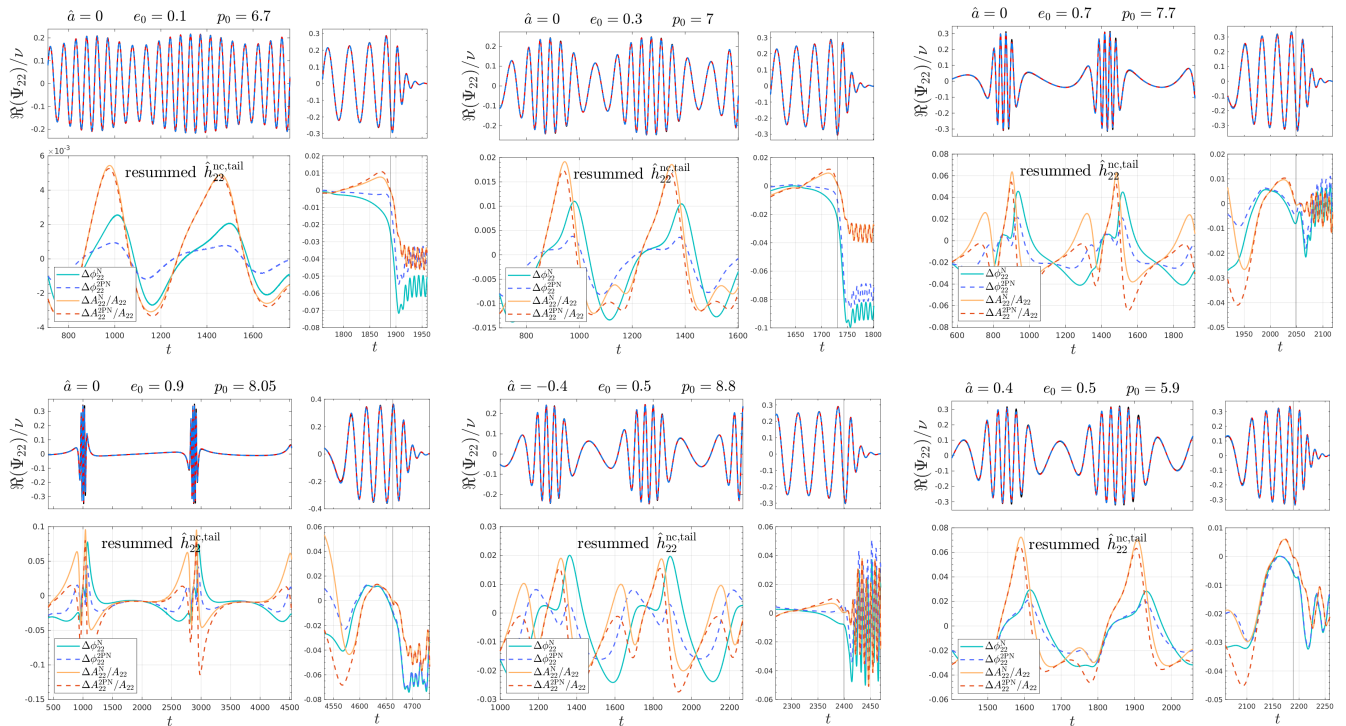


FIG. 4. Comparisons with *resummed* noncircular tail factor: comparing analytical and numerical $\ell = m = 2$ waveforms for the transition from inspiral to plunge of a test-particle on a Kerr black hole with spin parameter \hat{a} . We consider different configurations with $\nu = 10^{-3}$. Each panel displays the numerical waveform (black, indistinguishable) and two EOB waveforms: (i) the solid-red one with noncircular information only in the Newtonian prefactor, (ii) the dashed-blue one with noncircular 2PN corrections with the tail $\hat{h}_{22}^{\text{nc,tail}}$ of Eq. (31) *resummed* following the procedure discussed in Sec. III A. The bottom panel shows both the phase differences and the relative amplitude differences with respect to the numerical waveform. We use dashed lines for the differences corresponding to the wave with 2PN corrections. The vertical line marks the merger-time, corresponding to the peak of the numerical amplitude. The resummation strongly improves the analytical/numerical agreement with respect to Fig. 1.

ent eccentric configurations: y is *not* a small quantity¹¹. For the nonspinning configurations considered in Fig. 2, it oscillates between 0 and 4 during the eccentric inspiral and may reach values ~ 7 up to merger. We thus wonder whether an argument that can be so large may eventually generate some nonphysical behavior for the functions ($\hat{t}_{p_{r_*}}^{22}, \hat{t}_{p_{r_*}^2}^{22}, \hat{t}_{p_{r_*}^3}^{22}, \hat{t}_{p_{r_*}^4}^{22}$), especially given the fact that they stem from an expansion in eccentricity within a PN expansion. As an example, Fig. 3 shows various truncations of $\hat{t}_{p_{r_*}}^{22}$. One sees that: (i) the various polynomial truncations become very large for values of y of the order of those of the late inspiral and (ii) the sign alternation gives an oscillatory behavior that visually resembles the one that is typical of truncated PN expansions of the energy flux of a test-particle orbiting a Schwarzschild black hole on circular orbits (see e.g. Ref. [50]). On the basis of this analogy, and with the understanding that $\hat{t}_{p_{r_*}}^{22}$ is a suitable recasting of an expansion in the eccentricity (or

in p_{r_*} and \dot{p}_r), we *interpret* the polynomial expression of $\hat{t}_{p_{r_*}}^{22}$ as the *truncated expansion* of an unknown function of y that is expanded around $y = 0$. As such, this function can be resummed, and we do it straightforwardly applying Padé approximants. In Fig. 3 we exhibit several (diagonal or nearly diagonal) Padé approximant that resum different truncation of the polynomials. The Padé stabilizes the truncated series (e.g. the results obtained resumming the truncation up to y^6 is equivalent to the Padé of the full polynomial up to y^7) and considerably lowers the value of the function reached for $y \simeq 6$. Although we do not have a proof, the consistency between the P_2^3, P_3^3 and P_3^4 approximants seems to suggest that the residual polynomial $\hat{t}_{p_{r_*}}^{22}$ is indeed the Taylor expansion of some unknown function and its resummation does make sense. A completely analogous behavior is found for the other three functions ($\hat{t}_{p_{r_*}^2}^{22}, \hat{t}_{p_{r_*}^3}^{22}, \hat{t}_{p_{r_*}^4}^{22}$), which are thus also resummed. In practice, we replace the Taylor-expanded functions with ($P_3^4[\hat{t}_{p_{r_*}}^{22}], P_4^4[\hat{t}_{p_{r_*}^2}^{22}], P_3^3[\hat{t}_{p_{r_*}^3}^{22}], P_4^4[\hat{t}_{p_{r_*}^4}^{22}]$). The quality of the resummed $\ell = m = 2$ waveform is shown in Fig. 4, which is the analogous of Fig. 1 where the Taylor-expanded functions have been replaced by the Padé resummed ones. The analytical/numerical phase agree-

¹¹ Note that $y = p_\varphi^2 u = 1$ at Newtonian order for circular orbits, where $p_\varphi = p_\varphi^{\text{N,circ}} = 1/\sqrt{u}$.

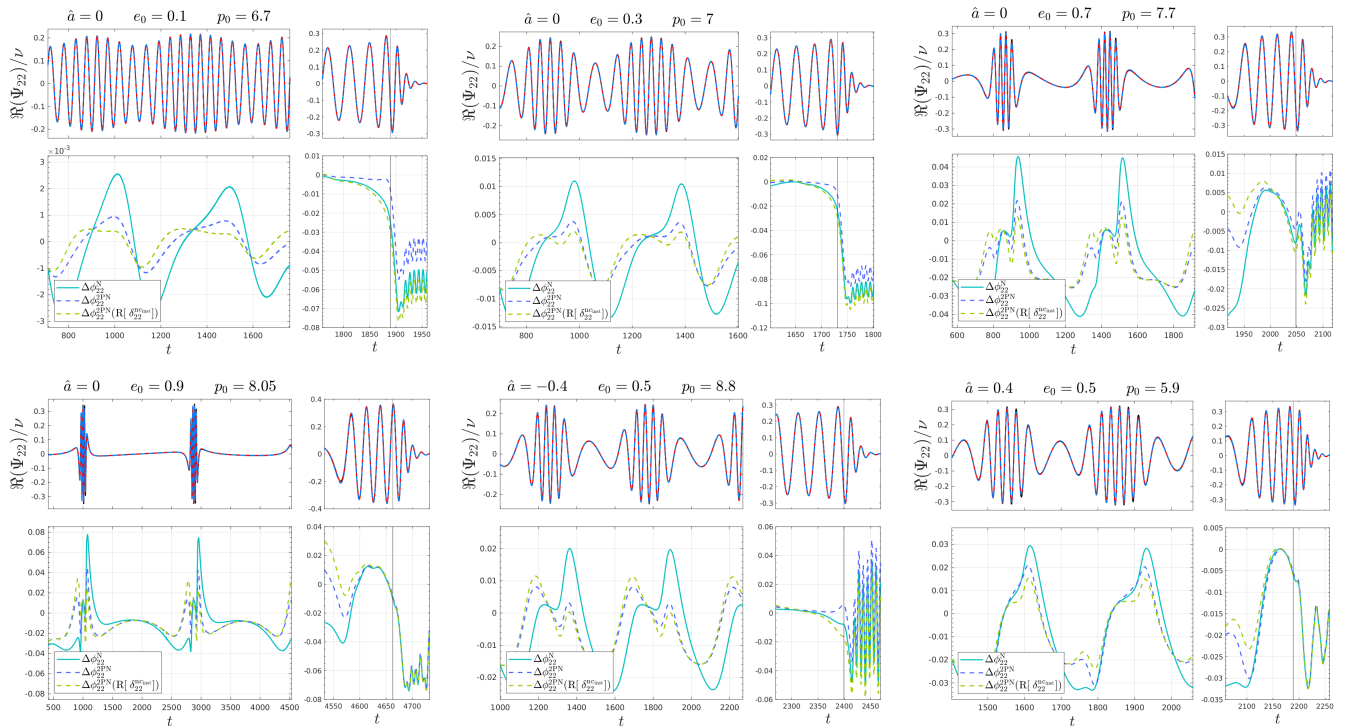


FIG. 5. Same configurations of Fig. 4, but here we focus on the phase and we show also the analytical/numerical agreement obtained considering the resummed noncircular tail and the resummed instantaneous noncircular correction (dashed light green). The color scheme of the other differences is the same of Fig. 4: solid light blue for the wave with only the generic Newtonian prefactor, dashed blue for the wave with 2PN corrections with resummed tail and Taylor expanded instantaneous corrections.

ment not only improves (and largely) during the plunge and merger phase, but also during the eccentric inspiral. In particular, it is now evident the improvement with respect to the simple Newtonian prefactor all over, notably without pathological behaviors towards merger.

B. Resummation of the instantaneous residual noncircular factor

A priori, the same resummation strategy should be implemented for the residual instantaneous 2PN corrections which exhibits an analogous structure with polynomials in y . We explore this on both the residual noncircular amplitude correction f_{22}^{ncinst} and phase $\delta_{22}^{\text{ncinst}}$. For the amplitude, we find that any choice of Padé approximant for the various residual polynomials in y of Eq. (37) develops spurious poles, so that our resummation strategy cannot be pursued¹². This is not of great concern, since the generic Newtonian prefactor alone already gives an excellent approximation to the exact waveform. This can be clearly seen in Fig. 4, where the amplitudes with

and without 2PN noncircular corrections produce analytical/numerical relative differences that are comparable.

By contrast, for the instantaneous residual noncircular phase given in Eq. (38) the procedure is robust. More precisely, we resum the y -polynomials $\hat{\delta}_{22}^{22}$ of Eq. (38) using the Padé approximants $P_0^1[\hat{\delta}_{u_{1\text{PN}}}^{22}]$, $P_1^1[\hat{\delta}_{p_{r_*}^{1\text{PN}}}^{22}]$, $P_2^1[\hat{\delta}_{u_{2\text{PN}}}^{22}]$, and $P_1^1[\hat{\delta}_{p_{r_*}^{2\text{PN}}}^{22}]$. Note that the latter polynomial, written explicitly in Eq. (45), is at fourth-order in y , but we only use $O(y^2)$ -terms since the P_1^2 approximant produces unphysical behaviors for large y and the other higher-order Padé approximants have spurious poles in the equal-mass case. The improvements introduced by this resummation are shown in Fig. 5, where we compare the analytical/numerical phase differences of the new obtained waveform with the phase differences of the previous prescription, where the resummation was applied only to the eccentric hereditary terms. While a slight improvement in the phase accuracy can be seen in the reported cases¹³, the resummation of the instantaneous phase correction is less relevant than the resummation of the eccentric tail. Nonetheless, through this paper we will use the resummed instantaneous phase as

¹² This is the current situation with the 2PN-accurate waveform. The procedure will have to be investigated again in the future using results at 3PN order.

¹³ The only exception is the $\hat{a} = -0.4$ case, but bear in mind that we are not including spin terms in the noncircular corrections.

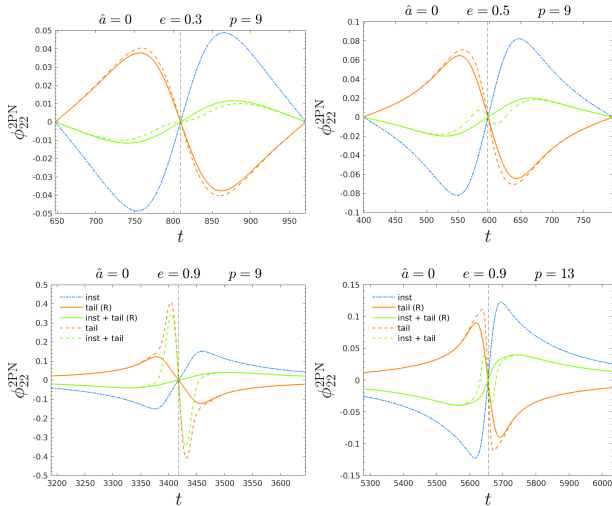


FIG. 6. Instantaneous and hereditary noncircular 2PN corrections to the quadrupolar phase for four nonspinning geodesic cases $(e, p) = (0.3, 9), (0.5, 9), (0.9, 9), (0.9, 13)$. The instantaneous phase corrections are shown with dash-dotted blue lines, while the orange lines are for the phase contributions of the resummed eccentric tail (dashed for the expanded results and solid for the resummed ones). The corresponding sums between instantaneous and hereditary are shown in green with the same style-scheme of the considered tail. The vertical dashed line marks the periastron passage. For $e = 0.9$ we do not show the whole radial period in order to highlight the periastron.

our default option for the 2PN noncircular corrections.

C. Discussion: Compensation between instantaneous and hereditary contributions

The results shown in the section above require some discussion. On the one hand, as noted in previous works [17, 19], the Newtonian prefactor is quite effective in capturing the behavior of the correct waveform, both in amplitude and phase. As a consequence, the missing analytical information is rather tiny and special resummation procedures should be implemented to make the additional PN information really useful. By separately analyzing the cumulative action of the instantaneous and hereditary contributions to the waveform one finds that the good performance of our resummed waveform is due to *compensations* between the two. This eventually yields only a tiny correction to the Newtonian noncircular prefactor. More importantly, one notices that the instantaneous contributions alone tend to *overestimate* the analytical phase, eventually yielding phase differences with the numerical waveform that are *larger* than those obtained with the simple Newtonian prefactor. This is very clear when inspecting Fig. 6 that illustrates this effect for four different geodesic configurations: $(e, p) = (0.3, 9), (0.5, 9), (0.9, 9), (0.9, 13)$. Indeed at high eccentricity and relatively small semilatus rectum, the

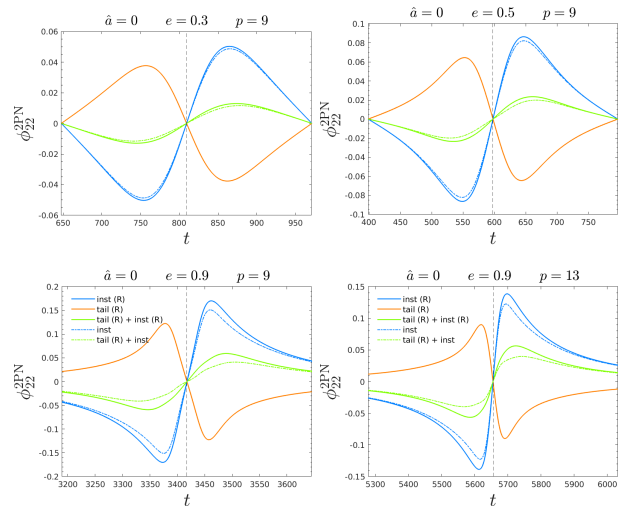


FIG. 7. Analogous to Fig. 6, but here we focus on the relevance of the resummation for the instantaneous part. The orange solid line is the phase contribution of the resummed eccentric tail, while the blue lines correspond to the instantaneous phase contributions: dash-dotted for the nonresummed results, solid line for the resummed ones. The corresponding sums between tail and instantaneous are shown in green with the same style-scheme of the instantaneous terms. The vertical dashed line marks the periastron passage. For $e = 0.9$ we do not show the whole radial period in order to highlight the periastron.

resummation of the tail factor is a crucial aspect in order to have a compensation between instantaneous and hereditary terms. The benefits of the resummation can be seen even at milder eccentricities or larger semilatus recta, even if it is less crucial. In Fig. 7 we also show the effect of the resummation of the instantaneous factor for the same configurations considered in Fig. 6. While the effect of the resummation is clearly visible, it is also evident that the resummation of the instantaneous part is less relevant than the tail resummation.

D. Subdominant modes

The factorization and resummation outlined in the previous section can be similarly applied to higher modes. The resulting factorized (though nonresummed) expressions are all reported in Appendix A. We explicitly discuss analytical/numerical comparisons for the modes $(2, 1), (3, 3), (3, 2)$ and $(4, 4)$. While for the modes $(2, 1)$ and $(3, 3)$ the tail contribution is present, for the modes $(3, 2)$ and $(4, 4)$ it is absent, at 2PN order. This has implications on the waveform performance, as we will see below. We use several Padé approximants. To make this clear, it is convenient to rewrite here explicitly the tail factor at 2PN order for the modes $(2, 1), (3, 3)$

$$\hat{h}_{21}^{\text{nc tail}} = 1 + \frac{1}{c^3} \pi \left[-i \left(\frac{3029}{1920} u p_{r_*} \hat{t}_{p_{r_*}}^{21} + \frac{619}{576} p_{r_*}^3 \hat{t}_{p_{r_*}^3}^{21} \right) + \frac{635}{768} \frac{p_{r_*}^2}{p_\varphi} \hat{t}_{p_{r_*}^2}^{21} - \frac{61}{256} \frac{p_{r_*}^4}{p_\varphi u} \hat{t}_{p_{r_*}^4}^{21} \right], \quad (51)$$

$$\begin{aligned} \hat{h}_{33}^{\text{nc tail}} = 1 + \frac{1}{c^3} \frac{\pi}{p_\varphi^2 (7 + 2p_\varphi^2 u)^2} & \left[-i \left(\frac{4763}{384} p_{r_*} \hat{t}_{p_{r_*}}^{33} - \frac{4763}{24} \frac{p_\varphi^2 p_{r_*}^3}{p_\varphi^2 u^2 (7 + 2p_\varphi^2 u)^2} \hat{t}_{p_{r_*}^3}^{33} \right) \right. \\ & \left. + \frac{4763}{96} \frac{p_{r_*}^2}{p_\varphi u (7 + 2p_\varphi^2 u)} \hat{t}_{p_{r_*}^2}^{33} + \frac{4763}{6} \frac{p_\varphi^3 p_{r_*}^4}{p_\varphi^3 u^3 (7 + 2p_\varphi^2 u)^3} \hat{t}_{p_{r_*}^4}^{33} \right], \quad (52) \end{aligned}$$

where

$$\begin{aligned} \hat{t}_{p_{r_*}}^{21} = 1 + \frac{6035y}{3029} - \frac{10870y^2}{3029} + \frac{8350y^3}{3029} - \frac{3215y^4}{3029} \\ + \frac{511y^5}{3029}, \quad (53) \end{aligned}$$

$$\hat{t}_{p_{r_*}^2}^{21} = 1 - \frac{1388y}{635} + \frac{666y^2}{635} - \frac{92y^3}{635} - \frac{13y^4}{635}, \quad (54)$$

$$\hat{t}_{p_{r_*}^3}^{21} = 1 - \frac{981y}{619} + \frac{573y^2}{619} - \frac{115y^3}{619}, \quad (55)$$

$$\hat{t}_{p_{r_*}^4}^{21} = 1 - \frac{82y}{183} - \frac{17y^2}{183}, \quad (56)$$

$$\begin{aligned} \hat{t}_{p_{r_*}}^{33} = 1 + \frac{67183y}{23815} + \frac{721737y^2}{47630} - \frac{85973y^3}{9526} \\ + \frac{30812y^4}{4763} - \frac{10722y^5}{4763} + \frac{16769y^6}{47630} \\ - \frac{337y^7}{47630}, \quad (57) \end{aligned}$$

$$\begin{aligned} \hat{t}_{p_{r_*}^2}^{33} = 1 + \frac{3125521y}{762080} + \frac{5675333y^2}{762080} - \frac{2623521y^3}{69280} \\ + \frac{3513777y^4}{95260} - \frac{2943211y^5}{152416} + \frac{7128059y^6}{762080} \\ - \frac{2725303y^7}{762080} + \frac{35247y^8}{95260} + \frac{5233y^9}{95260}, \quad (58) \end{aligned}$$

$$\begin{aligned} \hat{t}_{p_{r_*}^3}^{33} = 1 + \frac{1407963y}{381040} - \frac{343943y^2}{47630} + \frac{2036583y^3}{95260} \\ - \frac{271775y^4}{19052} + \frac{602219y^5}{76208} - \frac{268357y^6}{95260} \\ + \frac{85037y^7}{190520} + \frac{918y^8}{23815}, \quad (59) \end{aligned}$$

$$\begin{aligned} \hat{t}_{p_{r_*}^4}^{33} = 1 + \frac{858779y}{190520} + \frac{92901791y^2}{6096640} + \frac{66769y^3}{7040} \\ - \frac{94475723y^4}{1219328} + \frac{9400891y^5}{152416} - \frac{82481269y^6}{3048320} \\ + \frac{17880961y^7}{1524160} - \frac{6096411y^8}{1524160} + \frac{2935y^9}{13856} \\ + \frac{4009y^{10}}{76208}. \quad (60) \end{aligned}$$

Each residual function is resummed using Padé approximants. The choices we made are summarized in Table II. The modes (3, 2) and (4, 4) are shown in Fig-

TABLE II. Padé used for the resummation of the tail 2PN noncircular corrections for the modes (2, 2), (2, 1) and (3, 3). Note that $\hat{t}_{p_{r_*}^3}^{33}$ has terms up to y^8 , but we use the (3, 2) Padé.

(ℓ, m)	Padé			
	$\hat{t}_{p_{r_*}}^{\ell m}$	$\hat{t}_{p_{r_*}^2}^{\ell m}$	$\hat{t}_{p_{r_*}^3}^{\ell m}$	$\hat{t}_{p_{r_*}^4}^{\ell m}$
(2, 2)	(4, 3)	(4, 3)	(4, 4)	(4, 4)
(2, 1)	(2, 3)	(1, 3)	(0, 3)	(2, 0)
(3, 3)	(4, 3)	(5, 4)	(3, 2)	(5, 5)

ure 8 which compares analytical with numerical waveform for an illustrative, but significant, set of configurations. We start by noticing that the merger-ringdown waveform, especially for the mode (2, 1), is more accurate for high eccentricity than for small eccentricity. This is related to the (yet unpublished) NQC/ringdown fit that we are using here and that will be presented in a future work. The behavior during merger/ringdown of this test-mass EOB model should be considered preliminary and will undergo further improvements. When analyzing the inspiral phase, a few comments are in order. First, the phase and amplitude agreement during the inspiral phase for the modes (2, 1) and (3, 3) is comparable to the (2, 2) mode, and the 2PN corrections are found to yield a notable reduction of the analytical/numerical phase difference with respect to the simple Newtonian prefactor. This is true for any value of the eccentricity considered. When moving to the modes (3, 2) and (4, 4) one faces instead the rather surprising fact that the PN-corrected waveform performs *worse* than the leading-order one. We understand this result as due to the fact that these modes do not have a tail factor at 2PN order, in contrast to what happens for the modes (2, 2), (3, 3) and (2, 1) where the aforementioned compensation between instantaneous and tail part can take place. An illustration of this effect for initial eccentricity $e_0 = 0.7$ can be found in Fig. 9. Qualitatively, with greater accuracy the same behavior should be found also for the modes (3, 2) and (4, 4). Future work, that aims at incorporating all noncircular corrections up to 3PN in our factorized and resummed waveform, will hopefully clarify these issues [51].

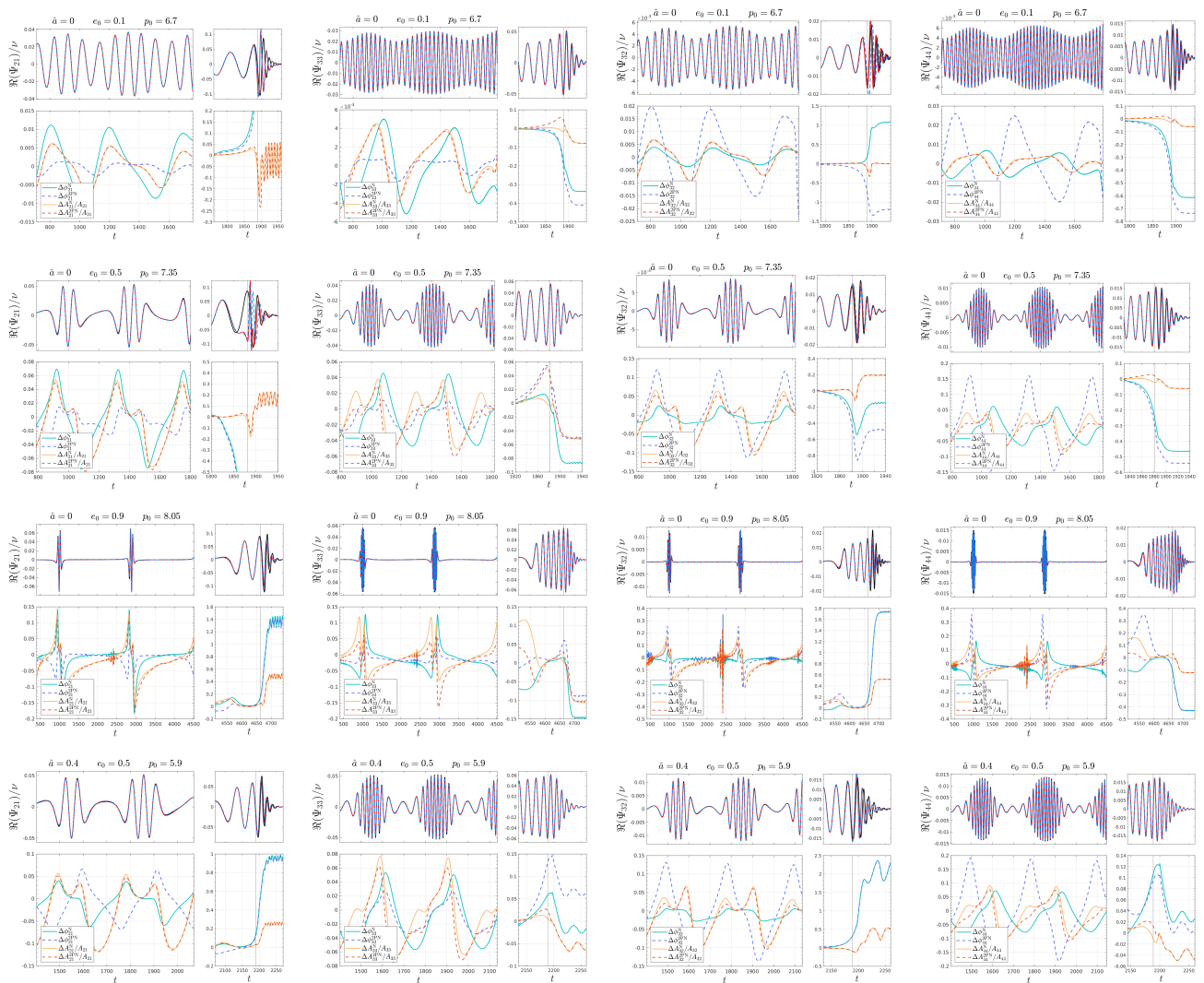


FIG. 8. Same color scheme of Fig. 4, but here in each row we consider the subdominant modes (2,1), (3,3), (3,2), and (4,4) for the configurations $(e_0, \hat{a}, p_0) = (0.1, 0, 6.7), (0.5, 0, 7.35), (0.9, 0, 8.05), (0.5, 0.4, 5.9)$.

1. Multipole $\ell = 2, m = 0$

In Sec. IIC we have already pointed out that we have to use an alternative factorization for the modes with $m = 0$. In Fig. 10 we test the factorization proposed in Eq. (24) for different geodesic configurations in Schwarzschild. As it can be seen, the agreement between numerical and analytical results is still qualitatively good, even if the other analytical modes discussed above are clearly more accurate (both with only Newtonian and 2PN noncircular corrections). Here a source of disagreement is that the asymmetry of the $m = 0$ numerical modes with respect to the apastron is not negligible, even in the geodesic case. In any case, for the $m = 0$ modes the 2PN corrections do not seem to improve the analytical waveform with only the generic Newtonian prefactor.

TABLE III. Hyperbolic capture configurations in the large mass ratio limit considered in this work. The symmetric mass ratio used to drive the dynamics is $\nu = 10^{-2}$. For each configuration we report the Kerr dimensionless spin parameter \hat{a} , the initial energy E_0 , the initial angular momentum $p_{\varphi,0}$, the initial separation r_0 , the number of peaks of the orbital frequency $N_{\Omega}^{\text{peaks}}$, and the merger time t_{mrg} .

\hat{a}	E_0	$p_{\varphi,0}$	r_0	$N_{\Omega}^{\text{peaks}}$	t_{mrg}
0	1.000711	4.01	120	2	2133
0	1.000712	4.01	120	1	819
0	1.001240	4.01	120	1	731

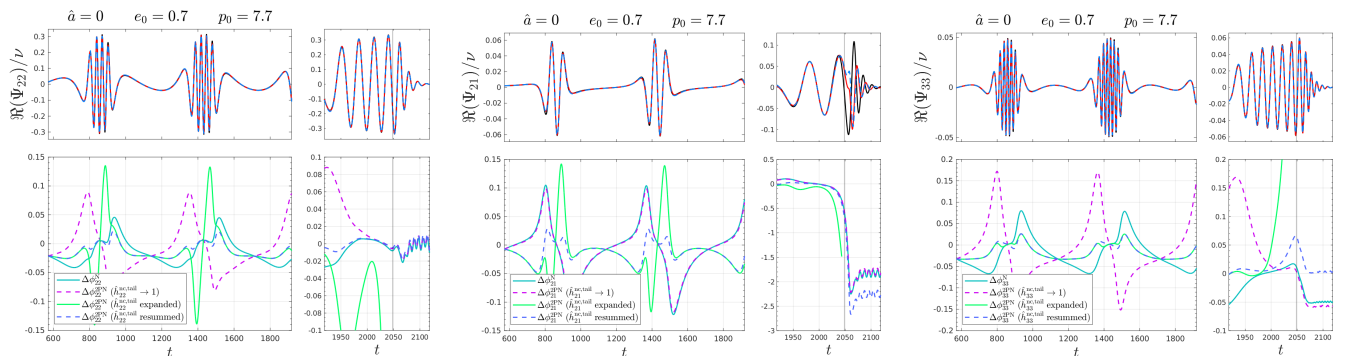


FIG. 9. Comparisons of the waveform modes (2,2), (2,1) and (3,3) for the nonspinning case $(e_0, p_0) = (0.7, 7.7)$. Top panels: numerical waveforms (black), the waveforms with only Newtonian noncircular corrections (red online) and the waveforms with 2PN noncircular corrections with the resummed eccentric tail factor (dashed blue). Bottom panels: analytical/numerical phase differences (in radians) for different prescriptions: (i) only Newtonian noncircular corrections (solid light blue) (ii) only instantaneous noncircular corrections up to 2PN, i.e. without eccentric tail (dashed purple) (iii) waveform with 2PN noncircular corrections, both instantaneous and hereditary in expanded form (solid aqua-green) (iv) waveform with 2PN noncircular corrections, both instantaneous and hereditary, with resummation applied to the latter (dashed blue).

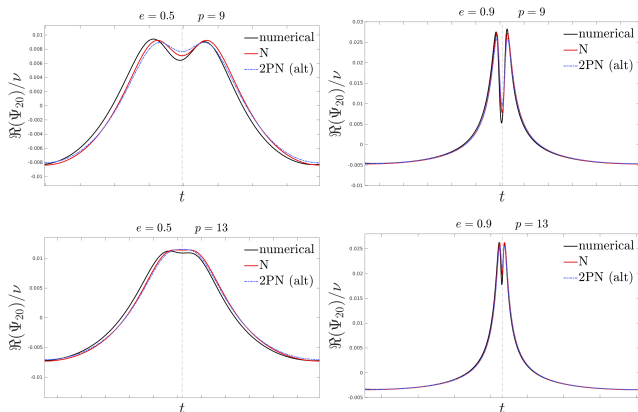


FIG. 10. Comparisons for the mode (2,0) on nonspinning geodesic orbits with $e = (0.5, 0.9)$ and $p = (9, 13)$. We show the numerical waveform (black), the EOB waveform with noncircular corrections only at Newtonian level (red online) and with corrections at 2PN as discussed in Sec. II C (dashed blue).

IV. WAVEFORM VALIDATION: DYNAMICAL CAPTURE IN THE LARGE MASS RATIO LIMIT

We now turn our attention to dynamical captures in the large mass ratio limit. In particular, we consider the configurations that were originally shown in Fig. 14 of Ref. [19], whose parameters are also listed in Table III for convenience. The analytical/numerical comparisons for the new prescriptions, compared with the original Newtonian case, are shown in Figure 11. We report both the waveforms with expanded and resummed instantaneous noncircular phase at 2PN. We also recall that in the hyperbolic case the parameters of the ringdown model, the NQC corrections and the merger time are extracted directly from the numerical waveform. This is due to the

fact that a fit over the parameter space of these quantities is not currently available. See Sec. V C of Ref. [19] for more details. For this reason, the last part of the waveform is artificially more accurate than the result that would be obtained with the same fitting-procedure followed for eccentric orbits. Nonetheless, this aspect is not very relevant for our discussion since in order to test the reliability of the 2PN corrections we have to focus on the inspiral. The phase differences of Figure 11 show that the 2PN noncircular corrections do not provide a better analytical/numerical agreement than the Newtonian wave in the hyperbolic scenario. Moreover, the resummation of the instantaneous noncircular phase worsens the analytical/numerical agreement with respect to leaving the instantaneous phase terms in expanded form. This is an indication that the resummation of the instantaneous phase could be avoided. It is possible that employing terms beyond the 2PN order will clarify the procedure to follow for the instantaneous contribution.

V. WAVEFORM VALIDATION: THE COMPARABLE MASS CASE

Let us move now to comparable-mass binaries. In this case, we incorporate our 2PN-improved eccentric waveform within the EOB eccentric model recently presented in Ref. [25], that is currently the latest evolution of the scheme proposed in Ref. [17]. In doing so, we keep the same dynamics, informed by NR quasi-circular simulations, of Ref. [25]. The 2PN noncircular corrections to the waveform have an essentially negligible impact on quasi-circular configurations and it is not worth to provide a new, optimized, determination of (a_6^c, c_3) using the 2PN resummed waveform. We thus explore here the performance of this new waveform using both time-domain (phase-alignment) and frequency domain (un-

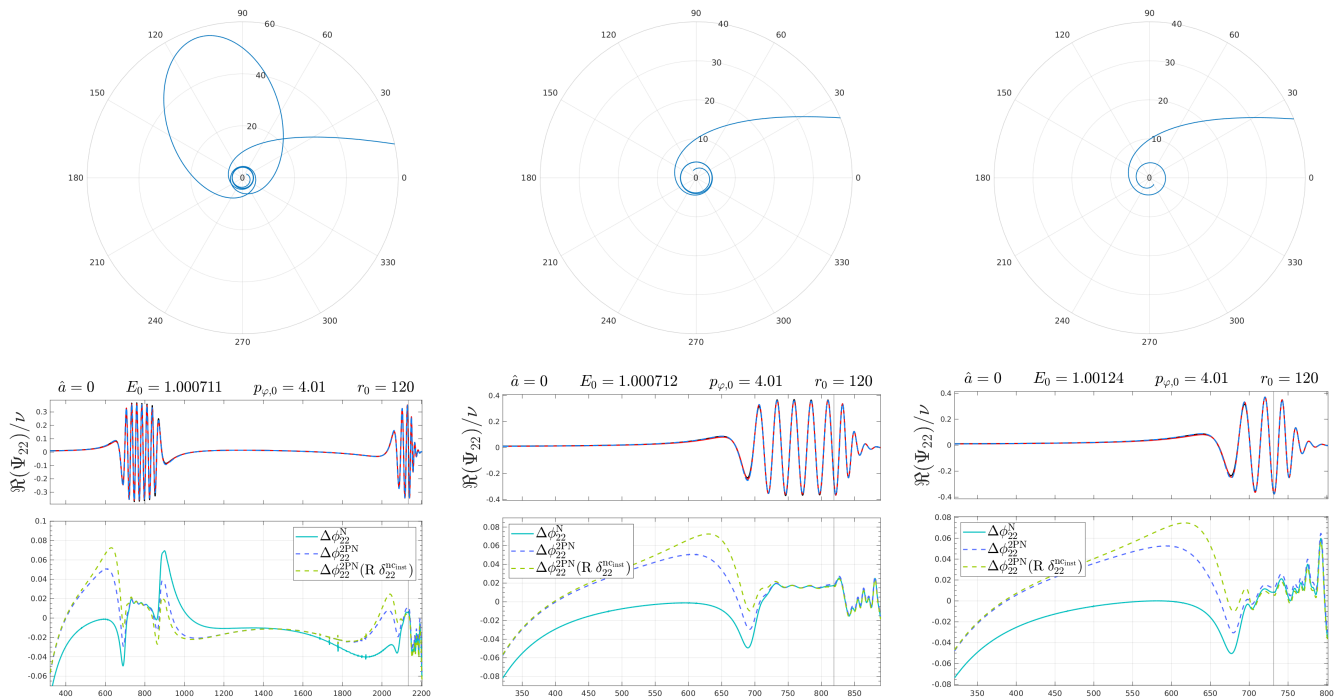


FIG. 11. Dynamical capture of a particle on a Schwarzschild black hole with $\nu = 10^{-2}$, $p_{\varphi,0} = 4.01$ and three different initial energies $E_0 = (1.000711, 1.000712, 1.00124)$. Top panels: the trajectories, all starting from $r_0 = 120$, although the plot only focuses on the latest part. Middle panels: comparing the real part of the numerical waveform (black, barely indistinguishable) with two analytical waveforms: the one with only the Newtonian noncircular corrections (red) and the one with the 2PN corrections where the tail factor is resummed while the instantaneous factor is not (dashed blue). The corresponding phase differences are reported in the bottom panels (solid clear blue and dashed blue, respectively). The same panels also show the analytical/numerical phase difference obtained with the resummation applied to *both* the tail and the instantaneous 2PN noncircular phase $\delta_{22}^{\text{inst}}$ (dashed green). The parameters of the ringdown and of the NQC corrections, as well the merger time (marked by the vertical line), are extracted from numerical data as in Ref. [19], see text. The closest analytical/numerical agreement is obtained resumming only the noncircular tail factor.

faithfulness) comparisons.

A. Phase comparison in the time domain

Let us consider first the time-domain phasing comparison with the 28 public eccentric datasets of the SXS catalog [15]. We have 20 nonspinning datasets, with initial nominal eccentricities up to 0.3, and 8 spin-aligned datasets. In Ref. [24] we had performed specific analyses of this data in order to complement the information available in previous work [15], in particular: (i) computing a gauge-invariant estimate of the eccentricity during the evolution and (ii) giving two different estimates on the NR uncertainty from the two highest resolutions available. For completeness, the datasets we consider are listed in Table IV. The Table reports the time-domain phase uncertainty at merger point $\delta\phi_{\text{mrg}}^{\text{NR}}$ as well as the analogous quantities for the unfaithfulness $\bar{F}_{\text{NR/NR}}^{\text{max}}$ on Advanced LIGO noise, as detailed in Ref. [24] according to the definitions that we will recall below. Table IV also reports, for each configuration, the parameters $(e_{\omega_a}^{\text{EOB}}, \omega_a^{\text{EOB}})$ used to initialize each EOB

evolution at apastron (see Refs. [17, 24]). These values are updated with respect to previous work because they are determined by inspecting the EOB/NR phase difference in the time-domain and are tuned manually so to reduce as much as possible the difference between the EOB and NR instantaneous GW frequencies [24]. Let us note that our procedure for setting up initial data can be optimized. On the one hand, the manual procedure for determining $(e_{\omega_a}^{\text{EOB}}, \omega_a^{\text{EOB}})$ could have been automatized. On the other hand, the initial conditions we use are the analogous of the adiabatic initial conditions for circular orbits. As such, they do not reduce to the (iterated) post-adiabatic ones [52, 53] in the quasi-circular limit, and some spurious eccentricity would be present in that case. These improvements are discussed in Ref. [32] and will be taken into consideration in the future. It is understood that they can only improve the EOB/NR agreement, as pointed out in Ref. [32] for the version of the eccentric **TEOBResumS** of Ref. [24]. To convey all available information, we find it useful to explicitly show the time-domain phasing comparisons in Figure 12 (for the nonspinning datasets) and in Figure 13 (for the spinning dataset). One appreciates that for several cases the careful choice of $(e_{\omega_a}^{\text{EOB}}, \omega_a^{\text{EOB}})$ allows one to obtain a rather

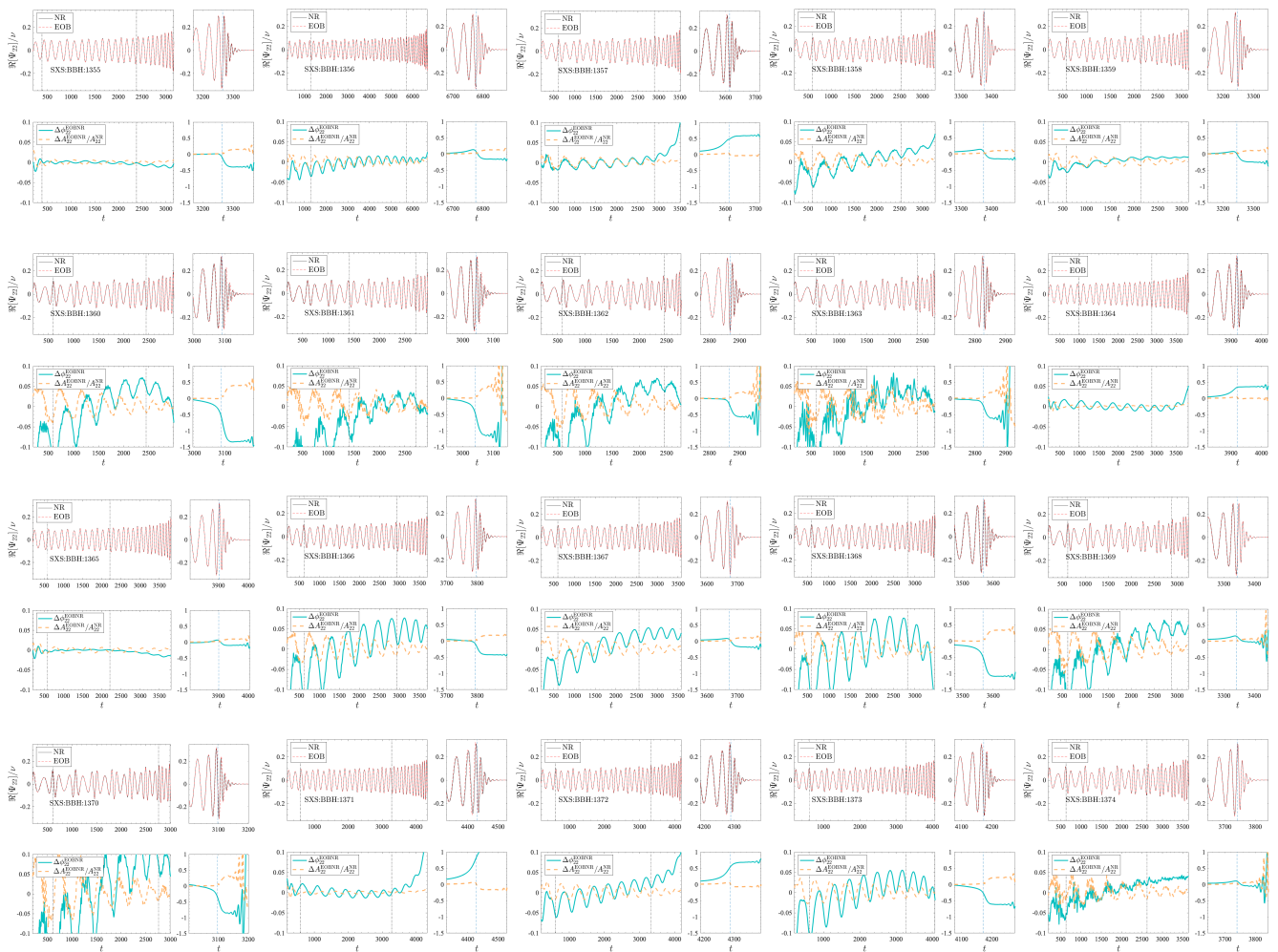


FIG. 12. EOB/NR time-domain phasing for all the nonspinning datasets considered. The dashed vertical lines indicate the alignment window. For each configuration, we show together the NR (black) and EOB (red) real part of the waveform (top panel), and the phase difference (blue online) and the relative amplitude difference (orange online), bottom panel.

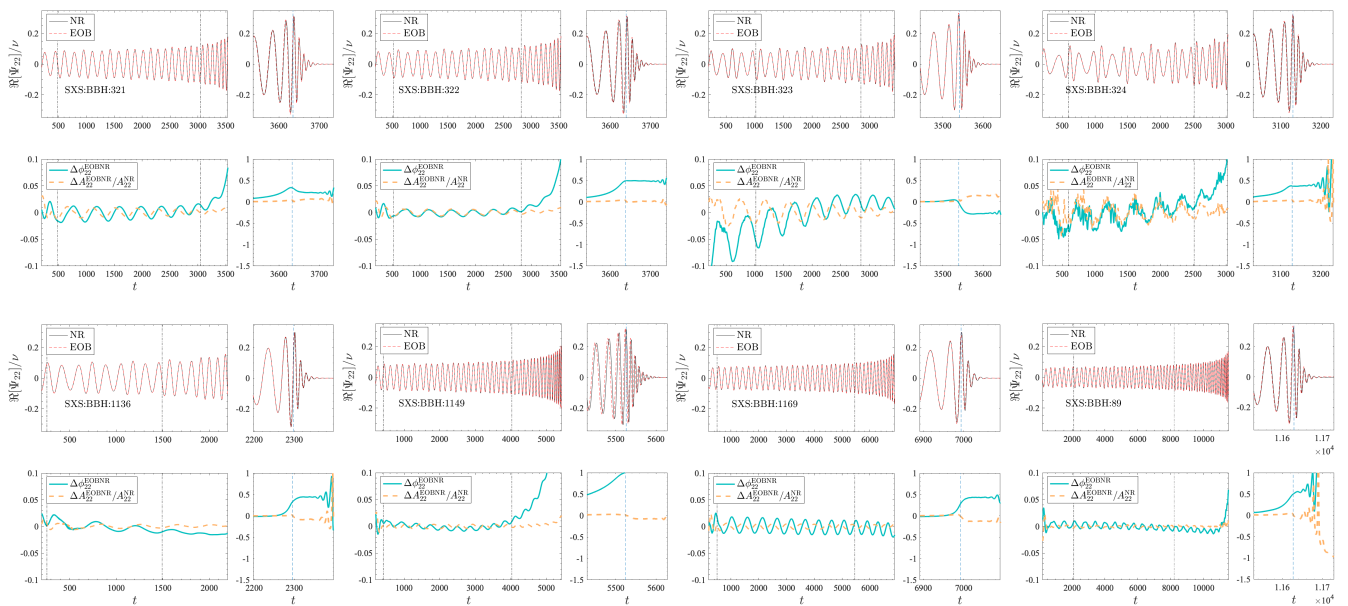


FIG. 13. EOB/NR time-domain phasing for all spinning datasets considered. The dashed vertical lines indicate the alignment window. For each configuration, we show together the NR (black) and EOB (red) real part of the waveform (top panel), and the phase difference (blue online) and the relative amplitude difference (orange online), bottom panel.

TABLE IV. SXS simulations with eccentricity analyzed in this work. From left to right: the ID of the simulation; the mass ratio $q \equiv m_1/m_2 \geq 1$ and the individual dimensionless spins (χ_1, χ_2) ; the time-domain NR phasing uncertainty at merger $\delta\phi_{\text{mrg}}^{\text{NR}}$; the estimated NR eccentricity at first apastron $e_{\omega_a}^{\text{NR}}$; the NR frequency of first apastron ω_a^{NR} ; the initial EOB eccentricity $e_{\omega_a}^{\text{EOB}}$ and apastron frequency ω_a^{EOB} used to start the EOB evolution; the maximal NR unfaithfulness uncertainty, $\bar{F}_{\text{NR/NR}}^{\text{max}}$, the initial frequency used in the EOB/NR unfaithfulness computation, Mf_{min} , and the maximal EOB/NR unfaithfulness, $\bar{F}_{\text{EOB/NR}}^{\text{max}}$.

#	id	(q, χ_1, χ_2)	$\delta\phi_{\text{mrg}}^{\text{NR}}$ [rad]	$e_{\omega_a}^{\text{NR}}$	ω_a^{NR}	$e_{\omega_a}^{\text{EOB}}$	ω_a^{EOB}	$\bar{F}_{\text{NR/NR}}^{\text{max}}$ [%]	Mf_{min}	$\bar{F}_{\text{EOB/NR}}^{\text{max}}$ [%]
1	SXS:BBH:1355	(1, 0, 0)	+0.92	0.0620	0.03278728	0.0888	0.02805750	0.012	0.0055	0.13
2	SXS:BBH:1356	(1, 0, 0)	+0.95	0.1000	0.02482006	0.15038	0.019077	0.0077	0.0044	0.24
3	SXS:BBH:1358	(1, 0, 0)	+0.25	0.1023	0.03108936	0.18082	0.021238	0.016	0.0061	0.22
4	SXS:BBH:1359	(1, 0, 0)	+0.25	0.1125	0.03708305	0.18240	0.021387	0.0024	0.0065	0.17
5	SXS:BBH:1357	(1, 0, 0)	-0.44	0.1096	0.03990101	0.19201	0.01960	0.028	0.0061	0.15
6	SXS:BBH:1361	(1, 0, 0)	+0.39	0.1634	0.03269520	0.23557	0.020991	0.057	0.0065	0.35
7	SXS:BBH:1360	(1, 0, 0)	-0.22	0.1604	0.03138220	0.2440	0.019508	0.0094	0.0065	0.31
8	SXS:BBH:1362	(1, 0, 0)	-0.09	0.1999	0.05624375	0.3019	0.01914	0.0098	0.0065	0.15
9	SXS:BBH:1363	(1, 0, 0)	+0.58	0.2048	0.05778104	0.30479	0.01908	0.07	0.006	0.25
10	SXS:BBH:1364	(2, 0, 0)	-0.91	0.0518	0.03265995	0.0844	0.025231	0.049	0.062	0.15
11	SXS:BBH:1365	(2, 0, 0)	-0.90	0.0650	0.03305974	0.110	0.023987	0.027	0.062	0.12
12	SXS:BBH:1366	(2, 0, 0)	-6×10^{-4}	0.1109	0.03089493	0.14989	0.02577	0.017	0.0052	0.20
13	SXS:BBH:1367	(2, 0, 0)	+0.60	0.1102	0.02975257	0.15095	0.0260	0.0076	0.0055	0.15
14	SXS:BBH:1368	(2, 0, 0)	-0.71	0.1043	0.02930360	0.14951	0.02512	0.026	0.0065	0.13
15	SXS:BBH:1369	(2, 0, 0)	-0.06	0.2053	0.04263738	0.3134	0.0173386	0.011	0.0041	0.25
16	SXS:BBH:1370	(2, 0, 0)	+0.12	0.1854	0.02422231	0.31708	0.016779	0.07	0.006	0.37
17	SXS:BBH:1371	(3, 0, 0)	+0.92	0.0628	0.03263026	0.0912	0.029058	0.12	0.006	0.19
18	SXS:BBH:1372	(3, 0, 0)	+0.01	0.1035	0.03273944	0.14915	0.026070	0.06	0.006	0.09
19	SXS:BBH:1373	(3, 0, 0)	-0.41	0.1028	0.03666911	0.15035	0.02529	0.0034	0.0061	0.13
20	SXS:BBH:1374	(3, 0, 0)	+0.98	0.1956	0.02702594	0.314	0.016938	0.067	0.0059	0.1
21	SXS:BBH:89	(1, -0.50, 0)	...	0.0469	0.02516870	0.07194	0.01779	...	0.0025	0.18
22	SXS:BBH:1136	(1, -0.75, -0.75)	-1.90	0.0777	0.04288969	0.1209	0.02728	0.074	0.0058	0.12
23	SXS:BBH:321	(1.22, +0.33, -0.44)	+1.47	0.0527	0.03239001	0.07621	0.02694	0.015	0.0045	0.27
24	SXS:BBH:322	(1.22, +0.33, -0.44)	-2.02	0.0658	0.03396319	0.0984	0.026895	0.016	0.0061	0.26
25	SXS:BBH:323	(1.22, +0.33, -0.44)	-1.41	0.1033	0.03498377	0.1438	0.02584	0.019	0.0058	0.17
26	SXS:BBH:324	(1.22, +0.33, -0.44)	-0.04	0.2018	0.02464165	0.29425	0.01894	0.098	0.0058	0.19
27	SXS:BBH:1149	(3, +0.70, +0.60)	+3.00	0.0371	0.03535964	0.06237	0.02664	0.025	0.005	1.07
28	SXS:BBH:1169	(3, -0.70, -0.60)	+3.01	0.0364	0.02759632	0.04895	0.024285	0.033	0.004	0.10

flat EOB/NR phase difference, with residual oscillations of the order of 0.01 rad, with accumulated phase difference at merger compatible with the nominal NR uncertainty listed in Table IV. However, for some datasets, notably those with larger initial eccentricities, the choice of the initial parameters looks suboptimal, and the phase difference still shows a linear drift. Typically, this effect is more prominent for dataset with larger initial eccentricity. It might be related to either missing physics in the dynamics¹⁴ or to the need of further improving the initial data choice. Note however that this happens for NR simulations that are especially noisy in the frequency at early times, so this might prevent us from an optimal determination of the initial data that is based on the time-alignment procedure, which is in turn affected by the noise in the frequency. In any case, our choice of

$(e_{\omega_a}^{\text{EOB}}, \omega_a^{\text{EOB}})$ can be considered *conservative* for all the datasets considered and actually suggests that the analytical model can match the NR waveforms even better than what shown in Figs. 12 and 13. The understanding that this is probably the case is motivated by the observation that there are datasets with high eccentricity, e.g. SXS:BBH:1362 or SXS:BBH:1363, whose EOB/NR phase agreement is practically equivalent to that of less eccentric dataset (e.g. SXS:BBH:1358).

B. EOB/NR unfaithfulness

As done in previous works, as an additional figure of merit we evaluate the quality of the EOB waveform by computing the EOB/NR unfaithfulness weighted by the Advanced LIGO noise over all the available configurations. Here we updated the analogous calculation done in Ref. [25] that was only relying on the simple Newton-factorized waveform without the 2PN-accurate eccentric corrections. Considering two waveforms (h_1, h_2) , let us

¹⁴ We remind the reader that the radiation reaction we are using here only incorporates the noncircular Newtonian prefactor in the $\ell = m = 2$ mode.

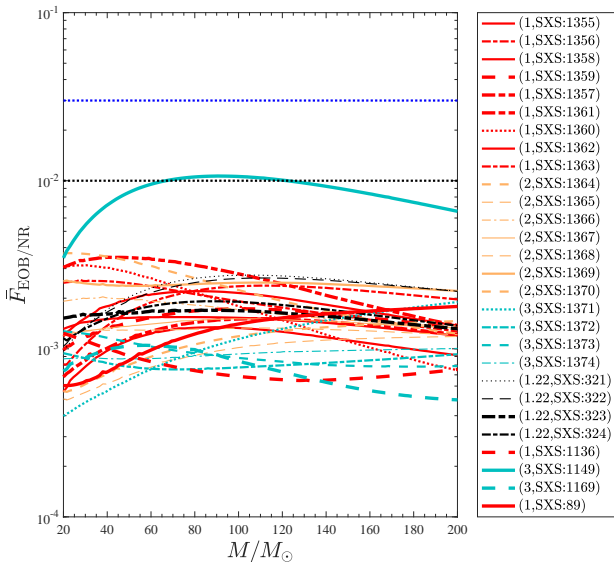


FIG. 14. EOB/NR unfaithfulness for the $\ell = m = 2$ mode computed over the eccentric SXS simulations publicly available, Table IV. The horizontal lines mark the 0.03 and 0.01 values. The value of $\bar{F}_{\text{EOB/NR}}^{\text{max}}$ does not exceed the 0.7% except for the single outlier given by SXS:BBH:1149, corresponding to $(3, +0.70, +0.60)$ with $e_{\omega_a}^{\text{NR}} = 0.037$, that is around 1%. This is consistent with the slight degradation of the model performance for large positive spins already found in the quasi-circular limit, as pointed out in Ref. [25].

recall that the unfaithfulness is a function of the total mass M of the binary and is defined as

$$\bar{F}(M) \equiv 1 - F = 1 - \max_{t_0, \phi_0} \frac{\langle h_1, h_2 \rangle}{\|h_1\| \|h_2\|}, \quad (61)$$

where (t_0, ϕ_0) are the initial time and phase. We used $\|h\| \equiv \sqrt{\langle h, h \rangle}$, and the inner product between two waveforms is defined as $\langle h_1, h_2 \rangle \equiv 4\Re \int_{f_{\text{min}}}^{\infty} \tilde{h}_1(f) \tilde{h}_2^*(f) / S_n(f) df$, where $\tilde{h}(f)$ denotes the Fourier transform of $h(t)$, $S_n(f)$ is the zero-detuned, high-power noise spectral density of Advanced LIGO [54] and f_{min} is the initial frequency approximately corresponding to the frequency of the first apastron on each NR simulation, after the initial junk radiation has cleared. In practice, the integral is done up to a maximal frequency f_{end} that corresponds to $|\tilde{h}(f_{\text{end}})| \sim 10^{-2}$. Both EOB and NR waveforms are tapered¹⁵ in the time-domain so as to reduce high-frequency oscillations in the corresponding Fourier transforms. In addition, as originally pointed out in Ref. [15], the accurate calculation of the Fourier transform of eccentric waveforms is a delicate matter and it may affect the calculation of the EOB/NR

unfaithfulness, $\bar{F}_{\text{EOB/NR}}$, if not optimally chosen. These issues have been discussed to some extent in Sec. IV of Ref. [25], see in particular Fig. 15 and 16 therein. Here we only recall that the original waveform is padded with zeros in order to increase the frequency resolution and capture all the details of the Fourier transform. Similarly, we were careful to tune the tapering parameters so that the EOB and NR Fourier transform for each dataset visually agree likewise to the case shown in Fig. 16 of Ref. [25]. The final outcome of the EOB/NR unfaithfulness computation versus M is shown in Fig. 14. The maximum values $\bar{F}_{\text{EOB/NR}}^{\text{max}}$ are also listed in the last column of Table IV, together with the value of the initial frequency Mf_{min} used in the integral. Figure 14, complemented by Table IV, brings a minimal improvement with respect to Fig. 14 of Ref. [25], especially for low masses. Since we are using here a new choice of the parameters $(e_{\omega_a}^{\text{EOB}}, \omega_a^{\text{EOB}})$ (and consequently new tapering parameters) it is not really possible, within the context of equal-mass binaries, to precisely state to which extent the small improvements found depend on these new choices or on the additional PN corrections in the waveforms. Globally, in view of the similarities between Fig. 14 of Ref. [25] and our current Fig. 14, we are prone to conservatively state that the factorized and resummed 2PN noncircular corrections to the waveform are not especially important on this specific corner of the parameter space.

VI. TESTING THE QUASI-CIRCULAR FACTORIZATION OF KHALIL ET AL. [27].

During the development of this work under the paradigm of the factorization of the general Newtonian prefactor, Ref. [27] appeared. Besides providing some of the analytical expressions used here (e.g. the explicit expression of the tail), Ref. [27] also proposed a different waveform factorization where: (i) only the *quasi-circular* Newtonian prefactor is factored out; (ii) all the noncircular effects are interpreted as corrections to the quasi-circular baseline expression and (iii) the instantaneous and hereditary contributions are included in additive form.

Given our numerical waveforms in the test-mass limit, it is interesting to thoroughly test also this analytical waveform proposal. We carefully follow Sec. IIIB of Ref. [27] and we report here all the equations needed to this aim. For $m > 0$, Ref. [27] proposes the following factorized expression

$$h_{\ell m}^{2\text{PN}_{\text{qc}}} = h_{\ell m}^{(N, \epsilon)_c} \hat{S}_{\text{eff}} (T_{\ell m} + T_{\ell m}^{\text{ecc}}) e^{i\delta_{\ell m}} (f_{\ell m} + f_{\ell m}^{\text{ecc}}), \quad (62)$$

where the eccentric terms $f_{\ell m}^{\text{ecc}}$ and $T_{\ell m}^{\text{ecc}}$ are written as functions of (r, p_r, \dot{p}_r) . For the leading-order quasi-circular hereditary term $T_{\ell m}$ we use the standard prescription introduced in Ref. [42], while for $\delta_{\ell m}$, and $f_{\ell m}$ we follow Refs. [19, 43, 44]. We here focus explicitly on the $(2, 2)$ mode only, precisely following the steps of

¹⁵ We use a hyperbolic tangent function with two tunable parameters, (α, τ) , of the form $w(t) = [1 + \tanh(\alpha t - \tau)] / 2$ that multiplies both the NR and EOB waveforms.

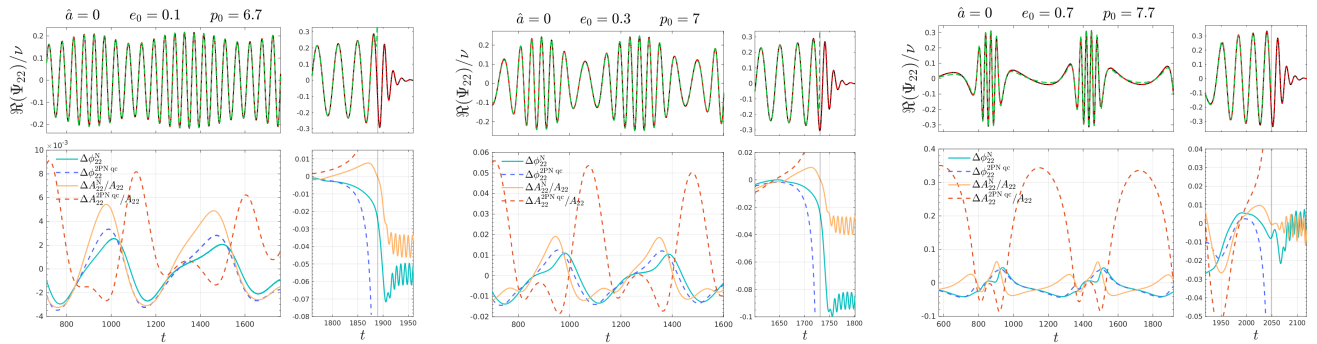


FIG. 15. Testing the waveform factorization of Ref. [27], Eq. (62): comparisons between the $\ell = m = 2$ numerical and analytical waveforms emitted by the eccentric inspiral of a test particle on a Schwarzschild black hole. The initial eccentricities and semilata recta are $(e_0, p_0) = (0.1, 6.7)$, $(0.3, 7)$, $(0.7, 7.7)$. Each top panel displays the numerical waveform (black, indistinguishable); the EOB waveform with the generic Newtonian prefactor (dash-dotted red, labeled N) and the 2PN accurate waveform with the quasi-circular factorization of Eq. (62) (labeled 2PN_{qc}). The corresponding phase differences and relative amplitude differences are shown in the bottom panels. The vertical black line marks the merger-time, corresponding to the peak of the numerical waveform amplitude. For simplicity, the 2PN_{qc} waveform has not been completed by NQC corrections and ringdown. The analytical/numerical phase agreement is comparable for the two choices (blue lines); by contrast, the amplitude disagreement is always larger for the 2PN_{qc} prescription, and worsens up to 30% when the eccentricity increases.

Ref. [27]. More precisely, we use the full expression of T_{22}^{ecc} presented in the supplemental material of Ref. [27], that reads

$$\begin{aligned}
T_{22}^{\text{ecc}} = & \eta^3 \pi \left[-\frac{3ip_r}{2r} - \dot{p}_r \sqrt{r} - \frac{p_r (2p_r + i\dot{p}_r r^{3/2})}{4\sqrt{r}} + \frac{1}{48} \left(-5ip_r^3 - 15pr^2 \dot{p}_r r^{3/2} + 9ip_r \dot{p}_r^2 r^3 - \dot{p}_r^3 r^{9/2} \right) \right. \\
& + \frac{1}{32} \sqrt{r} \left(-10p_r^4 + 15ip_r^3 \dot{p}_r r^{3/2} + 8p_r^2 \dot{p}_r^2 r^3 - ip_r \dot{p}_r^3 r^{9/2} + 2\dot{p}_r^4 r^6 \right) + \frac{r}{1920} \left(589ip_r^5 + 1150p_r^4 \dot{p}_r r^{3/2} \right. \\
& - 1060ip_r^3 \dot{p}_r^2 r^3 - 505p_r^2 \dot{p}_r^3 r^{9/2} + 55ip_r \dot{p}_r^4 r^6 - 116\dot{p}_r^5 r^{15/2} \left. \right) + \frac{r^{3/2}}{11520} \left(1974p_r^6 - 4995ip_r^5 \dot{p}_r r^{3/2} \right. \\
& \left. - 7470p_r^4 \dot{p}_r^2 r^3 + 7240ip_r^3 \dot{p}_r^3 r^{9/2} + 3855p_r^2 \dot{p}_r^4 r^6 - 669ip_r \dot{p}_r^5 r^{15/2} + 560\dot{p}_r^6 r^9 \right) \left. \right]. \quad (63)
\end{aligned}$$

For the instantaneous contribution, f_{22}^{ecc} , we use Eq. (122)

of Ref. [27] that we rewrite here explicitly specified to the test-mass limit ($\nu = 0$),

$$\begin{aligned}
f_{22}^{\text{ecc}} = & -\frac{p_r^2}{2v_0^2} + ip_r r v_0 + \frac{r^2 v_0^4}{2} + \frac{1}{2rv_0^2} - 1 + \eta^2 \left(\frac{p_r^4}{4r^3 v_0^8} + \frac{29p_r^4}{84v_0^2} + \frac{ip_r^3}{4r^2 v_0^5} - \frac{37}{84} ip_r^3 r v_0 - \frac{p_r^2}{12r^4 v_0^8} + \frac{1}{4} p_r^2 r^2 v_0^4 + \frac{31p_r^2}{14rv_0^2} \right. \\
& \left. - \frac{37}{84} ip_r r^3 v_0^7 + \frac{ip_r}{6r^3 v_0^5} - \frac{209ip_r v_0}{84} - \frac{1}{6r^5 v_0^8} - \frac{2}{21} r^4 v_0^{10} - \frac{13}{12r^2 v_0^2} - \frac{59rv_0^4}{84} + \frac{43v_0^2}{21} \right) + \eta^3 \left(-\frac{\hat{a}p_r^2}{3r^3 v_0^5} - \frac{4i\hat{a}p_r}{3r^2 v_0^2} \right. \\
& \left. + \frac{\hat{a}}{3r^4 v_0^5} - \frac{5\hat{a}v_0}{3r} + \frac{4\hat{a}v_0^3}{3} \right) + \eta^4 \left(-\frac{\hat{a}^2 p_r^4}{6r^4 v_0^8} - \frac{i\hat{a}^2 p_r^3}{6r^3 v_0^5} + \frac{\hat{a}^2 p_r^2}{6r^5 v_0^8} - \frac{5\hat{a}^2 p_r^2}{6r^2 v_0^2} + \frac{i\hat{a}^2 p_r v_0}{r} + \frac{\hat{a}^2}{2r^3 v_0^2} - \frac{\hat{a}^2 v_0^4}{2} - \frac{p_r^6}{4r^6 v_0^{14}} \right. \\
& - \frac{31p_r^6}{112r^3 v_0^8} - \frac{277p_r^6}{1008v_0^2} - \frac{5ip_r^5}{32r^5 v_0^{11}} - \frac{3ip_r^5}{14r^2 v_0^5} + \frac{571ip_r^5 r v_0}{2016} - \frac{p_r^4}{12r^7 v_0^{14}} - \frac{179p_r^4}{144r^4 v_0^8} - \frac{85}{252} p_r^4 r^2 v_0^4 - \frac{1963p_r^4}{1008rv_0^2} \\
& \left. - \frac{5ip_r^3}{24r^6 v_0^{11}} + \frac{349ip_r^3 r^3 v_0^7}{1008} - \frac{953ip_r^3}{1008r^3 v_0^5} + \frac{803}{504} ip_r^3 v_0 + \frac{2p_r^2}{9r^8 v_0^{14}} + \frac{79p_r^2}{168r^5 v_0^8} - \frac{71p_r^2 r^4 v_0^{10}}{1008} + \frac{43p_r^2}{42r^3 v_0^4} - \frac{31p_r^2}{168r^2 v_0^2} \right)
\end{aligned}$$

$$\begin{aligned}
& -\frac{31}{112}p_r^2 r v_0^4 - \frac{43p_r^2 v_0^2}{126} - \frac{5ip_r}{72r^7 v_0^{11}} + \frac{127ip_r r^5 v_0^{13}}{2016} - \frac{83ip_r}{504r^4 v_0^5} + \frac{5}{63}ip_r r^2 v_0^7 - \frac{9221ip_r v_0}{6048r} + \frac{1}{9r^9 v_0^{14}} - \frac{1}{126}r^6 v_0^{16} \\
& + \frac{1}{6r^6 v_0^8} + \frac{43}{63r^4 v_0^4} + \frac{53r^3 v_0^{10}}{168} + \frac{13}{504r^3 v_0^2} - \frac{43r^2 v_0^8}{126} - \frac{43v_0^2}{126r} - \frac{11v_0^4}{18} \Big), \tag{64}
\end{aligned}$$

where

$$v_0 = \frac{(1 + \dot{p}_r r^2)^{1/6}}{\sqrt{r}}. \tag{65}$$

Following the practice introduced in Ref. [55], when considering the Hamiltonian formalism for a test particle around a Schwarzschild black hole it is useful to replace p_r with p_{r^*} , the radial momentum conjugate to some Regge-Wheeler tortoise coordinate [56]. The scope of this is to avoid the presence of spurious numerical singularities towards the horizon when the equations of motion are solved numerically. We thus rewrite the above equations replacing (p_r, \dot{p}_r) with (p_{r^*}, \dot{p}_{r^*}) . Using Hamilton's equations, the radial momentum and its derivative are written as (see Appendix E of Ref. [27])

$$p_r = \sqrt{\frac{B}{A}} p_{r^*} \equiv \xi^{-1}(r) p_{r^*}, \tag{66}$$

$$\dot{p}_r = - \left[\left(\frac{\partial H}{\partial r} \right)_{p_{r^*}} + \left(\frac{\partial H}{\partial p_{r^*}} \right)_r \frac{p_{r^*}}{\xi(r)} \frac{d\xi(r)}{dr} \right]. \tag{67}$$

The explicit expressions for the Kerr metric functions A and B can be found in Ref. [57]. Figure 15 shows the triple comparisons between: (i) the numerical waveform (black online, barely distinguishable in the top panels); (ii) the waveform with the generic Newtonian prefactor [17] (red online) and (iii) the 2PN-accurate waveform of above (dashed, green online). This is done for three values of the initial eccentricity $e_0 = (0.1, 0.3, 0.7)$. For each analytical waveform choice, the bottom panels of the figure reports the corresponding phase differences and fractional amplitude differences. For simplicity, the $h_{\ell m}^{2\text{PN}_{\text{qc}}}$ is not completed through merger (via NQC corrections) and ringdown. As can be seen in the figure, the amplitude differences become relevant at large eccentricities during the inspiral at apastron. Moreover, even at small eccentricity the waveform with only Newtonian corrections seems to perform globally better than the outcome of Eq. (62).

Figure 15 also highlights an aspect that is a priori unexpected: the largest amplitude differences occur at *apastron* and not at *periastron*. This might look puzzling because PN expansions are more accurate in weak field than in strong field, while the plot seems to indicate the opposite. The reason of this behavior can be understood inspecting Figs. 16 and 17. They refer to the same configuration ($e_0 = 0.7$) of the rightmost panel of Fig. 15. In Fig. 16 we compare different analytical quadrupolar waveforms and their analytical/numerical relative amplitude differences. In particular: (i) the quasi-circular

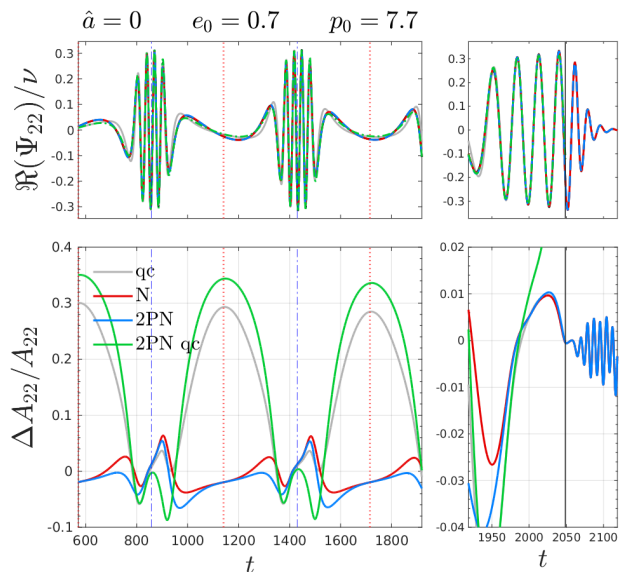


FIG. 16. Comparing waveforms generated by a test-particle inspiralling and plunging into a Schwarzschild black hole with $(e_0, p_0) = (0.7, 7.7)$. Top panel: the numerical waveforms (black, indistinguishable); the quasi-circular EOB waveform (gray); the waveform with the Newtonian noncircular corrections (red); the waveform of Eq. (24) that adds to the previous one the 2PN corrections (blue); and the waveform of Eq. (62) with the quasi-circular factorization and 2PN noncircular corrections (green, without merger and ringdown). Bottom panel: relative amplitude differences with the numerical waveforms. Apastron are marked by dotted (red) vertical lines, while periastron with dash-dotted (blue) lines. See text for discussion.

EOB waveform (gray online); (ii) the waveform with noncircular corrections included in the generic Newtonian prefactor (red online); (iii) the waveform of Eq. (24), where the 2PN noncircular effects are incorporated as a multiplicative correction to the Newtonian prefactor (blue online); and (iv) the waveform with quasi-circular factorization and 2PN noncircular corrections as written in Eq. (62) (green online). These plots are completed by Fig. 17, that illustrates the noncircular *instantaneous* corrections to the amplitude and to the phase for each analytical prescription. The instantaneous noncircular correction for the waveform of Eq. (62) is written as the multiplicative factor $1 + f_{22}^{\text{ecc}}/f_{22}$, for formal consistency with the other analytical choices. All noncircular factors provide a relevant correction to the phase, as shown in the middle panel of Fig. 17. The effect of these corrections is evident in the top panel of Fig. 16, where

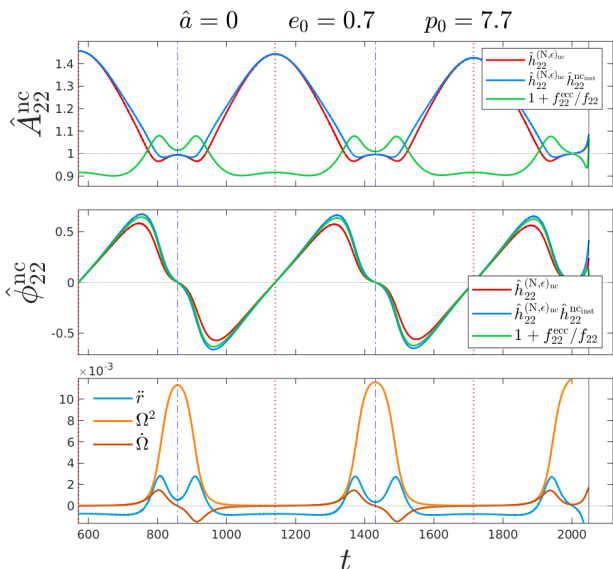


FIG. 17. Contrasting different noncircular corrections for the same configuration of Fig. 16. Top and middle panels: the noncircular contributions to amplitude and phase. We consider the noncircular Newtonian prefactor $\hat{h}_{\ell m}^{(N,\epsilon)nc}$ of Eq. (26) (red), the Newtonian-factorized instantaneous corrections up to 2PN, $\hat{h}_{\ell m}^{(N,\epsilon)nc} \hat{h}_{\ell m}^{ncinst}$, (blue), and the 2PN noncircular corrections of Eq. (62) written as $1 + f_{22}^{ecc}/f_{22}$ (green). The bottom panel shows \dot{r} , Ω^2 and $\dot{\Omega}$. The correction proportional to $\dot{r}/(r\Omega^2)$ in Eq. (26) yields larger values at apastron than $1 + f_{22}^{ecc}/f_{22}$. See text for discussion.

the quasi-circular waveform (gray online) is visibly de-phased with respect to the other curves. This indicates that all noncircular phase corrections discussed in this work eventually yield an improved numerical/analytical phase agreement with respect to the quasi-circular EOB waveform. By contrast, the noncircular correction provided by Eq. (62), at 2PN accuracy, does not provide a reliable amplitude at apastron, with differences that are rather close to those obtained using the standard circular waveform.

To understand this aspect, let us focus for a moment on the Newtonian noncircular prefactor of Eq. (26), whose time-evolution is shown for the case considered in Fig. 17 (red online). The figure shows that the contribution of the Newtonian prefactor is larger at apastron than at periastron. This follows from the fact that in Eq. (26) the orbital frequency Ω appears squared and at the denominator of the noncircular correction, as a consequence of having factorized the circular Newtonian contribution. This eventually amplifies the contribution of the whole function in correspondence of the lowest values of Ω , i.e. at apastron. Note however that the only nonvanishing contribution of Eq. (26) at apastron is the one proportional to \dot{r} , that is thus the main reason behind the behavior seen in Fig. 17. The hierarchy between \dot{r} and Ω^2 is clarified by the bottom panel of Fig. 17. By contrast, when considering Eq. (62), without the crucial factoriza-

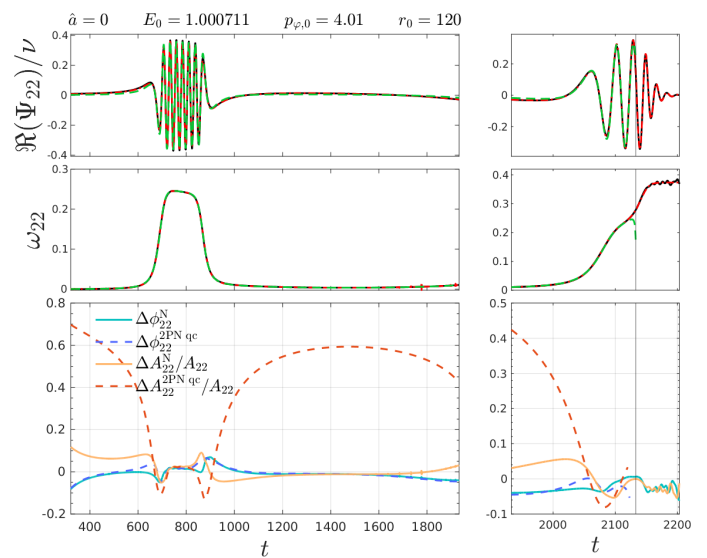


FIG. 18. Same type of comparison of Fig. 15 but considering the dynamical capture configuration in the left panels of Fig. 11. Top panel: real part of the waveform. Middle panel: instantaneous frequency. Bottom panel: phase and fractional amplitude differences. The waveform of Ref. [27], Eq. (62), accumulates rather large amplitude differences up to the apastron of the quasi-elliptic orbit following the first encounter.

tion of the Newtonian prefactor, the amplitude correction remains substantially constant, and small, for the whole radial evolution, see $1 + f_{22}^{ecc}/f_{22}$ in Fig. 17 (green online). This leads to the large analytical/numerical discrepancies for the amplitude, as shown in Fig. 15 and Fig. 16. Loosely speaking, we can trace all this to the fact that Eq. (62) incorporates the PN expansion of Eq. (26) through the replacement of Ω and \dot{r} via the 2PN equation of motion, and so the crucial amplification related to the exact \dot{r}/Ω^2 contribution is lost.

To conclude, we also mention that the problematic behavior of the waveform of Eq. (62) is even more evident in the dynamical capture scenario. Fig. 18 refers to the left-most configuration of Fig. 11. The waveform of Ref. [27], Eq. (62), yields fractional amplitude differences $\sim 60\%$ at the apastron of the quasi-elliptic orbit following the first encounter.

VII. CONCLUSIONS

We have presented a new factorized and resummed multipolar waveform for spin aligned binaries that is valid along noncircular orbits, i.e. either eccentric inspirals or dynamical capture scenarios. Our main findings can be summarized as follows:

- (i) We have exploited 2PN noncircular results within the paradigm of the factorization of the generic Newtonian prefactor. In this way, this 2PN information is simply recasted into correcting factors

that can be directly used to improve the waveform of existing eccentric model based on the formalism of `TEOBResumS`, notably those of Refs. [17, 19, 24, 25]. Differently from other works [27], we choose to express the correcting factors in terms of $p_\varphi^2 u$, without using powers of the derivative of the radial momentum \dot{p}_r . This permits to obtain analytical expressions that are relatively simple, with a well organized analytical structure.

- (ii) We thoroughly tested the performance of these analytical correcting factors by performing comparisons with numerical waveforms from eccentric inspirals (also through plunge and merger) in the test-mass limit. We showed that the analytical/numerical agreement through the plunge phase (and for large eccentricity) can be largely improved by implementing straightforward resummations scheme (via Padé approximants) of the residual polynomials in $p_\varphi^2 u$ entering the noncircular tail factor. With this procedure, we can obtain analytical/numerical phase disagreements of ± 0.04 rad for $e = 0.9$, and disagreements at most within 0.02 rad for smaller eccentricities (see Figs. 4 and 5). A similar behavior is also found for hyperbolic captures.
- (iii) The quadrupolar waveform can be further improved applying the same resummation procedure adopted for the eccentric tail contribution also to the 2PN instantaneous noncircular contribution to the phase. Nonetheless, this step is not as crucial as the resummation of the hereditary contribution.
- (iv) When moving to the comparable-mass case, we applied the same 2PN-resummed noncircular correction to the EOB noncircular model of Ref. [25] and we provided a new comparison with the 28 public NR simulations of eccentric inspirals from the SXS catalog. For most of the configurations, the phase difference during the inspiral is mostly within the ± 0.05 bandwidth. The related EOB/NR unfaithfulness computations (using aLIGO noise for $20M_\odot \leq M \leq 200M_\odot$) are below the 1% threshold (at most 0.6%) except for the only outlier, SXS:BBH:1149 that grazes this limit because of limitations inherited by the underlying quasi-circular model, as explained in Ref. [25]. It should be noted that the new, factored and resummed, 2PN contributions discussed here seem to bring only marginal improvements to the model of Ref. [25]. In this respect, the use of, well controlled, test-mass limit numerical data proves crucial to learn the actual importance of this additional analytical information.
- (v) In this respect, the availability of test-mass waveform data allowed us to thoroughly test the waveform factorization proposed in Ref. [27], whose main difference with our prescription is that the noncircular part of the Newtonian prefactor is not

factored out. We found that the full Newtonian-factor factorization (even before the presence of the 2PN noncircular corrections) looks more accurate and robust (especially for the amplitude, with differences that can reach up to 60% versus a 6% at most) all over the parameter space. The origin of the reliable behavior of the amplitude of the Newton-factorized waveform (somehow overlooked in past works) traces to the crucial presence of the the exact contribution $\ddot{r}/r\Omega^2$ in Eq. (26), as extensively explained in Sec. VI.

In conclusion, our results indicate that the incorporation of high-PN noncircular waveform term within EOB models is more effective if suitable factorizations and resummation procedures are implemented. In particular, the use of the general Newtonian prefactor, as originally proposed in Ref. [17], seems an essential element for constructing highly accurate analytical waveforms for non-circular dynamics for either present or future gravitational wave detectors. We think it is particularly important to emphasize that the good performance of our waveform is not limited to mild values of eccentricities, but it remains robust *also* for large eccentricities. In this respect, the waveform of Ref. [27] implemented in the model of Ref. [32] doesn't seem to be a robust choice when eccentricity is larger than ~ 0.3 . Despite this issue, the model presented in [32] shows an excellent EOB/NR performance over the 28 SXS datasets (with eccentricities up to ~ 0.3) that is globally comparable to ours (and even better in the large-spin case). Although the focus of this paper is on the waveform, we finally note that from our resummed expressions it is possible to compute energy and angular momentum fluxes. These can be used to construct more accurate representations of the analytical radiation reaction (and especially the azimuthal part \mathcal{F}_φ) along general (equatorial) orbits that include the 2PN information, thus going beyond the Newtonian prefactor paradigm¹⁶ of Ref. [17]. This additional analytical information in radiation reaction (as well as the Newton-factor dressing) is currently omitted also in Ref. [32]. Our prescription for radiation reaction has been extensively tested in Ref. [19], that clearly indicated that more analytical information is needed to obtain accurate analytical fluxes for large eccentricities. Exploiting our current results for radiation reaction purposes is postponed to future work. As a last observation, considering

¹⁶ We remind in passing that Ref [17] compared several choices of \mathcal{F}_φ with the exact flux computed in the test-mass limit. Among these choices, there was a circular-factorized and resummed version of the results of [40], Eq. (5) of Ref. [17], analogous to the prescriptions suggested in Ref. [27], modulo the additional Padé resummation adopted in Ref. [17] to enhance the robustness of the analytical expression in strong field. This study [17, 58] indicated that the general-Newtonian prefactor factorization yielded a closer agreement of the fluxes with test-mass numerical data, thus suggesting that another route is necessary to consistently incorporate 2PN results in radiation reaction.

that this result is obtained using only 2PN information, our procedure seems to indicate a viable route to process a large amount of (high-order) PN information [59–61] in order to construct strong-field accurate, EOB-based, fully nonadiabatic, analytical waveform models for eccentric extreme mass ratio inspirals in view of providing waveform templates for LISA [62, 63].

ACKNOWLEDGMENTS

S. B. acknowledges support by the EU H2020 under ERC Starting Grant, no. BinGraSp-714626. M. O. and G. G. acknowledge support from the project “Black holes, neutron stars and gravitational waves” financed by Fondo Ricerca di Base 2018 of the University of Perugia. G. G., M. O. and A. P. thank Niels Bohr Institute for hospitality. S. A. thanks Institute for Pure and Applied Math-

ematics (UCLA) for hospitality. The numerical simulations using *Teukode* [49, 64] were performed on the Virgo “Tullio” server in Torino, supported by INFN. We thank A. Ramos-Buades, A. Buonanno, M. Khalil and S. Ossokine for useful discussions and for sharing within the LVK collaboration the content of Ref. [32] before publication. We are particularly grateful to A. Ramos-Buades for a question that allowed us to improve our understanding of the noncircular corrections to the amplitude.

Appendix A: Newton-factorized noncircular higher modes

In this appendix we present the resulting 2PN noncircular relativistic factors of Sec. II B for all the subdominant modes up to¹⁷ $\ell = m = 4$. Note that the contributions that are not explicitly written, are equal¹⁸ to 1.

a. Tail noncircular factors

$$\begin{aligned} \hat{h}_{20}^{\text{tail-nc}} = & 1 - \frac{\pi p_\varphi}{320c^3 (p_\varphi^2 u - 1)} \left[p_{r_*}^2 u \left(1364 - 2885p_\varphi^2 u + 3490p_\varphi^4 u^2 - 2400p_\varphi^6 u^3 + 890p_\varphi^8 u^4 - 139p_\varphi^{10} u^5 \right) \right. \\ & \left. - \frac{p_{r_*}^4}{3 (p_\varphi^2 u - 1)} \left(4262 - 8790p_\varphi^2 u + 10390p_\varphi^4 u^2 - 7155p_\varphi^6 u^3 + 2670p_\varphi^8 u^4 - 417p_\varphi^{10} u^5 \right) \right]. \end{aligned} \quad (\text{A1})$$

$$\begin{aligned} \hat{h}_{21}^{\text{tail-nc}} = & 1 - \frac{\pi}{11520c^3} \left[6ip_{r_*} u \left(3029 + 6035p_\varphi^2 u - 10870p_\varphi^4 u^2 + 8350p_\varphi^6 u^3 - 3215p_\varphi^8 u^4 + 511p_\varphi^{10} u^5 \right) \right. \\ & - \frac{15p_{r_*}^2}{p_\varphi} \left(635 - 1388p_\varphi^2 u + 666p_\varphi^4 u^2 - 92p_\varphi^6 u^3 - 13p_\varphi^8 u^4 \right) + 20ip_{r_*}^3 \left(619 - 981p_\varphi^2 u + 573p_\varphi^4 u^2 \right. \\ & \left. \left. - 115p_\varphi^6 u^3 \right) + \frac{15p_{r_*}^4}{p_\varphi u} \left(183 - 82p_\varphi^2 u - 17p_\varphi^4 u^2 \right) \right]. \end{aligned} \quad (\text{A2})$$

$$\begin{aligned} \hat{h}_{31}^{\text{tail-nc}} = & 1 - \frac{\pi}{1920c^3 p_\varphi^2 (7 - 6p_\varphi^2 u)^2} \left[ip_{r_*} \left(88130 - 107366p_\varphi^2 u + 89843p_\varphi^4 u^2 - 388835p_\varphi^6 u^3 + 588840p_\varphi^8 u^4 \right. \right. \\ & \left. \left. - 397460p_\varphi^{10} u^5 + 139731p_\varphi^{12} u^6 - 20563p_\varphi^{14} u^7 \right) + \frac{p_{r_*}^2}{2p_\varphi u (7 - 6p_\varphi^2 u)} \left(2115120 - 3821769p_\varphi^2 u \right. \right. \\ & \left. \left. + 915328p_\varphi^4 u^2 - 2431548p_\varphi^6 u^3 + 9399380p_\varphi^8 u^4 - 10528645p_\varphi^{10} u^5 + 5655444p_\varphi^{12} u^6 - 1592318p_\varphi^{14} u^7 \right. \right. \\ & \left. \left. + 186288p_\varphi^{16} u^8 \right) - \frac{ip_{r_*}^3}{3p_\varphi^2 u^2 (7 - 6p_\varphi^2 u)^2} \left(38072160 - 92454747p_\varphi^2 u + 79749569p_\varphi^4 u^2 - 137703015p_\varphi^6 u^3 \right) \right] \end{aligned}$$

¹⁷ For all the modes with $\ell > 4$, at 2PN accuracy, one has at most just the Newtonian contribution, which means $\hat{h}_{\ell m} = 1$ and no relativistic factors.

¹⁸ These are: $\hat{h}_{30}^{\text{tail-nc}}, \hat{h}_{32}^{\text{tail-nc}}, \hat{h}_{40}^{\text{tail-nc}}, \hat{h}_{41}^{\text{tail-nc}}, \hat{h}_{42}^{\text{tail-nc}}, \hat{h}_{43}^{\text{tail-nc}}, \hat{h}_{44}^{\text{tail-nc}}$.

$$\begin{aligned}
& + 356358768p_\varphi^8 u^4 - 482607515p_\varphi^{10} u^5 + 363100527p_\varphi^{12} u^6 - 161234979p_\varphi^{14} u^7 + 40408200p_\varphi^{16} u^8 \\
& - 4441608p_\varphi^{18} u^9 \Big) - \frac{p_{r_*}^4}{2p_\varphi^3 u^3 (7 - 6p_\varphi^2 u)^3} \Big(304577280 - 928941216p_\varphi^2 u + 1082387695p_\varphi^4 u^2 \\
& - 1365588354p_\varphi^6 u^3 + 3139841017p_\varphi^8 u^4 - 4991336104p_\varphi^{10} u^5 + 4638849326p_\varphi^{12} u^6 - 2632737900p_\varphi^{14} u^7 \\
& + 916090404p_\varphi^{16} u^8 - 181221912p_\varphi^{18} u^9 + 15589584p_\varphi^{20} u^{10} \Big) \Big]. \tag{A3}
\end{aligned}$$

$$\begin{aligned}
\hat{h}_{33}^{\text{tail-nc}} = 1 - \frac{\pi}{3840c^3 p_\varphi^2 (2p_\varphi^2 u + 7)^2} & \Big[ip_{r_*} \Big(47630 + 134366p_\varphi^2 u + 721737p_\varphi^4 u^2 - 429865p_\varphi^6 u^3 + 308120p_\varphi^8 u^4 \\
& - 107220p_\varphi^{10} u^5 + 16769p_\varphi^{12} u^6 - 337p_\varphi^{14} u^7 \Big) + \frac{p_{r_*}^2}{2p_\varphi u (2p_\varphi^2 u + 7)} \Big(381040 + 1407963p_\varphi^2 u \\
& - 2751544p_\varphi^4 u^2 + 8146332p_\varphi^6 u^3 - 5435500p_\varphi^8 u^4 + 3011095p_\varphi^{10} u^5 - 1073428p_\varphi^{12} u^6 + 170074p_\varphi^{14} u^7 + \\
& 14688p_\varphi^{16} u^8 \Big) - \frac{ip_{r_*}^3}{p_\varphi^2 u^2 (2p_\varphi^2 u + 7)^2} \Big(762080 + 3125521p_\varphi^2 u + 5675333p_\varphi^4 u^2 \\
& - 28858731p_\varphi^6 u^3 + 28110216p_\varphi^8 u^4 - 14716055p_\varphi^{10} u^5 + 7128059p_\varphi^{12} u^6 - 2725303p_\varphi^{14} u^7 \\
& + 281976p_\varphi^{16} u^8 + 41864p_\varphi^{18} u^9 \Big) - \frac{p_{r_*}^4}{2p_\varphi^3 u^3 (2p_\varphi^2 u + 7)^3} \Big(6096640 + 27480928p_\varphi^2 u + 92901791p_\varphi^4 u^2 \\
& + 57821954p_\varphi^6 u^3 - 472378615p_\varphi^8 u^4 + 376035640p_\varphi^{10} u^5 - 164962538p_\varphi^{12} u^6 + 71523844p_\varphi^{14} u^7 \\
& - 24385644p_\varphi^{16} u^8 + 1291400p_\varphi^{18} u^9 + 320720p_\varphi^{20} u^{10} \Big) \Big]. \tag{A4}
\end{aligned}$$

b. *Instantaneous noncircular factors*

$$\begin{aligned}
f_{20}^{\text{inst-nc}} = 1 + \frac{1}{c^2} & \left\{ \frac{p_{r_*}^2}{-1 + p_\varphi^2 u} \left[\left(\frac{1}{14} - \frac{31\nu}{14} \right) + p_\varphi^2 u \left(\frac{9}{14} + \frac{15\nu}{14} \right) \right] + \frac{p_{r_*}^4}{u(-1 + p_\varphi^2 u)^2} \left(-\frac{5}{7} + \frac{8\nu}{7} \right) \right\} \\
& + \frac{1}{c^4} \left\{ \frac{p_{r_*}^2}{(-1 + p_\varphi^2 u)^2} \left[u \left(\frac{65}{252} + \frac{211\nu}{126} + \frac{139\nu^2}{63} \right) + p_\varphi^2 u^2 \left(\frac{3683}{3528} - \frac{39371\nu}{1764} - \frac{5099\nu^2}{882} \right) \right] \right. \\
& + p_\varphi^4 u^3 \left(\frac{1825}{1176} + \frac{5239\nu}{294} + \frac{703\nu^2}{147} \right) + p_\varphi^6 u^4 \left(-\frac{209}{294} - \frac{355\nu}{588} - \frac{355\nu^2}{294} \right) \Big] \\
& + \frac{p_{r_*}^4}{(-1 + p_\varphi^2 u)^3} \left[\left(\frac{1613}{504} - \frac{1567\nu}{504} - \frac{71\nu^2}{72} \right) + p_\varphi^2 u \left(-\frac{16819}{1764} + \frac{92131\nu}{3528} + \frac{7421\nu^2}{3528} \right) \right. \\
& \left. + p_\varphi^4 u^2 \left(\frac{323}{147} - \frac{19445\nu}{1176} - \frac{1279\nu^2}{1176} \right) + p_\varphi^6 u^3 \left(-\frac{25}{168} + \frac{65\nu}{168} - \frac{5\nu^2}{168} \right) \right] \Big\}, \tag{A5}
\end{aligned}$$

$$\delta_{20}^{\text{inst-nc}} = 0. \tag{A6}$$

$$f_{21}^{\text{inst-nc}} = 1 + \frac{1}{c^2} p_{r_*}^2 \left(\frac{9}{14} + \frac{5\nu}{7} \right), \tag{A7}$$

$$\delta_{21}^{\text{inst-nc}} = \frac{1}{c^2} p_{r_*} p_\varphi \left(\frac{1}{14} + \frac{6\nu}{7} \right). \tag{A8}$$

$$f_{30}^{\text{inst-nc}} = 1 + \frac{1}{c^2} p_{r_*}^2 \frac{5 - 7\nu - 17\nu^2}{6 - 18\nu}, \quad (\text{A9})$$

$$\delta_{30}^{\text{inst-nc}} = 0. \quad (\text{A10})$$

$$f_{31}^{\text{inst-nc}} = 1 + \frac{1}{c^2} \left\{ \frac{p_{r_*}^2}{p_\varphi^2 u (-7 + 6p_\varphi^2 u)^3} \left[(-1076 + 1168\nu) + p_\varphi^2 u \left(\frac{4783}{2} - 4242\nu \right) + p_\varphi^4 u^2 (-1520 + 4834\nu) \right. \right. \\ \left. \left. + p_\varphi^6 u^3 (6 - 2136\nu) + p_\varphi^8 u^4 (180 + 288\nu) \right] + \frac{p_{r_*}^4}{p_\varphi^4 u^3 (-7 + 6p_\varphi^2 u)^5} \left[(154944 - 168192\nu) \right. \right. \\ \left. \left. + p_\varphi^2 u (-569222 + 740344\nu) + p_\varphi^4 u^2 (840044 - 1241680\nu) + p_\varphi^6 u^3 (-622914 + 1014636\nu) \right. \right. \\ \left. \left. + p_\varphi^8 u^4 (232812 - 408168\nu) + p_\varphi^{10} u^5 (-35208 + 65232\nu) \right] \right\}, \quad (\text{A11})$$

$$\delta_{31}^{\text{inst-nc}} = \frac{1}{c^2} \left\{ \frac{p_{r_*}}{p_\varphi (7 - 6p_\varphi^2 u)^2} \left[\left(\frac{269}{3} - \frac{292\nu}{3} \right) + p_\varphi^2 u (-146 + 222\nu) + p_\varphi^4 u^2 (61 - 110\nu) \right] \right. \\ \left. + \frac{p_{r_*}^3}{p_\varphi^3 u^2 (7 - 6p_\varphi^2 u)^4} \left[(-12912 + 14016\nu) + p_\varphi^2 u (39410 - 52984\nu) + p_\varphi^4 u^2 (-45043 + 69758\nu) \right. \right. \\ \left. \left. + p_\varphi^6 u^3 (22704 - 39288\nu) + p_\varphi^8 u^4 (-4248 + 8064\nu) \right] \right\}. \quad (\text{A12})$$

$$f_{32}^{\text{inst-nc}} = 1 + \frac{1}{c^2} \left\{ \frac{p_{r_*}^2}{p_\varphi^2 u (-1 + 3\nu)} \left[\left(-\frac{187}{2880} + \frac{223\nu}{576} - \frac{265\nu^2}{576} \right) + p_\varphi^2 u \left(-\frac{221}{192} + \frac{547\nu}{192} + \frac{227\nu^2}{192} \right) \right] \right. \\ \left. + \frac{p_{r_*}^4}{p_\varphi^4 u^3 (-1 + 3\nu)} \left[\left(\frac{187}{46080} - \frac{223\nu}{9216} + \frac{265\nu^2}{9216} \right) + p_\varphi^2 u \left(\frac{61}{3072} - \frac{323\nu}{3072} + \frac{317\nu^2}{3072} \right) \right] \right\}, \quad (\text{A13})$$

$$\delta_{32}^{\text{inst-nc}} = \frac{1}{c^2} \left\{ \frac{p_{r_*}}{p_\varphi (-1 + 3\nu)} \left[\left(-\frac{187}{720} + \frac{223\nu}{144} - \frac{265\nu^2}{144} \right) + p_\varphi^2 u \left(-\frac{433}{240} + \frac{355\nu}{48} - \frac{157\nu^2}{48} \right) \right] \right. \\ \left. + \frac{p_{r_*}^3}{p_\varphi^3 u^2 (-1 + 3\nu)} \left[\left(\frac{187}{11520} - \frac{223\nu}{2304} + \frac{265\nu^2}{2304} \right) + p_\varphi^2 u \left(\frac{61}{768} - \frac{323\nu}{768} + \frac{317\nu^2}{768} \right) \right] \right\}. \quad (\text{A14})$$

$$f_{33}^{\text{inst-nc}} = 1 + \frac{1}{c^2} \left\{ \frac{p_{r_*}^2}{p_\varphi^2 u (7 + 2p_\varphi^2 u)^3} \left[\left(\frac{1076}{9} - \frac{1168\nu}{9} \right) + p_\varphi^2 u \left(\frac{9161}{18} + \frac{2626\nu}{9} \right) + p_\varphi^4 u^2 \left(\frac{1292}{3} - \frac{214\nu}{3} \right) \right. \right. \\ \left. \left. + p_\varphi^6 u^3 \left(\frac{1430}{3} - \frac{424\nu}{3} \right) + p_\varphi^8 u^4 \left(\frac{20}{3} + \frac{32\nu}{3} \right) \right] + \frac{p_{r_*}^4}{p_\varphi^4 u^3 (7 + 2p_\varphi^2 u)^5} \left[\left(-\frac{17216}{9} + \frac{18688\nu}{9} \right) \right. \right. \\ \left. \left. + p_\varphi^2 u \left(-\frac{55034}{9} + \frac{52744\nu}{9} \right) + p_\varphi^4 u^2 \left(-\frac{23140}{3} + \frac{23984\nu}{3} \right) + p_\varphi^6 u^3 \left(\frac{11510}{3} - \frac{44260\nu}{3} \right) \right. \right. \\ \left. \left. + p_\varphi^8 u^4 \left(\frac{163540}{9} - \frac{57560\nu}{9} \right) + p_\varphi^{10} u^5 \left(-\frac{11912}{3} + \frac{7888\nu}{3} \right) \right] \right\}, \quad (\text{A15})$$

$$\delta_{33}^{\text{inst-nc}} = \frac{1}{c^2} \left\{ \frac{p_{r_*}}{p_\varphi (7 + 2p_\varphi^2 u)^2} \left[\left(\frac{269}{9} - \frac{292\nu}{9} \right) + p_\varphi^2 u \left(\frac{970}{9} - \frac{1142\nu}{9} \right) + p_\varphi^4 u^2 \left(\frac{313}{3} - \frac{182\nu}{3} \right) \right] \right. \\ \left. + \frac{p_{r_*}^3}{p_\varphi^3 u^2 (7 + 2p_\varphi^2 u)^4} \left[\left(-\frac{4304}{9} + \frac{4672\nu}{9} \right) + p_\varphi^2 u \left(-\frac{12010}{9} + \frac{11288\nu}{9} \right) + p_\varphi^4 u^2 (431 - 1318\nu) \right] \right\}$$

$$+ p_\varphi^6 u^3 \left(\frac{5456}{3} + \frac{968\nu}{3} \right) + p_\varphi^8 u^4 (-1336 + 864\nu) \Big] \Big\}. \quad (\text{A16})$$

$$\begin{aligned} f_{40}^{\text{inst-nc}} = & 1 + \frac{1}{c^2} \left\{ \frac{p_{r_*}^2}{(7 - 6p_\varphi^2 u)^2 (-1 + p_\varphi^2 u) (-1 + 3\nu)} \left[\left(-\frac{785}{11} + \frac{11205\nu}{22} - \frac{17673\nu^2}{22} \right) \right. \right. \\ & + p_\varphi^2 u \left(57 - \frac{1627\nu}{2} + \frac{3479\nu^2}{2} \right) + p_\varphi^4 u^2 (45 + 276\nu - 1092\nu^2) + p_\varphi^6 u^3 \left(-\frac{414}{11} + \frac{486\nu}{11} + \frac{1890\nu^2}{11} \right) \Big] \\ & + \frac{p_{r_*}^4}{u (-7 + 6p_\varphi^2 u)^3 (-1 + p_\varphi^2 u)^2 (-1 + 3\nu)} \left[\left(-\frac{20367}{11} + \frac{94608\nu}{11} - \frac{94608\nu^2}{11} \right) \right. \\ & + p_\varphi^2 u \left(\frac{8133}{2} - 19992\nu + 22128\nu^2 \right) + p_\varphi^4 u^2 \left(-\frac{65727}{22} + \frac{169416\nu}{11} - \frac{201888\nu^2}{11} \right) \\ & \left. \left. + p_\varphi^6 u^3 \left(\frac{8037}{11} - \frac{43056\nu}{11} + \frac{54144\nu^2}{11} \right) \right] \right\}, \quad (\text{A17}) \end{aligned}$$

$$\delta_{40}^{\text{inst-nc}} = 0. \quad (\text{A18})$$

$$f_{41}^{\text{inst-nc}} = 1, \quad (\text{A19})$$

$$\delta_{42}^{\text{inst-nc}} = 0. \quad (\text{A20})$$

$$\begin{aligned} f_{42}^{\text{inst-nc}} = & 1 + \frac{1}{c^2} \left\{ \frac{p_{r_*}^2}{(-7 - 3p_\varphi^2 u + 6p_\varphi^4 u^2)^3 (-1 + 3\nu)} \left[\left(-\frac{5495}{11} + \frac{78435\nu}{22} - \frac{123711\nu^2}{22} \right) \right. \right. \\ & + p_\varphi^2 u \left(\frac{22794}{55} - \frac{95055\nu}{22} + \frac{237351\nu^2}{22} \right) + p_\varphi^4 u^2 \left(\frac{2308683}{220} - \frac{778917\nu}{22} + \frac{83871\nu^2}{22} \right) \\ & + p_\varphi^6 u^3 \left(-\frac{4346379}{220} + \frac{1713879\nu}{22} - \frac{991377\nu^2}{22} \right) + p_\varphi^8 u^4 \left(\frac{692577}{55} - \frac{603477\nu}{11} + \frac{491211\nu^2}{11} \right) \\ & + p_\varphi^{10} u^5 \left(-\frac{127386}{55} + \frac{136890\nu}{11} - \frac{160650\nu^2}{11} \right) + p_\varphi^{12} u^6 \left(-\frac{2484}{11} + \frac{2916\nu}{11} + \frac{11340\nu^2}{11} \right) \Big] \\ & + \frac{p_{r_*}^4}{u (-7 - 3p_\varphi^2 u + 6p_\varphi^4 u^2)^5 (-1 + 3\nu)} \left[\left(-\frac{997983}{11} + \frac{4635792\nu}{11} - \frac{4635792\nu^2}{11} \right) \right. \\ & + p_\varphi^2 u \left(\frac{43866123}{55} - \frac{47651520\nu}{11} + \frac{63443142\nu^2}{11} \right) + p_\varphi^4 u^2 \left(\frac{35844849}{22} - \frac{16122492\nu}{11} - \frac{135164952\nu^2}{11} \right) \\ & + p_\varphi^6 u^3 \left(-\frac{525077109}{44} + \frac{441545616\nu}{11} - \frac{53867457\nu^2}{11} \right) + p_\varphi^8 u^4 \left(\frac{4684992993}{220} - \frac{914171508\nu}{11} + \frac{489089961\nu^2}{11} \right) \\ & + p_\varphi^{10} u^5 \left(-\frac{2041998687}{110} + \frac{865358424\nu}{11} - \frac{634963050\nu^2}{11} \right) + p_\varphi^{12} u^6 \left(\frac{96254487}{11} - \frac{433938060\nu}{11} + \frac{377733780\nu^2}{11} \right) \\ & + p_\varphi^{14} u^7 \left(-\frac{23603562}{11} + \frac{112003560\nu}{11} - \frac{109437480\nu^2}{11} \right) \\ & \left. \left. + p_\varphi^{16} u^8 \left(\frac{1077948}{5} - 1069200\nu + 1139184\nu^2 \right) \right] \right\}, \quad (\text{A21}) \end{aligned}$$

$$\begin{aligned}
\delta_{42}^{\text{inst-nc}} = & \frac{1}{c^2} \left\{ \frac{p_{r_*} p_\varphi u}{(7 + 3p_\varphi^2 u - 6p_\varphi^4 u^2)^2 (-1 + 3\nu)} \left[\left(-\frac{5513}{55} + \frac{5854\nu}{11} - \frac{7548\nu^2}{11} \right) \right. \right. \\
& + p_\varphi^2 u \left(-\frac{86061}{220} + \frac{13686\nu}{11} + \frac{273\nu^2}{11} \right) + p_\varphi^4 u^2 \left(\frac{139401}{220} - \frac{29826\nu}{11} + \frac{22599\nu^2}{11} \right) \\
& + p_\varphi^6 u^3 \left(-\frac{2556}{11} + \frac{12186\nu}{11} - \frac{11988\nu^2}{11} \right) \left. \right] \\
& + \frac{p_{r_*}^3 p_\varphi}{(7 + 3p_\varphi^2 u - 6p_\varphi^4 u^2)^4 (-1 + 3\nu)} \left[\left(-\frac{3434319}{110} + \frac{1677774\nu}{11} - \frac{1868580\nu^2}{11} \right) \right. \\
& + p_\varphi^2 u \left(-\frac{1623252}{55} - \frac{321240\nu}{11} + \frac{4439970\nu^2}{11} \right) + p_\varphi^4 u^2 \left(\frac{80592003}{220} - \frac{13474980\nu}{11} + \frac{1467963\nu^2}{11} \right) \\
& + p_\varphi^6 u^3 \left(-\frac{138830193}{220} + \frac{27487404\nu}{11} - \frac{15732441\nu^2}{11} \right) + p_\varphi^8 u^4 \left(\frac{26404461}{55} - \frac{22944114\nu}{11} + \frac{18134496\nu^2}{11} \right) \\
& + p_\varphi^{10} u^5 \left(-\frac{9559404}{55} + \frac{8902440\nu}{11} - \frac{8355960\nu^2}{11} \right) + p_\varphi^{12} u^6 \left(\frac{1342332}{55} - \frac{1324512\nu}{11} + \frac{1395792\nu^2}{11} \right) \left. \right] \left. \right\}. \quad (\text{A22})
\end{aligned}$$

$$f_{43}^{\text{inst-nc}} = 1, \quad (\text{A23})$$

$$\delta_{43}^{\text{inst-nc}} = 0. \quad (\text{A24})$$

$$\begin{aligned}
f_{44}^{\text{inst-nc}} = & 1 + \frac{1}{c^2} \left\{ \frac{p_{r_*}^2}{(7 + 51p_\varphi^2 u + 6p_\varphi^4 u^2)^3 (-1 + 3\nu)} \left[\left(\frac{5495}{11} - \frac{78435\nu}{22} + \frac{123711\nu^2}{22} \right) \right. \right. \\
& + p_\varphi^2 u \left(\frac{210159}{55} - \frac{667917\nu}{22} + \frac{914625\nu^2}{22} \right) + p_\varphi^4 u^2 \left(-\frac{9429801}{55} + \frac{12229341\nu}{22} - \frac{2912121\nu^2}{22} \right) \\
& + p_\varphi^6 u^3 \left(-\frac{19606626}{55} + \frac{22336029\nu}{22} + \frac{2602071\nu^2}{22} \right) + p_\varphi^8 u^4 \left(-\frac{7261839}{55} + \frac{4772385\nu}{11} - \frac{1459053\nu^2}{11} \right) \\
& + p_\varphi^{10} u^5 \left(-\frac{564948}{11} + \frac{1931958\nu}{11} - \frac{475470\nu^2}{11} \right) + p_\varphi^{12} u^6 \left(-\frac{2484}{11} + \frac{2916\nu}{11} + \frac{11340\nu^2}{11} \right) \left. \right] \\
& + \frac{p_{r_*}^4}{u (7 + 51p_\varphi^2 u + 6p_\varphi^4 u^2)^5 (-1 + 3\nu)} \left[\left(\frac{997983}{11} - \frac{4635792\nu}{11} + \frac{4635792\nu^2}{11} \right) \right. \\
& + p_\varphi^2 u \left(-\frac{144030369}{110} + \frac{92715672\nu}{11} - \frac{152428248\nu^2}{11} \right) + p_\varphi^4 u^2 \left(-\frac{737730837}{11} + \frac{3011803560\nu}{11} - \frac{2051555040\nu^2}{11} \right) \\
& + p_\varphi^6 u^3 \left(-\frac{2431571553}{55} + \frac{1633697784\nu}{11} - \frac{187083648\nu^2}{11} \right) + p_\varphi^8 u^4 \left(\frac{486563193}{5} - 405446040\nu + 297670464\nu^2 \right) \\
& + p_\varphi^{10} u^5 \left(\frac{3125458143}{110} - \frac{956714976\nu}{11} - \frac{188690472\nu^2}{11} \right) \\
& + p_\varphi^{12} u^6 \left(-\frac{3895064577}{55} + \frac{3530464704\nu}{11} - \frac{3326475600\nu^2}{11} \right) \\
& + p_\varphi^{14} u^7 \left(-\frac{673781166}{11} + \frac{2335443840\nu}{11} - \frac{497702880\nu^2}{11} \right) \left. \right\}
\end{aligned}$$

$$+ p_\varphi^{16} u^8 \left(\frac{305560836}{55} - \frac{229080960\nu}{11} + \frac{102316608\nu^2}{11} \right) \Big] \Big\}, \quad (\text{A25})$$

$$\begin{aligned} \delta_{44}^{\text{inst-nc}} = & -\frac{1}{c^2} \left\{ \frac{p_{r_*} p_\varphi u}{\left(7 + 51p_\varphi^2 u + 6p_\varphi^4 u^2\right)^2 (-1 + 3\nu)} \left[\left(\frac{11026}{55} - \frac{11708\nu}{11} + \frac{15096\nu^2}{11} \right) \right. \right. \\ & + p_\varphi^2 u \left(\frac{555681}{110} - \frac{233274\nu}{11} + \frac{175788\nu^2}{11} \right) + p_\varphi^4 u^2 \left(\frac{939051}{110} - \frac{377406\nu}{11} + \frac{241380\nu^2}{11} \right) \\ & \left. + p_\varphi^6 u^3 \left(\frac{172872}{55} - \frac{126540\nu}{11} + \frac{47736\nu^2}{11} \right) \right] \\ & + \frac{p_{r_*}^3 p_\varphi}{\left(7 + 51p_\varphi^2 u + 6p_\varphi^4 u^2\right)^4 (-1 + 3\nu)} \left[\left(\frac{3434319}{55} - \frac{3355548\nu}{11} + \frac{3737160\nu^2}{11} \right) \right. \\ & + p_\varphi^2 u \left(\frac{68284914}{55} - \frac{53840352\nu}{11} + \frac{31634784\nu^2}{11} \right) + p_\varphi^4 u^2 \left(-\frac{69674769}{55} + \frac{66841884\nu}{11} - \frac{71727336\nu^2}{11} \right) \\ & + p_\varphi^6 u^3 \left(-\frac{221951034}{55} + \frac{179751888\nu}{11} - \frac{118566720\nu^2}{11} \right) + p_\varphi^8 u^4 \left(\frac{64377018}{55} - \frac{49429008\nu}{11} + \frac{25417152\nu^2}{11} \right) \\ & + p_\varphi^{10} u^5 \left(\frac{74535768}{55} - \frac{42300576\nu}{11} - \frac{20036160\nu^2}{11} \right) \\ & \left. \left. + p_\varphi^{12} u^6 \left(-\frac{29497608}{55} + \frac{22006080\nu}{11} - \frac{9517824\nu^2}{11} \right) \right] \right\}. \quad (\text{A26}) \end{aligned}$$

Appendix B: Independent derivation of the angular radiation reaction force of Ref. [40]

In Ref. [40] Bini and Damour recomputed in the EOB formalism the instantaneous part of the radiation reaction force $\hat{\mathcal{F}}$ valid for general orbits, which had been originally obtained in harmonic coordinates by Iyer, Will and collaborators (see for instance Ref. [65]). In order to provide a meaningful check for the canonical transformations (5)-(8) we performed an alternative computation of the angular component $\hat{\mathcal{F}}_\varphi$ by exploiting directly our results for the instantaneous 2PN spherical modes $h_{\ell m}^{\text{inst}}$ discussed in Sec. II A 1.

The radiation-reaction force components $\hat{\mathcal{F}}_{r,\varphi}$ that drive the non conservative part of the EOB dynamics can be related via the equations of motion to the system loss of energy and angular momentum, which in turn are connected to the energy and angular momentum fluxes at infinity \dot{E} and \dot{J} by the balance equations. Overall we can write [40]

$$\dot{r}\hat{\mathcal{F}}_r + \Omega\hat{\mathcal{F}}_\varphi + \dot{E}_{\text{Schott}} + \dot{E} = 0, \quad (\text{B1})$$

$$\hat{\mathcal{F}}_\varphi + \dot{J} = 0, \quad (\text{B2})$$

where E_{Schott} is the Schott contribution to the energy of the system, due to its interaction with the local field. In general Eq. (B2) contains an additional Schott contribution \dot{J}_{Schott} but in Sec. II of [40] it has been shown that

such term can be always gauged away. Therefore thanks to this equation and the expression of the flux \dot{J} in terms of the multipolar waveform we can determine the angular component of the radiation-reaction force simply as

$$\hat{\mathcal{F}}_\varphi = -\dot{J} = \frac{1}{16\pi} \sum_{\ell=2}^{\ell_{\text{max}}} \sum_{m=-\ell}^{\ell} m \Im \left[\dot{h}_{\ell m} h_{\ell m}^* \right]. \quad (\text{B3})$$

This paves the way to recompute independently the 2PN instantaneous result for \mathcal{F}_φ given in Eq. (3.70) of Ref. [40], as mentioned above. The instantaneous modes that bring a non-zero contribution to $\hat{\mathcal{F}}_\varphi$ at 2PN are h_{21}^{inst} , h_{22}^{inst} , h_{31}^{inst} , h_{32}^{inst} , h_{33}^{inst} , h_{42}^{inst} and h_{44}^{inst} . The angular radiation reaction force coming from Eq. (B3) has proved to be consistent with the result of Ref. [40].

Appendix C: Alternative corrections using \dot{p}_{r_*}

As briefly discussed at the end of Sec. II C in this appendix we assay an alternative writing for the noncircular 2PN corrections for the modes with $m \neq 0$. Starting from the results in terms of u , p_{r_*} and p_φ we discussed in Sec. II B, we exploit the 2PN equation of motion for \dot{p}_{r_*} , invert it with respect to p_φ and use the resulting relation to recast everything in terms of u , p_{r_*} and \dot{p}_{r_*} . For the (2,2) mode, again the primary target of our focus, we find

$$\begin{aligned}
\left[\hat{h}_{22}^{\text{nc tail}}\right]_{\dot{p}_{r_*}} &= 1 - \frac{\pi}{c^3} \left(\frac{3}{2} i p_{r_*} u + \frac{i p_{r_*} \dot{p}_{r_*}}{4u} + \frac{p_{r_*}^2 \sqrt{u}}{2} - \frac{3i p_{r_*} \dot{p}_{r_*}^2}{16u^3} + \frac{5p_{r_*}^2 \dot{p}_{r_*}}{16u^{3/2}} + \frac{5i p_{r_*}^3}{48} + \frac{i p_{r_*} \dot{p}_{r_*}^3}{32u^5} \right. \\
&\quad - \frac{p_{r_*}^2 \dot{p}_{r_*}^2}{4u^{7/2}} - \frac{15i p_{r_*}^3 \dot{p}_{r_*}}{32u^2} + \frac{5p_{r_*}^4}{16\sqrt{u}} - \frac{11i p_{r_*} \dot{p}_{r_*}^4}{384u^7} + \frac{101p_{r_*}^2 \dot{p}_{r_*}^3}{384u^{11/2}} + \frac{53i p_{r_*}^3 \dot{p}_{r_*}^2}{96u^4} \\
&\quad - \frac{115p_{r_*}^4 \dot{p}_{r_*}}{192u^{5/2}} - \frac{589i p_{r_*}^5}{1920u} - \frac{223i p_{r_*} \dot{p}_{r_*}^5}{3840u^9} + \frac{257p_{r_*}^2 \dot{p}_{r_*}^4}{768u^{15/2}} + \frac{181i p_{r_*}^3 \dot{p}_{r_*}^3}{288u^6} - \frac{83p_{r_*}^4 \dot{p}_{r_*}^2}{128u^{9/2}} \\
&\quad \left. - \frac{111i p_{r_*}^5 \dot{p}_{r_*}}{256u^3} + \frac{329p_{r_*}^6}{1920u^{3/2}} \right), \tag{C1}
\end{aligned}$$

$$\begin{aligned}
\left[f_{22}^{\text{nc inst}}\right]_{\dot{p}_{r_*}} &= 1 + \frac{1}{c^2} \left[\frac{(3\nu + 62)p_{r_*}^2}{42} + \frac{(65 - 48\nu)p_{r_*}^2 \dot{p}_{r_*}}{84u^2} + \frac{(114\nu - 115)p_{r_*}^2 \dot{p}_{r_*}^2}{168u^4} + \frac{(10 - 9\nu)p_{r_*}^4}{21u} \right. \\
&\quad + \frac{(115 - 156\nu)p_{r_*}^2 \dot{p}_{r_*}^3}{336u^6} + \frac{(144\nu - 125)p_{r_*}^4 \dot{p}_{r_*}}{168u^3} + \frac{(174\nu - 65)p_{r_*}^2 \dot{p}_{r_*}^4}{672u^8} + \frac{(55 - 144\nu)p_{r_*}^4 \dot{p}_{r_*}^2}{336u^5} + \frac{(6\nu - 5)p_{r_*}^6}{24u^2} \left. \right] \\
&\quad + \frac{1}{c^4} \left[\frac{(1685 - 1506\nu - 336\nu^2)p_{r_*}^2 u}{504} - \frac{(76039 - 79256\nu + 29480\nu^2)p_{r_*}^2 \dot{p}_{r_*}}{42336u} \right. \\
&\quad - \frac{(40120 - 41507\nu + 6257\nu^2)p_{r_*}^2 \dot{p}_{r_*}^2}{10584u^3} + \frac{(2609 + 4538\nu + 382\nu^2)p_{r_*}^4}{3024} \\
&\quad + \frac{(227327 - 281328\nu + 48696\nu^2)p_{r_*}^2 \dot{p}_{r_*}^3}{56448u^5} - \frac{(198001 - 378512\nu + 96248\nu^2)p_{r_*}^4 \dot{p}_{r_*}}{84672u^2} \\
&\quad - \frac{11(9290 - 14020\nu + 3019\nu^2)p_{r_*}^2 \dot{p}_{r_*}^4}{42336u^7} + \frac{(749981 - 1363564\nu + 247480\nu^2)p_{r_*}^4 \dot{p}_{r_*}^2}{169344u^4} \\
&\quad \left. - \frac{(4687 - 20688\nu + 5916\nu^2)p_{r_*}^6}{14112u} \right], \tag{C2}
\end{aligned}$$

$$\begin{aligned}
\left[\delta_{22}^{\text{nc inst}}\right]_{\dot{p}_{r_*}} &= \frac{1}{c^2} \left[\frac{(25 - 26\nu)p_{r_*} \sqrt{u}}{14} + \frac{(25 - 12\nu)p_{r_*} \dot{p}_{r_*}}{42u^{3/2}} - \frac{(25 - 18\nu)p_{r_*} \dot{p}_{r_*}^2}{48u^{7/2}} + \frac{(6\nu + 5)p_{r_*}^3}{84\sqrt{u}} \right. \\
&\quad + \frac{5(10 - 9\nu)p_{r_*} \dot{p}_{r_*}^3}{168u^{11/2}} - \frac{5(31 - 30\nu)p_{r_*}^3 \dot{p}_{r_*}}{168u^{5/2}} - \frac{(775 - 918\nu)p_{r_*} \dot{p}_{r_*}^4}{5376u^{15/2}} + \frac{3(45 - 58\nu)p_{r_*}^3 \dot{p}_{r_*}^2}{224u^{9/2}} \\
&\quad \left. - \frac{(25 - 26\nu)p_{r_*}^5}{56u^{3/2}} + \frac{(325 - 576\nu)p_{r_*} \dot{p}_{r_*}^5}{5376u^{19/2}} - \frac{(145 - 498\nu)p_{r_*}^3 \dot{p}_{r_*}^3}{1344u^{13/2}} + \frac{3(5 - 8\nu)p_{r_*}^5 \dot{p}_{r_*}}{56u^{7/2}} \right] \\
&\quad + \frac{1}{c^4} \left[\frac{(31259 - 10972\nu - 11360\nu^2)p_{r_*} u^{3/2}}{10584} - \frac{(30467 - 58216\nu - 26216\nu^2)p_{r_*} \dot{p}_{r_*}}{21168\sqrt{u}} \right. \\
&\quad - \frac{(197641 - 182480\nu + 20600\nu^2)p_{r_*} \dot{p}_{r_*}^2}{84672u^{5/2}} - \frac{(25213 - 81572\nu - 27568\nu^2)p_{r_*}^3 \sqrt{u}}{21168} \\
&\quad + \frac{(430967 - 462772\nu + 66832\nu^2)p_{r_*} \dot{p}_{r_*}^3}{169344u^{9/2}} - \frac{(15711 - 16846\nu + 11500\nu^2)p_{r_*}^3 \dot{p}_{r_*}}{14112u^{3/2}} \\
&\quad - \frac{(2456467 - 2958740\nu + 594704\nu^2)p_{r_*} \dot{p}_{r_*}^4}{1354752u^{13/2}} + \frac{(866783 - 1234624\nu + 221608\nu^2)p_{r_*}^3 \dot{p}_{r_*}^2}{169344u^{7/2}} \\
&\quad - \frac{(38639 - 34420\nu + 21376\nu^2)p_{r_*}^5}{42336\sqrt{u}} + \frac{(2807687 - 4018384\nu + 1077064\nu^2)p_{r_*} \dot{p}_{r_*}^5}{2709504u^{17/2}} \\
&\quad \left. - \frac{(149307 - 248258\nu + 44612\nu^2)p_{r_*}^3 \dot{p}_{r_*}^3}{37632u^{11/2}} + \frac{(324131 - 573220\nu + 81808\nu^2)p_{r_*}^5 \dot{p}_{r_*}}{84672u^{5/2}} \right]. \tag{C3}
\end{aligned}$$

In Fig. 19 we look at the test-particle case and compare the above corrections with those of Sec. II B, specifically those with all the resummations. Without the need of a resummation scheme, the accuracy of the former turns out to be practically equivalent to the one of the latter,

especially for low or moderate eccentricity. Nevertheless, the evaluation of \dot{p}_{r_*} through the Hamilton's equation in the comparable mass case is less efficient than using directly p_φ and for this reason we deem preferable the resummed corrections containing p_φ presented in Sec. II B.

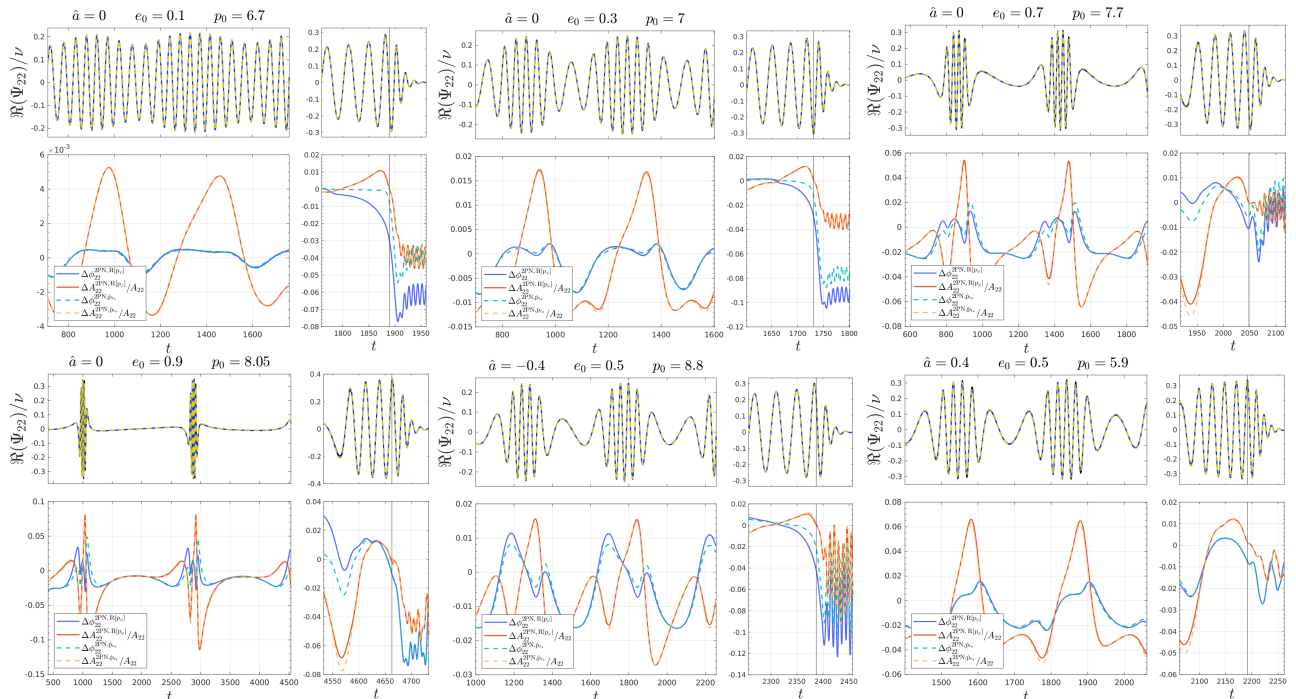


FIG. 19. Analytical/numerical comparisons of the $\ell = m = 2$ mode for different values of initial eccentricity and Kerr spin-parameter. In the top panels we show the real part of the numerical waveform (black, almost indistinguishable), the analytical waveform with resummed 2PN noncircular corrections written in terms of (p_{r_*}, p_φ) (solid blue) and the analytical one with corrections written in terms of (p_{r_*}, \dot{p}_{r_*}) (dashed yellow). The corresponding analytical/numerical phase differences and amplitude relative differences are shown in the bottom panels (solid lines for resummed corrections with p_φ , dashed lines for the corrections with \dot{p}_{r_*}).

- [1] R. Abbott *et al.* (LIGO Scientific, VIRGO, KAGRA), (2021), arXiv:2111.03606 [gr-qc].
- [2] D. Reitze *et al.*, (2021), arXiv:2111.06986 [gr-qc].
- [3] P. Couvares *et al.*, (2021), arXiv:2111.06987 [gr-qc].
- [4] M. Punturo *et al.*, (2021), arXiv:2111.06988 [gr-qc].
- [5] S. Katsanevas *et al.*, (2021), arXiv:2111.06989 [gr-qc].
- [6] V. Kalogera *et al.*, (2021), arXiv:2111.06990 [gr-qc].
- [7] D. McClelland *et al.*, (2021), arXiv:2111.06991 [gr-qc].
- [8] M. Maggiore *et al.*, JCAP **03**, 050 (2020), arXiv:1912.02622 [astro-ph.CO].
- [9] M. Evans *et al.*, (2021), arXiv:2109.09882 [astro-ph.IM].
- [10] P. Amaro-Seoane *et al.* (LISA), (2017), arXiv:1702.00786 [astro-ph.IM].
- [11] P. Amaro-Seoane, J. R. Gair, M. Freitag, M. Coleman Miller, I. Mandel, C. J. Cutler, and S. Babak, Class. Quant. Grav. **24**, R113 (2007), arXiv:astro-ph/0703495.
- [12] P. Amaro-Seoane, Phys. Rev. D **98**, 063018 (2018), arXiv:1807.03824 [astro-ph.HE].
- [13] S. Babak, J. Gair, A. Sesana, E. Barausse, C. F. Sopuerta, C. P. L. Berry, E. Berti, P. Amaro-Seoane, A. Petiteau, and A. Klein, Phys. Rev. D **95**, 103012 (2017), arXiv:1703.09722 [gr-qc].
- [14] M. Pirrer and C.-J. Haster, Phys. Rev. Res. **2**, 023151 (2020), arXiv:1912.10055 [gr-qc].
- [15] I. Hinder, L. E. Kidder, and H. P. Pfeiffer, (2017), arXiv:1709.02007 [gr-qc].
- [16] T. Hinderer and S. Babak, Phys. Rev. **D96**, 104048 (2017), arXiv:1707.08426 [gr-qc].
- [17] D. Chiamarello and A. Nagar, Phys. Rev. D **101**, 101501 (2020), arXiv:2001.11736 [gr-qc].
- [18] T. Islam, V. Varma, J. Lodman, S. E. Field, G. Khanna, M. A. Scheel, H. P. Pfeiffer, D. Gerosa, and L. E. Kidder, (2021), arXiv:2101.11798 [gr-qc].
- [19] S. Albanesi, A. Nagar, and S. Bernuzzi, Phys. Rev. D **104**, 024067 (2021), arXiv:2104.10559 [gr-qc].
- [20] X. Liu, Z. Cao, and Z.-H. Zhu, (2021), arXiv:2102.08614 [gr-qc].
- [21] Q. Yun, W.-B. Han, X. Zhong, and C. A. Benavides-Gallego, Phys. Rev. D **103**, 124053 (2021), arXiv:2104.03789 [gr-qc].
- [22] A. Tucker and C. M. Will, Phys. Rev. D **104**, 104023 (2021), arXiv:2108.12210 [gr-qc].
- [23] Y. Setyawati and F. Ohme, Phys. Rev. D **103**, 124011 (2021), arXiv:2101.11033 [gr-qc].
- [24] A. Nagar, A. Bonino, and P. Retegno, Phys. Rev. D **103**, 104021 (2021), arXiv:2101.08624 [gr-qc].
- [25] A. Nagar and P. Retegno, (2021), arXiv:2108.02043 [gr-qc].
- [26] G. Cho, S. Tanay, A. Gopakumar, and H. M. Lee, (2021), arXiv:2110.09608 [gr-qc].
- [27] M. Khalil, A. Buonanno, J. Steinhoff, and J. Vines, Phys. Rev. D **104**, 024046 (2021), arXiv:2104.11705 [gr-qc].
- [28] A. Nagar, P. Retegno, R. Gamba, and S. Bernuzzi, Phys. Rev. D **103**, 064013 (2021), arXiv:2009.12857 [gr-qc].

- qc].
- [29] R. Gamba, M. Breschi, G. Carullo, P. Rettegno, S. Albanesi, S. Bernuzzi, and A. Nagar, Submitted to Nature Astronomy (2021), arXiv:2106.05575 [gr-qc].
- [30] R. Abbott *et al.* (LIGO Scientific, Virgo), Phys. Rev. Lett. **125**, 101102 (2020), arXiv:2009.01075 [gr-qc].
- [31] C. K. Mishra, K. G. Arun, and B. R. Iyer, Phys. Rev. **D91**, 084040 (2015), arXiv:1501.07096 [gr-qc].
- [32] A. Ramos-Buades, A. Buonanno, M. Khalil, and S. Ossokine, (2021), arXiv:2112.06952 [gr-qc].
- [33] A. Bohé *et al.*, Phys. Rev. **D95**, 044028 (2017), arXiv:1611.03703 [gr-qc].
- [34] R. Cotesta, A. Buonanno, A. Bohé, A. Taracchini, I. Hinder, and S. Ossokine, Phys. Rev. **D98**, 084028 (2018), arXiv:1803.10701 [gr-qc].
- [35] P. Rettegno, F. Martinetti, A. Nagar, D. Bini, G. Riemenschneider, and T. Damour, (2019), arXiv:1911.10818 [gr-qc].
- [36] A. Albertini, A. Nagar, P. Rettegno, S. Albanesi, and R. Gamba, (2021), arXiv:2111.14149 [gr-qc].
- [37] Y. Boetzel, C. K. Mishra, G. Faye, A. Gopakumar, and B. R. Iyer, Phys. Rev. D **100**, 044018 (2019), arXiv:1904.11814 [gr-qc].
- [38] C. M. Will and A. G. Wiseman, Phys. Rev. D **54**, 4813 (1996), arXiv:gr-qc/9608012.
- [39] A. Gopakumar and B. R. Iyer, Phys. Rev. D **65**, 084011 (2002), arXiv:gr-qc/0110100.
- [40] D. Bini and T. Damour, Phys. Rev. **D86**, 124012 (2012), arXiv:1210.2834 [gr-qc].
- [41] T. Damour and A. Nagar, Phys. Rev. **D76**, 064028 (2007), arXiv:0705.2519 [gr-qc].
- [42] T. Damour, B. R. Iyer, and A. Nagar, Phys. Rev. **D79**, 064004 (2009), arXiv:0811.2069 [gr-qc].
- [43] A. Nagar and A. Shah, Phys. Rev. **D94**, 104017 (2016), arXiv:1606.00207 [gr-qc].
- [44] F. Messina, A. Maldarella, and A. Nagar, Phys. Rev. **D97**, 084016 (2018), arXiv:1801.02366 [gr-qc].
- [45] A. Nagar, F. Messina, C. Kavanagh, G. Lukes-Gerakopoulos, N. Warburton, S. Bernuzzi, and E. Harms, Phys. Rev. **D100**, 104056 (2019), arXiv:1907.12233 [gr-qc].
- [46] A. Nagar, G. Riemenschneider, G. Pratten, P. Rettegno, and F. Messina, Phys. Rev. D **102**, 024077 (2020), arXiv:2001.09082 [gr-qc].
- [47] K. S. Thorne, Rev. Mod. Phys. **52**, 299 (1980).
- [48] G. Riemenschneider, P. Rettegno, M. Breschi, A. Albertini, R. Gamba, S. Bernuzzi, and A. Nagar, Phys. Rev. D **104**, 104045 (2021), arXiv:2104.07533 [gr-qc].
- [49] E. Harms, S. Bernuzzi, A. Nagar, and A. Zenginoglu, Class.Quant.Grav. **31**, 245004 (2014), arXiv:1406.5983 [gr-qc].
- [50] T. Damour, B. R. Iyer, and B. S. Sathyaprakash, Phys. Rev. **D57**, 885 (1998), arXiv:gr-qc/9708034 [gr-qc].
- [51] A. Placidi, M. Orselli, and A. Nagar, (2021), arXiv:In preparation [gr-qc].
- [52] T. Damour, A. Nagar, and S. Bernuzzi, Phys.Rev. **D87**, 084035 (2013), arXiv:1212.4357 [gr-qc].
- [53] A. Nagar and P. Rettegno, Phys. Rev. **D99**, 021501 (2019), arXiv:1805.03891 [gr-qc].
- [54] “Updated Advanced LIGO sensitivity design curve,” <https://dcc.ligo.org/LIGO-T1800044/public>.
- [55] A. Nagar, T. Damour, and A. Tartaglia, Class. Quant. Grav. **24**, S109 (2007), arXiv:gr-qc/0612096.
- [56] T. Regge and J. A. Wheeler, Phys. Rev. **108**, 1063 (1957).
- [57] T. Damour and A. Nagar, Phys.Rev. **D90**, 044018 (2014), arXiv:1406.6913 [gr-qc].
- [58] D. Chiaramello, Laurea Thesis, University of Torino, unpublished.
- [59] C. Munna and C. R. Evans, Phys. Rev. D **100**, 104060 (2019), arXiv:1909.05877 [gr-qc].
- [60] C. Munna, Phys. Rev. D **102**, 124001 (2020), arXiv:2008.10622 [gr-qc].
- [61] C. Munna and C. R. Evans, Phys. Rev. D **102**, 104006 (2020), arXiv:2009.01254 [gr-qc].
- [62] M. L. Katz, A. J. K. Chua, L. Speri, N. Warburton, and S. A. Hughes, (2021), arXiv:2104.04582 [gr-qc].
- [63] S. A. Hughes, N. Warburton, G. Khanna, A. J. K. Chua, and M. L. Katz, (2021), arXiv:2102.02713 [gr-qc].
- [64] E. Harms, S. Bernuzzi, and B. Brüggmann, Class.Quant.Grav. **30**, 115013 (2013), arXiv:1301.1591 [gr-qc].
- [65] A. Gopakumar, B. R. Iyer, and S. Iyer, Phys. Rev. **D55**, 6030 (1997), [Erratum: Phys. Rev.D57,6562(1998)], arXiv:gr-qc/9703075 [gr-qc].